Investigations of Morphologies and Emplacement Mechanisms of Volcanically-Derived Landforms on the Moon and Mars

by

Amber Keske

A Dissertation Presented in Partial Fulfillment
of the Requirements for the Degree
Doctor of Philosophy

Approved August 2018 by the
Graduate Supervisory Committee:

Philip R. Christensen, Chair
Mark S. Robinson
Amanda B. Clarke
Kelin X. Whipple
James F. Bell III

ARIZONA STATE UNIVERSITY

December 2018

ABSTRACT

Previous workers hypothesized that lunar Localized Pyroclastic Deposits (LPDs) represent products of vulcanian-style eruptions, since some have low proportions of juvenile material. The objective of the first study is to determine how juvenile composition, calculated using deposit and vent volumes, varies among LPDs. I used Lunar Reconnaissance Orbiter Camera Narrow Angle Camera (LROC NAC) digital terrain models (DTMs) to generate models of pre-eruption surfaces for 23 LPDs and subtracted them from the NAC DTMs to calculate deposit and vent volumes. Results show that LPDs have a wide range of juvenile compositions and thinning profiles, and that there is a positive relationship between juvenile material proportion and deposit size. These findings indicate there is greater diversity among LPDs than previously understood, and that a simple vulcanian eruption model may only apply to the smallest deposits.

There is consensus that martian outflow channels were formed by catastrophic flooding events, yet many of these channels exhibit lava flow features issuing from the same source as the eroded channels, leading some authors to suggest that lava may have served as their sole agent of erosion. This debate is addressed in two studies that use Context Camera images for photogeologic analysis, geomorphic mapping, and cratering statistics: (1) A study of Mangala Valles showing that it underwent at least two episodes of fluvial activity and at least three episodes of volcanic activity during the Late Amazonian, consistent with alternating episodes of flooding and volcanism. (2) A study of Maja Valles finds that it is thinly draped in lava flows sourced from Lunae Planum to the west, rendering it analogous to the lava-coated Elysium outflow systems. However, the source of eroded channels in Maja Valles is not the source of the its lava flows, which

instead issue from south Lunae Planum. The failure of these lava flows to generate any major channels along their path suggests that the channels of Maja Valles are not lava-eroded.

Finally, I describe a method of locating sharp edges in out-of-focus images for application to automated trajectory control systems that use images from fixed-focus cameras to determine proximity to a target.

ACKNOWLEDGMENTS

This work would not have been possible without the dedicated friends, family, and colleagues who provided scientific and moral support during highs and lows. First, I would like to express my deepest thanks to Chis Hansen for encouraging me during times of existential crisis and for helping me maintain a positive outlook as I neared the end of my studies. Similarly, I would not have been who I am today without the friendships of Steven Glaser, Ly Hoang, Kristi Bradford, and Hayley Williamson, nor without the unwavering support from my Mom, Dad, sister Christa Jones, and brother-in-law Rusty Jones.

I would also like to thank my good friends, colleagues, and mentors at the Mars Space Flight Facility including: Dr. Phil Christensen (primary graduate advisor), graduate students of past and present (Mike Veto, Sean Peters, Jon Hill, Chris Haberle, Chris Mount, Julie Mitchell, Becky Smith, Andy Ryan, Allie Rutledge, Emily Garhart, and Jayath Serla), postdocs, and staff (Ashley Toland, Mark Salvatore, Tara Fisher, and the JMARS developers). I have also been most fortunate for the friendships and professional relationships I have in the LROC team, especially with Dr. Mark Robinson and the DTM group (Megan Henriksen, Madeleine Manheim, Bradley Karas, and Corrine Rojas). Also paramount to my success were the other members my dissertation committee: Drs. Amanda Clarke, Jim Bell, and Kelin Whipple. Additionally, much of my success is owed to my mentors from the U of A, including Drs. Alfred McEwen, Peter Smith, Christopher Hamilton, and Ingrid Daubar. Thanks also to my piano teacher Tim Rovnak, who helped me keep the soul in the music that keeps me grounded.

Support for my graduate work was most graciously provided by the National Science Foundation Graduate Research Fellowship Program and the THEMIS mission.

TABLE OF CONTENTS

Page

CHAPTER Page

LIST OF TABLES

LIST OF FIGURES

Figure Page

CHAPTER 1

INTRODUCTION

Since the dawn of humanity, fascination with the awe-inspiring yet destructive power of volcanoes has inspired art, myth, and scientific endeavors. The advent of the Space Age has since broadened our understanding of the true importance of volcanism as a fundamental process in planetary development both as an interior process and as a resurfacing agent. The diversity of volcanic landforms discovered in the last century has been truly astounding, from the exotic (e.g., the cryovolcanic plumes on Enceladus) to the bizarre (e.g., Venusian tectono-volcanic coronae), and there is certainly more to come. These discoveries push the limits of knowledge of how interior processes manifest as volcanic products on planetary surfaces, thereby forcing revision of community assumptions about initial conditions and the physics behind magma transport, eruption, and subsequent emplacement of products. Hence, the study of volcanically-derived landforms on planetary surfaces not only informs the geologic history of the planetary bodies on which they are studied—it also bolsters our understanding of the physics of volcanic processes operating elsewhere in the solar system, including here on Earth. Furthermore, it hones the tools we use for predicting the nature of volcanism on bodies we've yet to explore, which in turn informs the science objectives and thus the instrument requirements when designing missions to explore new worlds.

The Moon has been a first step in many ways: it was the first outer world to be mapped, the first visited by spacecraft, the first visited by man, and it will most likely be the first on which we establish a permanent human presence. Samples of pyroclastic glass

from Taurus-Littrow collected during the Apollo 17 mission contain high abundances of ilmenite, thus rendering pyroclastic deposits as excellent targets for in situ extraction of oxygen for propellant and helium-3 for nuclear fission fuel (e.g., Hawke et al., 1990). In Chapter 2, I investigate the juvenile composition of small pyroclastic deposits on the Moon using their morphometries and estimate the volume of juvenile material present in each deposit. This information can be of great use in planning future in situ missions. In addition, I examine the consistency of my results with the current eruption model for small pyroclastic deposits and how it might be modified to accommodate the compositional and morphologic diversity among the deposits in my study.

As our knowledge of the physics behind the formation of volcanic morphologies improves, we learn how to distinguish between planetary landforms produced by volcanic processes alone and those produced by other processes including fluvial, aaeolian, tectonic, glacial processes, or any combination of these processes. Evidence of all of these processes have been identified on Mars. Of all the planets in our solar system, Mars is the most Earth-like: it hosts an active atmosphere, has undergone major climatic shifts, and has been subject to aqueous activity throughout its history. The well-preserved geology on the surface of Mars allows for investigation into its warm and watery past, when conditions on Mars were similar to those of prebiotic Earth, presenting a unique opportunity to study a period that has been nearly erased on Earth. Whether or not these conditions led to the emergence and preservation of life, as it did on Earth, begs the question of what the climate history of Mars is and, in particular, what the history of water on Mars might entail. In other words, how did Mars transition from a hospitable to hostile environment, and how did that change the type of aqueous activity present on the surface?

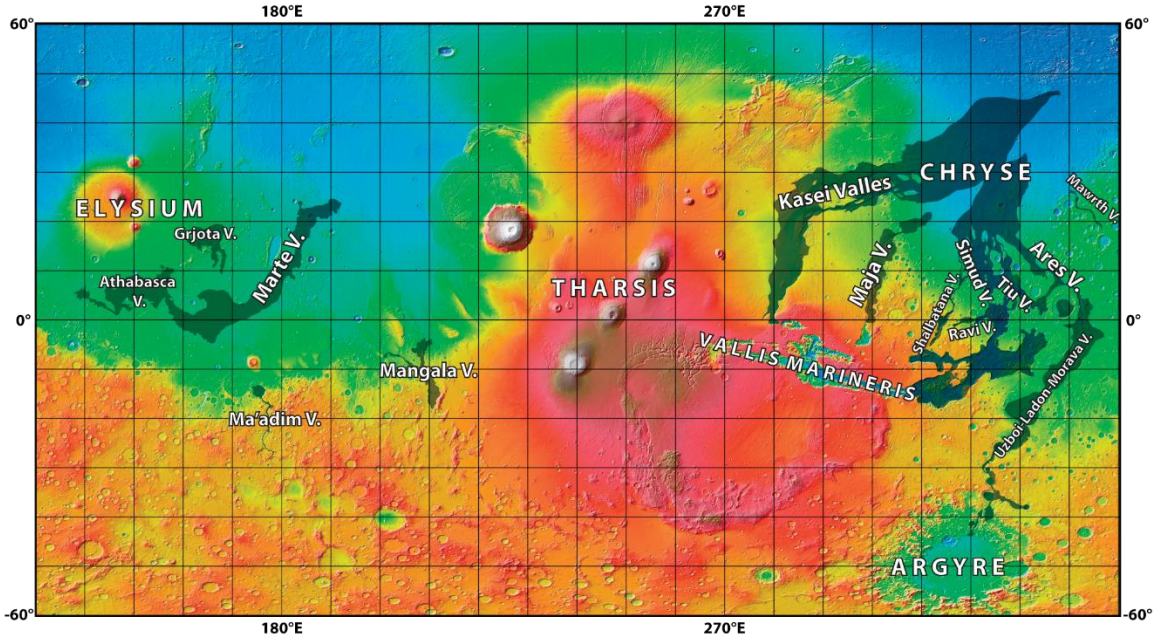

Figure 1.1. Global map of major outflow channels on Mars over a Mars Orbiter Laser Altimeter (Smith et al., 2001) colorized shaded relief basemap.

Outflow channels, or vast networks of fluvial features present on the martian surface generally believed to be the result of megaflooding events (Baker and Milton, 1974), are characteristic of this transitional period in Mars' history. Despite their importance as a potential marker of long-term global climate change, they are poorly understood: ongoing debate surrounds the origin, mechanism(s) and activity history of these regions. Their common location near the global topographic dichotomy boundary suggests that the nature of their formation is sensitive to the topography of the global cryosphere in addition to that of the surface, and recent studies of the recurrent fluvial and volcanic behavior of these channels (e.g., Jaeger et al., 2007) imply that there is an intimate relationship between local volcanism and flooding episodes. An understanding of the precise timing and global distribution of volcanic and fluvial events may provide insight into whether outflow activity has occurred as isolated systems in response to local stimuli, or has instead been associated with global geologic events, such as high-volume, planetary-

scale volcanic pulses or cryospheric response to changes in orbital obliquity (Mustard et al., 2001). In this way, outflow channels can act as a probe of the early history of Mars for answering outstanding questions about the evolution of climate during the transitional period.

In Chapters 3 and 4 I delve into the geologic history of two outflow channels: Mangala Valles and Maja Valles. In both studies, I have uncovered evidence of both fluvial and effusive volcanic activity and have constructed timelines using crater retention age dating suggesting that flooding episodes in these areas were related to, perhaps even triggered by, episodes of volcanism. Furthermore, Chapter 4 specifically addresses the controversial hypothesis that outflow channels may have formed by lava flow erosion, an idea that has gained traction since the identification of young lava flows draping the channels of Athabasca Valles (Jaeger et al., 2007).

The quality of our science in planetary geology is only as good as the data we use. Since much of planetary science data is collected optically, optical research is of tremendous importance for the advancement of technologies aiding planetary exploration. Chapter 5 outlines a solution to the issue of using out-of-focus thermal and visible images to determine object distance as applied to the Prox-1 low Earth orbit technology demonstration. I show that, despite image blur sourcing from both diffraction and defocusing, the THESIS/VIS subsystem is nevertheless capable of meeting the measurement requirements to achieve mission success.

Finally, Chapter 6 summarizes the findings presented in this dissertation.

CHAPTER 2

THE MORPHOMETRY OF LUNAR LOCALIZED PYROCLASTIC DEPOSITS

This chapter is a manuscript under review for publication in Earth and Planetary Science Letters with the following co-authors: M. S. Robinson and A. B. Clarke.

2.1. Introduction

Lunar dark mantle deposits (DMDs) are low-albedo, friable material dominantly found along highland-mare boundaries and are thought to be pyroclastic in origin (e.g., Carr, 1996; Schmitt et al., 1967; Wilhelms and McCauly, 1971; El-Baz, 1972; Sato, 1976). Although pyroclastic deposits represent a volumetrically negligible proportion of all volcanic material on the Moon, they may include some of the most primitive and volatile-rich components, and therefore are crucial for understanding lunar basaltic magmatism. Additionally, the high FeO content of these pyroclastic glasses has led to increased interest in their potential as a source of oxygen in future exploration endeavors (Allen, 2015). Previous workers (e.g., Head and Wilson, 1979; Gaddis et al., 1985) divided lunar pyroclastic deposits into two groups: "regional" (RDMDs), characterized by thin, flat blanketing deposits covering areas on the order of thousands of square kilometers, and "localized" (LDMDs), which are smaller (typically less than 100 km^2 in areal extent) with a resolvable positive topographic signature. The eruption mechanisms responsible for differences in RDMDs and LDMDs were evaluated by Head and Wilson (1979), who characterized both deposit types using photogrammetrically-derived topography from Apollo 16 Panoramic Camera images. The authors then compared their observations to

models of expected morphology resulting from various eruption types that may operate on the lunar surface. They proposed that wide dispersal of pyroclastic material characteristic of RDMDs is likely the result of the lunar equivalent of Strombolian-type activity (i.e., coalesced bubble explosions), while the proximal accumulation of coarse clasts and limited dispersal of fine ash particulates more closely resembles deposits resulting from Vulcanian-type eruptions involving explosive fragmentation of a solid, near-surface plug composed of wall rock material. The latter conclusion also relied heavily on the results of their volumetric measurements of six deposits and their vents in Alphonsus Crater, which indicated little or no juvenile component to the deposits, despite the low-albedo of the deposits compared to the surrounding crater floor. In particular, Alphonsus 1 (also known as Ravi) was calculated to have the smallest proportion of juvenile material, and was thus cited as the strongest indicator that LDMD deposits are composed chiefly of bedrock material, and that the eruption mechanism producing LDMDs must involve significant fracturing and entrainment of wall rock material.

This hypothesis influenced later interpretations of compositional groups of pyroclastic deposits that were categorized using spectra collected both telescopically (e.g., Gaddis et al., 1985; Hawke et al., 1985, 1989) and with the five-band Clementine ultraviolet-visible (UVVIS) instrument (Nozette, 1995) (e.g., Gaddis et al., 2000, 2003). It is therefore important to verify that the morphometric relationships described by Head and Wilson (1979) hold true for the Alphonsus deposits, given more contemporary data and methods, as well as for other LDMDs to confirm that their hypothesis indeed applies to all LDMDs. Later works revised RDMDs as being Hawaiian-type in origin, and instead

categorized cones (which are similar to LDMDs but with somewhat steeper slopes) as being Strombolian in origin (Head and Wilson, 2017).

Although the notion that LDMDs are products of lunar Vulcanian-like eruptions is generally accepted (e.g., Gaddis et al., 2003; Gustafson et al., 2012), the physical details of such events remain poorly constrained due to uncertainties related to the extent to which juvenile magma participates in the eruption and affects LDMD spectral reflectance in visible and near-infrared wavelengths. In order to better understand the nature of LDMD magma parent bodies and lunar mantle volatile content and composition using spectral reflection measurements, improved estimates of the volume of juvenile vs. bedrock material in LDMDs are necessary. The objective of this study is to determine how the relative proportions of bedrock and juvenile material vary in LDMDs as indicated by their deposit-to-vent-volume ratio and how the results compare with interpretations of deposit composition using remote sensing-based reflection spectra. Because the distinction between LDMDs and cones is poorly defined, we include cones in this study as well, and henceforth refer to the deposits in this study collectively as localized pyroclastic deposits (LPDs).

2.2. Methods

2.2.1 Volume estimates

We investigated the morphology of 23 LPD deposits from eleven sites across the Moon (Fig. 2.1) with the specific goal of quantifying the amount of juvenile magma in each deposit using the difference between the exterior tephra deposit volume and vent volume. Sixteen of the deposits are found in floor-fractured craters (Jozwiak et al., 2017):

Alphonsus crater, Oppenheimer crater, Gauss crater, Compton crater, and Schrödinger crater. Seven of the deposits are found at six sites located within mare: northeast Crisium, Birt, Isis, Lassell H, Osiris, and Tobias Mayer. These 23 sites were selected based on the topographic simplicity of the surroundings and the deposits themselves, the presence of a (preferably singular) central vent, and the availability of stereo images from the Lunar Reconnaissance Orbiter Camera (LROC) Narrow Angle Camera (NAC) (Robinson et al., 2010) for the production of high-resolution (~3–5 m horizontal pixel scale) Digital Terrain Models (DTMs) using SOCET SET (Henriksen et al., 2016). Since the vent slopes are steep (>20°), small uncertainties in slope can dramatically change the vent volume estimates. Where gaps in NAC DTM coverage on the surrounding LPD deposit exist, they were filled using data from the 60°S to 60°N 512 PPD Lunar Orbiter Laser Altimeter (LOLA) (Smith et al., 2010) and SELENE Terrain Camera merge (Haruyama et al., 2014; Barker et al., 2016). Since this product does not cover Schrödinger Crater, gaps at that location were instead filled using the LOLA global DTM.

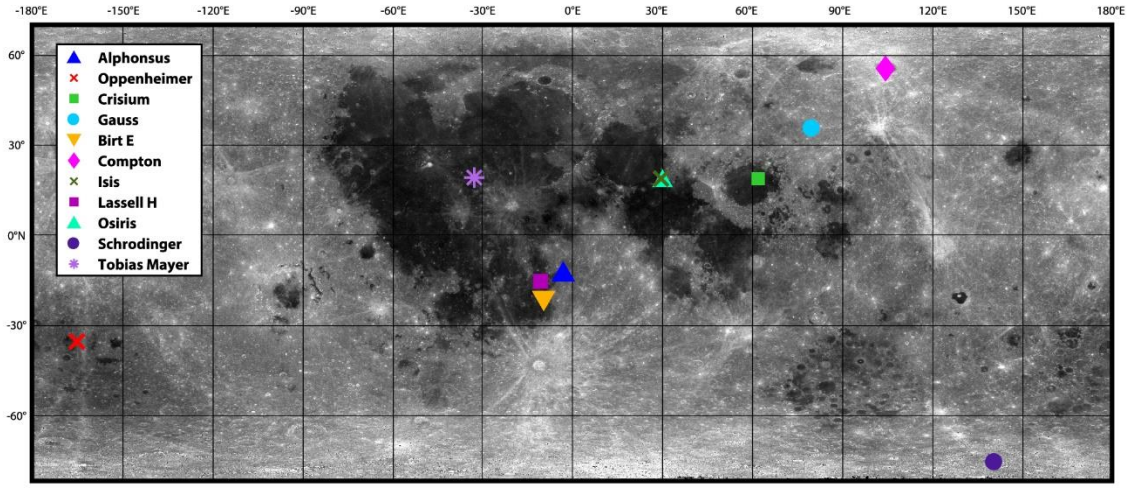

Figure 2.1. Locations of the eleven LPD sites included in this study on a global 643 nm WAC mosaic (Boyd et al., 2013).

To determine the volume of each deposit, we first synthesized a corresponding DTM of an estimated pre-depositional surface based on the pre-existing topography exposed around the deposit, profiles across the deposit, and exposed stratigraphy as seen in NAC images. Deposit boundaries were determined from reflectance and FeO contrasts with the surrounding terrain from a 100m pixel scale photometrically normalized map produced from observations at 643 nm by the LROC Wide Angle Camera (WAC) (Boyd et al., 2013) and the global Clementine UVVIS iron abundance map (Lucey et al., 1995), respectively. The boundaries were checked with low-incidence angle NAC images where available. The pyroclastic unit was then masked from the DTM and a new surface was generated using the ArcMap Spline tool (ESRI 2011), which generates a minimum curvature surface. This method was especially useful for modeling LPDs overlying rilles and fractures, which we assume existed prior to deposit emplacement. Since rille topography tends to be more irregular than inter-rille topography, in most cases we employed one or a combination of three strategies for extrapolating the rille topography: (1) using a simple linear model connecting the rille on one side of the deposit to the other, (2) applying the slope of the extrapolated topography outside of (and parallel to) the rille to the bottom of the rille, or (3) using representative profiles to determine a deposit thickness profile outside of the rille, and then subtracting that thickness profile from the present rille topography (Fig. 2.2).

Once a model of the pre-existing surface was produced (Fig. 2.2g), it was then subtracted from the present-day NAC DTM (Fig. 2.2a) containing the deposit, resulting in a surface difference DTM (Fig. 2.2i). In the difference DTM, positive values (shown in red) indicate deposit thickness and negative values (shown in blue) are vent depth values.

The difference DTM guided the choice of rille extrapolation strategy, as we expect the thickness of the deposit to smoothly decrease radially outward form the vent rim. The vent volume is the volume calculated by integrating the negative values of the difference DTM in the vent area, and the deposit volume is calculated by integrating the positive values of the entire difference DTM.

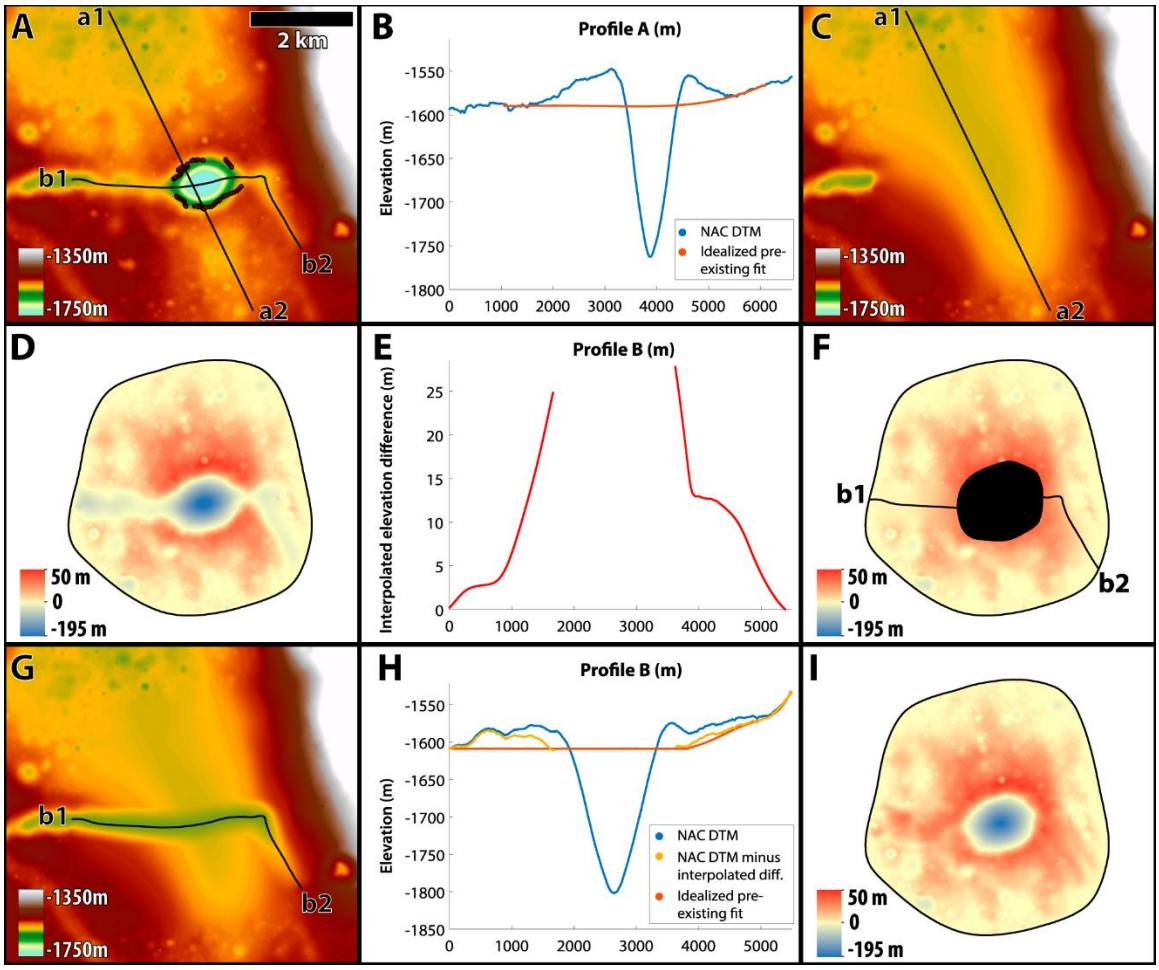

Figure 2.2. Example of pre-existing surface derivation at Alphonsus 2 using NAC DTM profiles. A representative topographic profile a1–a2 (shown in panel A) was used to produce a model profile of the pre-existing surface without the rille (panel B). That profile is then used to interpolate a 3D surface (panel C). That surface is then subtracted from the NAC DTM (panel D), the rille removed, and the missing area interpolated to produce a new difference (or thickness) DTM (panel F, thickness profile along rille shown in panel E). The thickness profile extracted from the interpolated difference DTM is then subtracted from the NAC DTM and used to produce a best-guess model profile of the rille floor (panel H). That profile is then incorporated into a new 3D model of the pre-existing surface including the rille (panel G, final difference (i.e., thickness) DTM shown in panel I).

This method allows for minimization of uncertainties resulting from complicating underlying topography, such as slopes, rilles, and/or scarps. Minimization of these uncertainties is of particular importance given the low-lying, low-relief nature of LPDs, and produces more realistic surface difference DTMs than when a simple flat plane is used.

After making volume estimates, we calculate the dense-rock equivalent (DRE) volume, which scales the deposit volume down to the equivalent bedrock volume. For the purposes of this study, we define bedrock to be the floor material (country rock) onto which the deposit has been emplaced. Given a deposit whose volume ($V_{deposit}$) exceeds the volume of its vent (V_{vent}), we used the following equation:

$$V_{juvenile,DRE} = V_{deposit}\frac{\rho_{deposit}}{\rho_{bedrock}} - V_{vent}$$

The result can then be used to determine the proportion of juvenile material in the deposit:

$$\%\ juvenile = 100 * \frac{V_{juvenile,DRE}}{V_{deposit}\frac{\rho_{deposit}}{\rho_{bedrock}}}$$

This is a modification of the equation presented by Head and Wilson (1979) that adjusts the volume of the fragmented and deposited bedrock material that was displaced to create the vent crater during eruption. For $\rho_{deposit}$, we used the bulk density of a sample of orange beads from Taurus-Littrow as measured by Gold et al. (1976), 1.4 g/cm^3. The range of values used for $\rho_{bedrock}$ varied by deposit location. For deposits located in floor-fractured craters, we used the density of pure anorthite as a dense endmember (2.7 g/cm^3), and the bulk density range of lunar impact breccias reported by Kiefer et al. (2012), 2.3–2.6 g/cm^3. For deposits situated on mare, we used 3.0–3.3 g/cm^3 (Kiefer et al., 2012), the upper end of which is extreme. When the volume of the vent exceeds the volume of the deposit, the

expression returns a negative value, indicating negligible volume of juvenile material in the deposit.

2.2.2 Sources of uncertainty

Reported errors in juvenile percentages include bedrock density and DTM uncertainties. The uncertainty of NAC DTMs is given by the relative linear error value as calculated by SOCET SET, which uses the image ground sampling distance, convergence angle, and image matching uncertainty of the model to derive a vertical uncertainty for each DTM (typically less than 5 meters) (Henriksen et al., 2016). The global LROC-SELENE DTM that was used for gaps in our NAC DTMS has a vertical accuracy of 3–4 m (Barker et al., 2016). Volumetric uncertainties were derived by multiplying the vertical uncertainty of the NAC DTM by area of the deposit it covers, and then adding the area of any gaps multiplied by 4 m to that value.

There are several systematic errors that are not accounted for in our uncertainty calculations and are not represented by the error bars in subsequent plots. For example, we did not account for increased porosity of the bedrock material upon caprock fragmentation. Without a representative sample or details about the eruption mechanics, we cannot know the shape or size distribution of the fragments that would have resulted from the caprock. Additionally, the bulk density value used for the deposit material is sourced from the only sample of an in-situ pyroclastic deposit that we have in the Apollo sample collection. Thus, we do not know whether its bulk density is representative of all pyroclastic deposits. Similarly, fallback of material into the vent during and after eruption would serve to exaggerate juvenile estimates, but without any knowledge of the volume of tephra that

receded into the vent, we cannot estimate how much of an impact this has in our calculations. Any post-eruptive subsidence resulting from evacuation of the magmatic plumbing system would also influence volumes in unpredictable ways. Another influence on our estimates is the accuracy of our estimated pre-existing surfaces. Examples of particularly complex sites from our dataset include Compton W, Gauss 2, and Oppenheimer 3, therefore the reconstructed surfaces at these sites likely have the largest errors (see section 2.3 for sensitivity analysis of pre-existing surfaces to errors).

Since LPDs are pre-Imbrian (>3.85 Ga) to Imbrian (~3.85–3.2 Ga) in age (Head, 1974), we must consider the effect of regolith development on the albedo and morphology of LPDs. The model presented by Gault et al. (1974) indicates that a 3.8 Gy aged surface has been turned over at least once to a depth of 1.2 meters, 10 times at 70 centimeters, and 100 times at 10 centimeters. A 4 Gy surface would have been turned over to a depth of 10 meters. The accumulation rate of material derived from 1 meter or more away at the lunar landing sites is estimated to be 6.8 mm/Myr (Arvidson et al., 1975; Melosh, 1989), equivalent to about 25 meters for a 3.8 Ga surface. Considering the extremely shallow slopes of LPDs, regolith turnover therefore may have dramatically reduced the albedo of and buried the edges of the deposits, causing the apparent edge of the deposit to recede towards the vent over time, thereby leading to greater uncertainty as to the true areal extent of the deposit. Since the majority of the tephra volume is near the vent for all deposits, the impact of the areal uncertainty due to mixing at the edges on juvenile proportion calculations may not be important. However, since our average thickness values are calculated by dividing the deposit volumes by their areas, underestimates in deposit areas would result in average thickness overestimates. Regolith production would also mute the

topographic signature of the deposits by shallowing their slopes and causing slumping of additional deposit material into the vent. Without more precise knowledge about regolith development at each site, we cannot precisely measure the importance of its effects on our volume measurements, though it may have caused us to underestimate deposit volumes.

Deposit Name	Latitude (°N)	Longitude (°E)	Exposure description
Alphonsus 1	-12.51	358.04	Some grain flow patches
Alphonsus 2	-12.54	358.28	Potential outcroppings of discrete surface (Fig. 2.3a)
Alphonsus 4	-12.86	358.38	Possible surface obscured by creep
Alphonsus 5	-13.09	358.39	No compelling exposures
Alphonsus 6	-13.57	355.92	Fairly consistent max elevation of bright grain flow patches, no structural indication of layer (Fig. 2.3b)
Alphonsus 7	-13.51	358.55	Some grain flow patches
Alphonsus 8	-14.39	358.09	Possible surface obscured by creep
Alphonsus 9, 10, 11	-13.78	356.62	Discrete surface identified in 11, one surface exposure in 10, grain flow patches in 9
Oppenheimer 1	-37.10	195.42	No compelling exposures
Oppenheimer 2	-33.55	194.52	Bight band of blocky material
Oppenheimer 3	-35.30	196.75	No compelling exposures
Oppenheimer 4	-34.96	196.58	No compelling exposures
Crisium 1	18.55	61.91	No compelling exposures
Crisium 2	19.08	61.20	No compelling exposures
Gauss 1	35.87	76.65	One grain flow feature, no indication of stratigraphical interface
Gauss 2	36.30	81.50	No compelling exposures
Birt E	-20.73	350.36	Possible surface identified
Compton W	54.10	105.39	No compelling exposures
Isis	18.97	27.47	No compelling exposures
Lassell H	-15.00	349.13	No compelling exposures
Osiris	18.64	27.64	No compelling exposures
Schrodinger	-75.40	138.60	Structural indications of interface present on both sides of vent (Fig. 2.3c)
Tobias Mayer W	19.20	327.50	Possible surface identified

Table 2.1. Descriptions of exposures of wall rock material within the vents.

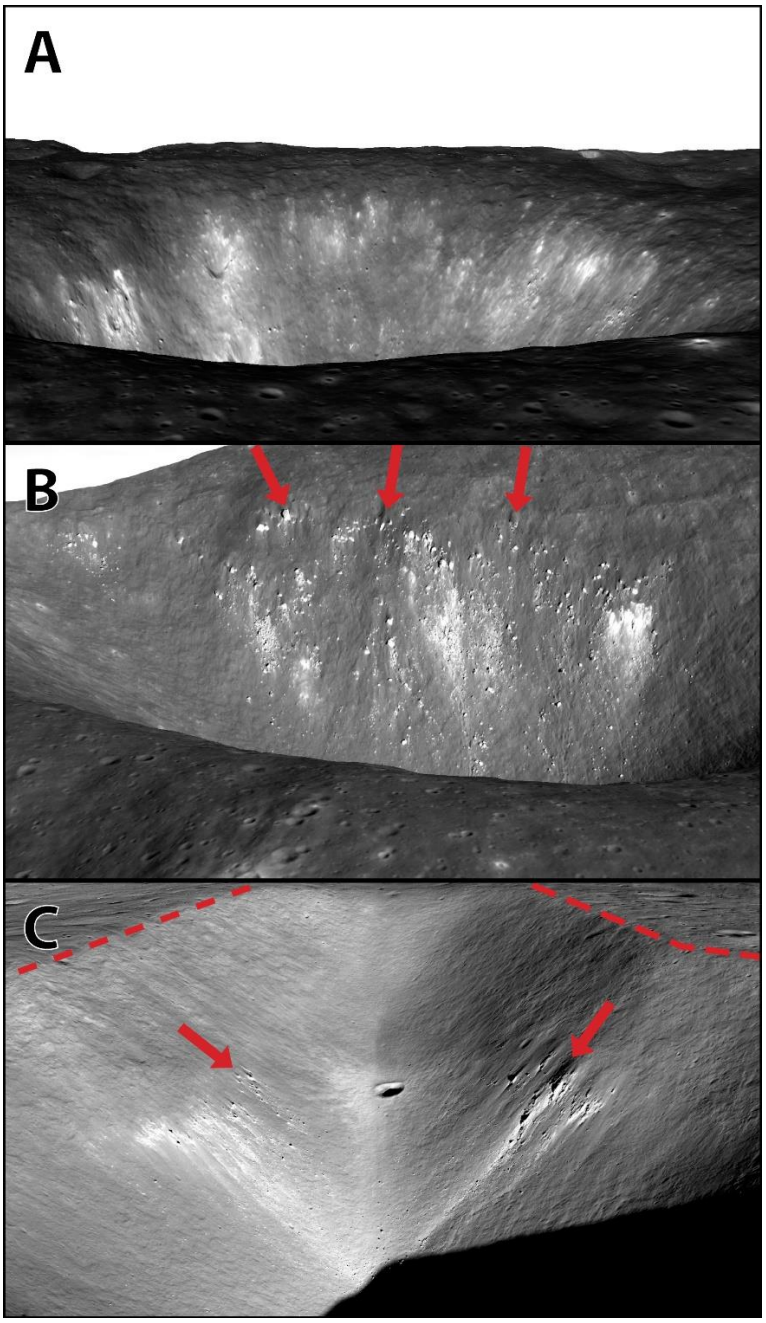

Figure 2.3. A) Perspective view of the eastern wall of Alphonsus 6 vent with a series of grain flows of no clear structural origin. The source of erosion in some cases appears to have been overrun by the fine dark deposit material (NAC orthophoto, width of view ~1500 m, vertical exaggeration 2.8x). B) Perspective view of the western wall of Alphonsus 11 vent showing structural benches appearing to source from an interface between the original surface and the deposit (NAC orthophoto, width of view ~1550 m, vertical exaggeration 2.1x). C) Perspective view down the axis of the vent toward the southwest. Red dashes outline the vent rim, which are parallel to linear benches of eroding material on both sides of the vent (indicated by arrows) that likely represent a stratigraphic interface. (NAC image, width of view ~5200 m, vertical exaggeration 1.5x).

2.2.3 Outcrops and sensitivity analysis

About half of the vents in this study exhibit linear blocky textures partially down the wall that we interpret as exposed outcrops of the sub-deposit bedrock revealing the maximum depth of the overlying pyroclastic deposit (Table 2.1, Fig. 2.3). In a few cases, aligned exposures of mass wasting materials sourced from eroding benches indicate a discrete stratigraphic interface interpreted to represent the pre-existing surface. These outcrops present an opportunity to test our methodology of approximating the pre-existing surface.

To investigate the sensitivity of our results to our estimates of the pre-existing surface, we created alternative pre-existing surface models (which we'll call reconstructed surface B) for three deposits containing deliberate topographic modifications representing extreme, but still realistic, cases (Fig. 2.4). We then use the locations of observed outcrops on the vent walls to show that the surface generated using our methods (reconstructed surface A) previously outlined is more likely.

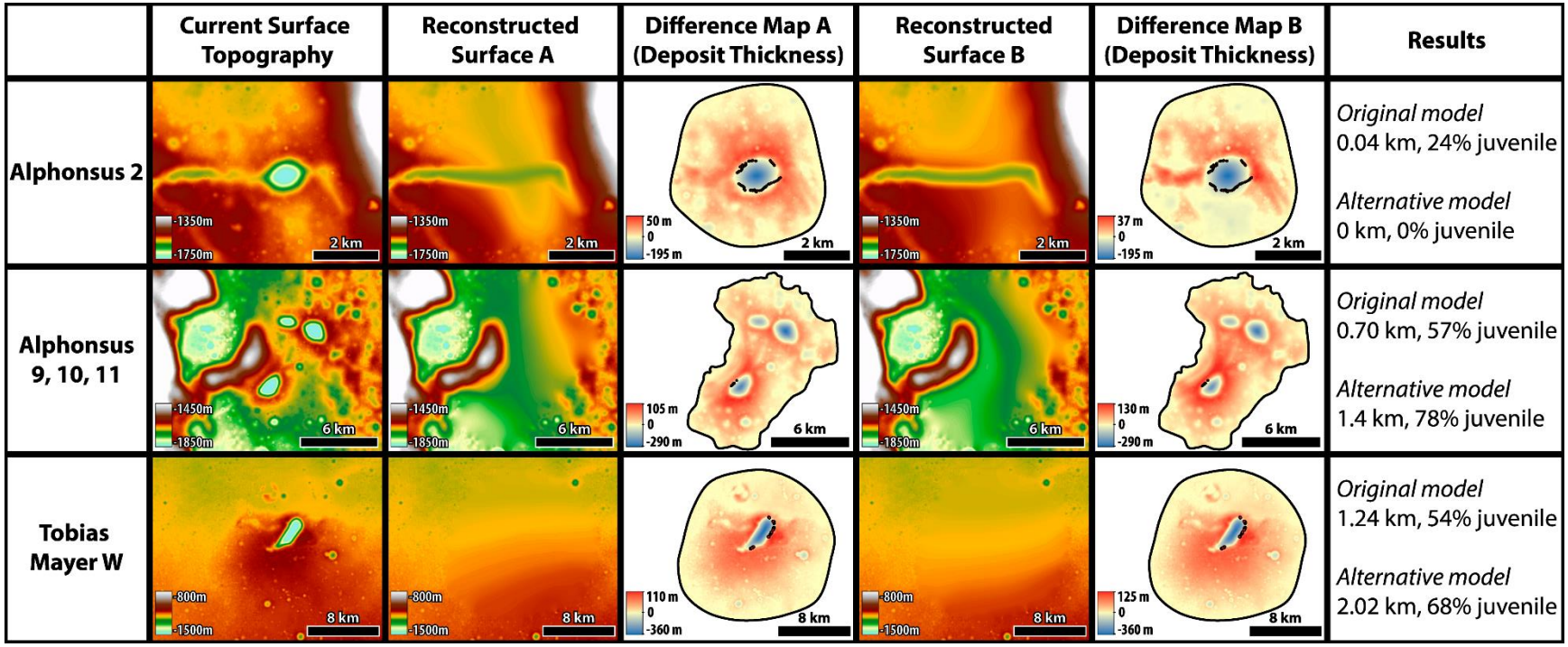

Figure 2.4. Summary table of the results of the sensitivity of our results to changes in the shape of our pre-existing surface models. Alternative surfaces are designed to represent extreme, yet realistic, cases. Black dots denote locations of identified outcrops interpreted as marking the interface between the deposit and the underlying country rock; they broadly agree more with the original model surfaces produced following our methodology.

Alphonsus 2

Reconstructed surface A (as shown in Fig. 2.2) relied heavily on a topographic profile (Fig. 2.2b) across the deposit and extrapolation from the topography outside of the deposit to a minimum-curvature profile. If we remove this step and instead assume, as an extreme alternative, that the small depression north of the rille sloped up more steeply north of the rille (reconstructed surface B), the difference (thickness) map B is much more irregular than difference map A. Moreover, the locations of blocky outcrops (indicated by black dots) on difference map A are noticeably closer to the plane of 0 thickness (white in the difference/thickness DTM), where the model indicates an interface should be visible. Of the three deposits tested, the difference in the calculated juvenile proportion from reconstructed surface A to reconstructed surface B was the most dramatic for Alphonsus 2, decreasing from 24% to 0%.

Alphonsus 9, 10, 11

For this deposit, there is uncertainty in the shape of the contours on the floor. Reconstructed surface A exhibits contours following the convex shape of the gently sloping larger crater floor toward the east. However, it is also possible that the contours instead more closely follow the shape of the more prominent ridge hugged by the deposit toward the west, in sharp contrast with the larger-scale topography of the crater floor (reconstructed surface B). Reconstructed surface B results in a difference/thickness map that looks rather similar to difference map A, only thicker and more diffusely distributed. The outcrops once again align more favorably with difference map A. Nevertheless, the

difference map B yields a juvenile proportion of 78%, about 21% greater than the calculated estimate from difference map A.

Tobias Mayer W

In terms of contextual topography, Tobias Mayer is one of the simplest deposits. Similar to the Alphonsus 9/10/11 deposit, reconstructed surface A has contours following the wide convex downsloping character of the surrounding topography. Therefore, the logical extreme alternative is an oppositely concave surface (reconstructed surface B). Difference map B once again looks similar to that of difference map A, albeit generally thicker. The exposed outcrops agree with both models roughly equally. This alternative surface example had a smaller impact on the calculated juvenile proportion than was found in the previous two examples, having an increase of about 12% from 54% to 68%.

These analyses demonstrate the importance of careful consideration of surrounding topography when generating pre-existing surfaces. It shows that in the worse cases, errors in reconstructed surfaces may be as high as ±25%.

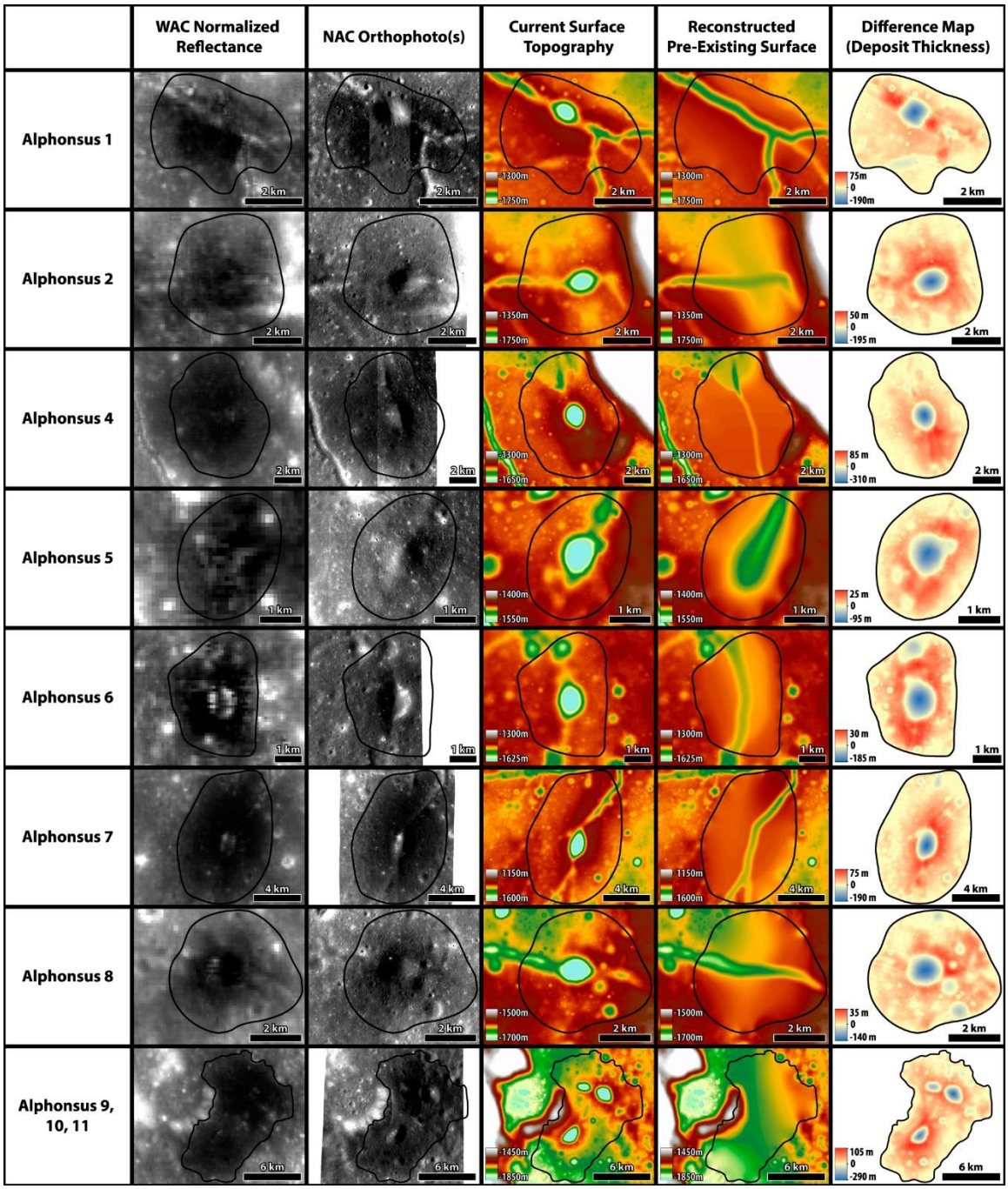
WAC Normalized Reflectance
NAC Orthophoto(s)
Current Surface Topography
Reconstructed Pre-Existing Surface
Difference Map (Deposit Thickness)
Alphonsus 1
Alphonsus 2
Alphonsus 4
Alphonsus 5
Alphonsus 6
Alphonsus 7
Alphonsus 8
Alphonsus 9, 10, 11

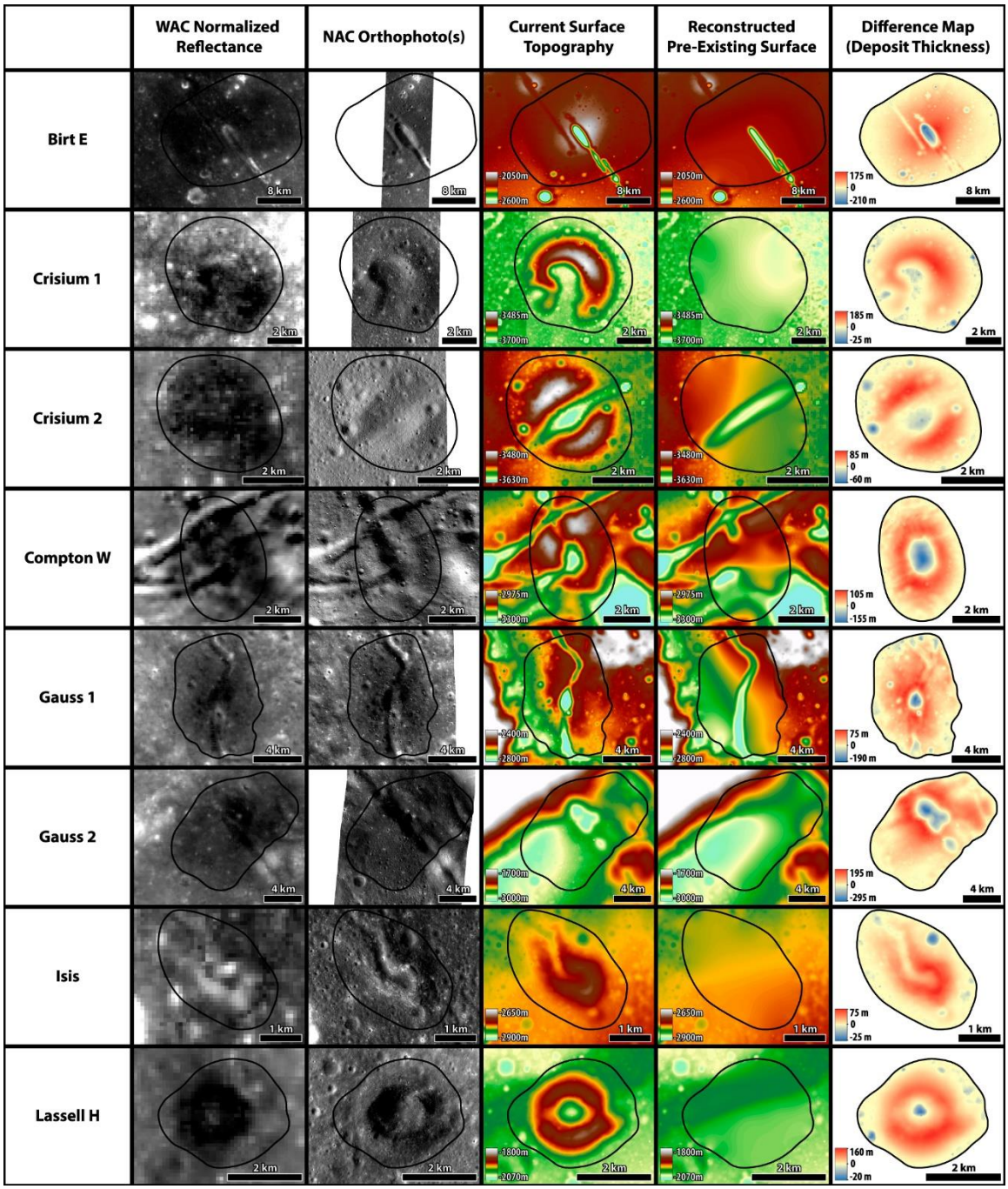
WAC Normalized Reflectance
NAC Orthophoto(s)
Current Surface Topography
Reconstructed Pre-Existing Surface
Difference Map (Deposit Thickness)
Birt E
Crisium 1
Crisium 2
Compton W
Gauss 1
Gauss 2
Isis
Lassell H
-2050m
-2600m
175 m
0
-210 m
-3485m
-3700m
185 m
-25 m
-3480m
-3630m
85 m
-60 m
-2975m
-3300m
105 m
-155 m
-2400m
-2800m
75 m
-190 m
-1700m
-3000m
195 m
-295 m
-2650m
-2900m
-1800m
-2070m
160 m
-20 m
1 km
2 km
4 km
8 km

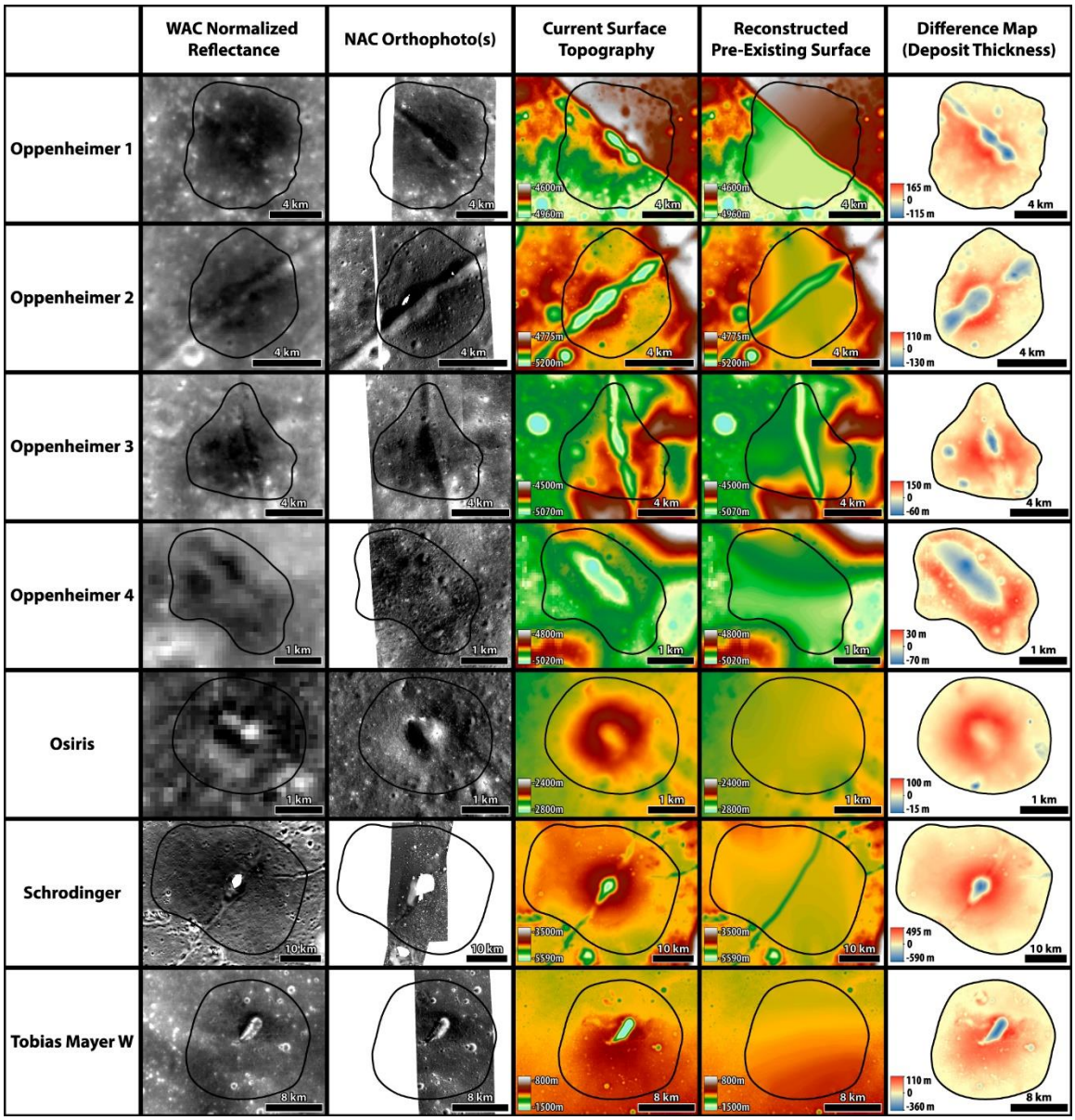

Figure 2.5. Graphic tables presenting the current surface appearance and topography of the LPDs in this study alongside our pre-existing surface model and the difference/deposit thickness DTM corresponding to each deposit. Areas not covered by NAC DTMs are filled in with the WAC-Kaguya global DTM. NAC DTM coverage is equal to the orthophoto coverage shown in the second column.

Deposit Name	Area (km^2)	Deposit Volume (km^3)	Vent Volume (km^3)	Juvenile Volume (DRE) (km^3)	% Juvenile	Maximum Deposit Thickness (m)	Average Deposit Thickness at Vent (m)	Maximum Vent Depth (m)	Average Deposit Thickness (m)	Notes
Alphonsus 1	35	0.416 ± 0.088	0.146 ± 0.005	0.089 ± 0.070	32.2 ± 20.9	74 ± 3	31 ± 3	187 ± 3	12 ± 3	MD Ravi (Head and Wilson, 1979)
Alphonsus 2	20	0.212 ± 0.049	0.083 ± 0.003	0.038 ± 0.038	24.2 ± 24.2	49 ± 3	36 ± 3	193 ± 3	11 ± 3	Monira (Head and Wilson, 1979)
Alphonsus 4	46	0.723 ± 0.117	0.286 ± 0.007	0.121 ± 0.099	25.4 ± 18.6	85 ± 3	42 ± 3	311 ± 3	16 ± 3	KC Soraya (Head and Wilson, 1979)
Alphonsus 5	6	0.030 ± 0.014	0.024 ± 0.002	0.002 ± 0.002	7.9 ± 7.9	23 ± 3	13 ± 3	93 ± 3	5 ± 3	
Alphonsus 6	11	0.090 ± 0.030	0.092 ± 0.004	0	0	29 ± 3	20 ± 3	185 ± 3	9 ± 3	
Alphonsus 7	71	1.022 ± 0.106	0.343 ± 0.005	0.231 ± 0.103	38.2 ± 11.4	72 ± 2	50 ± 2	272 ± 2	15 ± 2	R (Head and Wilson, 1979)
Alphonsus 8	18	0.117 ± 0.033	0.069 ± 0.003	0.012 ± 0.012	12.9 ± 12.9	36 ± 2	18 ± 2	139 ± 2	7 ± 2	
Alphonsus 9, 10, 11	92	2.134 ± 0.177	0.264 ± 0.005, 0.065 ± 0.002, 0.170 ± 0.003	0.697 ± 0.192	57.2 ± 7.4	107 ± 2	55 ± 2, 54 ± 2, 83 ± 2	290 ± 2, 145 ± 2, 246 ± 2	25 ± 4	CA (Head and Wilson, 1979)
Oppenheimer 1	70	2.134 ± 0.227	0.157 ± 0.010	1.040 ± 0.219	86.3 ± 3.2	163 ± 3	80 ± 3	116 ± 3	32 ± 3	Oppenheimer N (Bennett et al., 2016)
Oppenheimer 2	35	0.588 ± 0.058	0.109 ± 0.007, 0.076 ± 0.004	0.144 ± 0.066	41.5 ± 13.2	107 ± 2	75 ± 2, 27 ± 2	110 ± 2, 86 ± 2	20 ± 2	Oppenheimer SSE (Bennett et al., 2016)
Oppenheimer 3	40	1.522 ± 0.073	0.028 ± 0.002	0.823 ± 0.102	96.6 ± 0.6	147 ± 2	91 ± 2	58 ± 2	39 ± 2	Oppenheimer E (Bennett et al., 2016) (not to be confused with Opp. E Crater)
Oppenheimer 4	5	0.035 ± 0.008	0.020 ± 0.002	0.004 ± 0.004	13.9 ± 13.9	31 ± 2	15 ± 2	70 ± 2	9 ± 2	
Crisium 1	33	1.242 ± 0.044	0.004 ± 0.001	0.550 ± 0.040	99.2 ± 0.3	185 ± 1	92 ± 1	20 ± 1	39 ± 1	
Crisium 2	12	0.219 ± 0.012	0.006 ± 0.001	0.092 ± 0.011	93.7 ± 1.3	85 ± 1	46 ± 1	37 ± 1	19 ± 1	
Gauss 1	87	2.982 ± 0.330	0.042 ± 0.006	1.632 ± 0.305	97.3 ± 0.8	136 ± 4	97 ± 4	100 ± 4	34 ± 4	Gauss W (Gaddis et al., 2003) (not to be confused with Gauss W Crater)
Gauss 2	108	5.165 ± 0.240	0.712 ± 0.017, 0.076 ± 0.004	2.098 ± 0.354	72.2 ± 3.9	195 ± 2	137 ± 2, 48 ± 2	296 ± 2, 127 ± 2	51 ± 2	Gauss E (Gaddis et al., 2003) (not to be confused with Gauss E Crater)
Birt E	356	14.856 ± 1.176	0.554 ± 0.016	6.088 ± 0.855	91.5 ± 1.3	214 ± 2	160 ± 2	173 ± 2	42 ± 3	Large deposit only (small northeastern deposit excluded from calculations)
Compton W	15	0.420 ± 0.040	0.080 ± 0.004	0.155 ± 0.042	64.7 ± 7.4	104 ± 3	75 ± 3	155 ± 3	31 ± 3	
Isis	6	0.098 ± 0.030	0	0.044 ± 0.016	100	77 ± 5	56 ± 5	0	16 ± 5	
Lassell H	7	0.333 ± 0.019	0.001 ± 0.000	0.148 ± 0.016	99.3 ± 0.3	158 ± 3	118 ± 3	19 ± 3	45 ± 3	
Osiris	5	0.151 ± 0.027	0	0.068 ± 0.015	100	102 ± 5	78 ± 5	0	28 ± 5	
Schrodinger	877	103.320 ± 1.516	3.326 ± 0.019	54.354 ± 5.724	94.2 ± 0.6	496 ± 3	436 ± 3	591 ± 3	119 ± 2	
Tobias Mayer W	232	4.985 ± 0.613	0.992 ± 0.012	1.242 ± 0.390	54.2 ± 8.3	110 ± 2	78 ± 2	360 ± 2	22 ± 3	

Table 2.2. Volume measurement results and calculations. Cells with multiple values are reporting the values for each vent within a multi-vent deposit. The ranges presented for % juvenile account for variations in bedrock density and LOLA uncertainties alone, and do not represent statistical uncertainties.

2.3. Results

Presented in Figure 2.5 is a graphic table of our reconstructed pre-existing surfaces (equivalent to surface A in Fig. 2.4) for each LPD and their resulting difference maps. Volume measurements, calculated juvenile volumes and percentages, and other morphometric measurements and calculations can be found in Table 2.2. Deposits containing multiple vents were treated as a single deposit when calculating the juvenile content, with V_{vent} being the sum of the individual vent volumes. Although we combined the deposit volumes for all other multi-vent deposits, vent depths and deposit thicknesses immediately surrounding the vents were still performed on an individual basis and are presented as multiple values for their respective deposits. The average deposit thicknesses near each vent were calculated by averaging the thickness values along the apex of the vent rim. The overall average deposit thickness is the volume of the deposit divided by the area of the deposit (vent area subtracted). We note that while Birt E is a multi-vent deposit, NAC DTM coverage does not include the smaller northwestern vent, thus its volume has been excluded from our numbers for Birt E.

Results show a wide variety of morphometric characteristics among deposits, with juvenile proportions spanning the entire range of 0–100%. There were four deposits that returned negative values for some or all bedrock densities considered. Oppenheimer 4 and Alphonsus 2, 5, and 8 exhibit error bars extending below 0 for the higher density ranges. Alphonsus 6, however, returned negative values for all densities considered. This may be

explained in part by the exclusion of the large cavity in the northern portion of the current surface from our pre-existing surface model, since it appears to be a topographic anomaly whose original depth is difficult to estimate. Therefore, the volume of Alphonsus 6 is an underestimate due to the mass unaccounted for in the cavity. The return of negative values for greater bedrock densities for all five deposits may indicate that we are systematically underestimating deposit volumes (due to muting of the landscape during regolith development, for example), or that the density contrast between the country rock is better represented by the smaller of the range of values, or both.

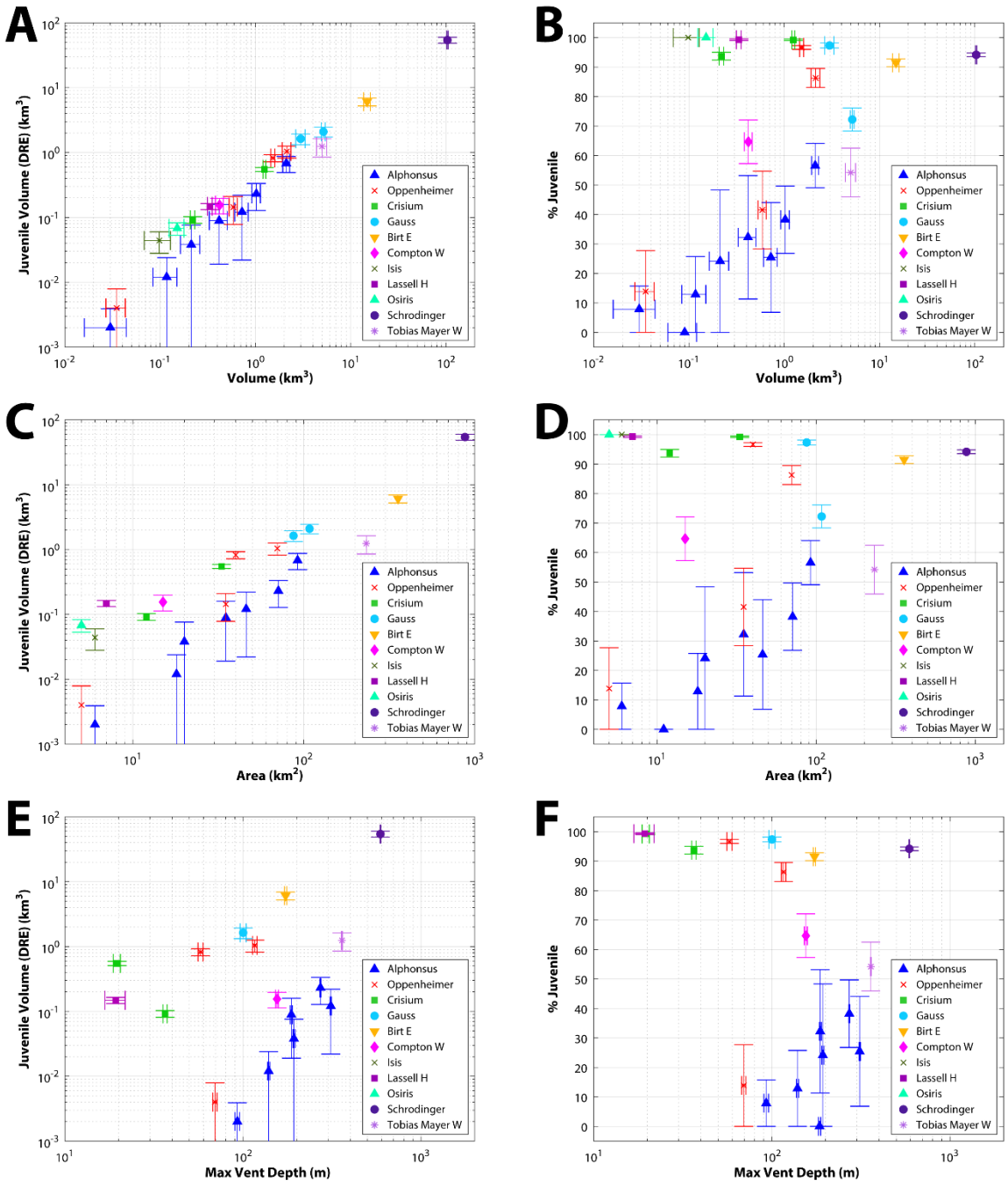
A
Juvenile Volume (DRE) (km³)
Volume (km³)
B
% Juvenile
Volume (km³)
C
Juvenile Volume (DRE) (km³)
Area (km²)
D
% Juvenile
Area (km²)
E
Juvenile Volume (DRE) (km³)
Max Vent Depth (m)
F
% Juvenile
Max Vent Depth (m)
Alphonsus
Oppenheimer
Crisium
Gauss
Birt E
Compton W
Isis
Lassell H
Osiris
Schrodinger
Tobias Mayer W

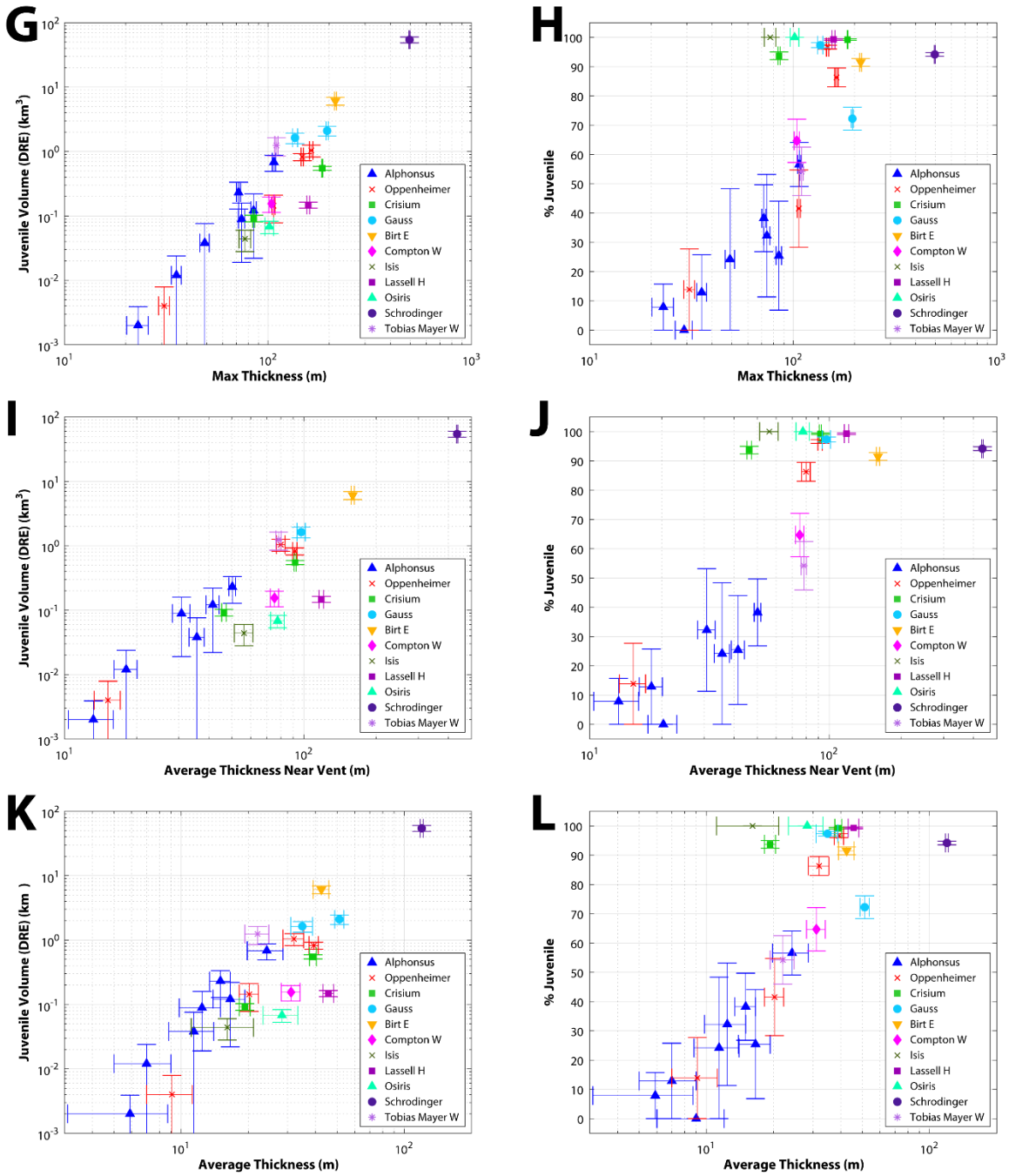

Figure 2.6. Plots depicting relationships between juvenile volume/proportion and various morphometrics. Vertical errors are derived from the range of bedrock densities expected and the volume errors calculated using the vertical precision of the DTMs. Horizontal uncertainties are derived from the latter alone. Multi-vent deposits are not plotted in max vent depth nor average thickness near vent since each deposit contains multiple values for those metrics.

2.4. Discussion

2.4.1 Morphometric relationships

Figure 2.6 shows the relationships between the calculated volume/proportion of juvenile material and the morphometric properties for each deposit presented in Table 2.2. There is a weak positive logarithmic relationship between the proportion of juvenile material and both total deposit volume (Fig 2.6b, R^2=0.72) and area (Fig. 2.6d, R^2=0.56) for deposits containing less than ~80% juvenile material. These relationships are much tighter and more consistent for absolute juvenile volume (Fig. 2.6a, R^2=0.96 and Fig. 2.6c, R^2=0.78, respectively). The relationship with vent depth and percent juvenile material (Fig. 2.6f), on the other hand, appears to be positive for deposits composed of less than 50% juvenile material and negative for deposits composed of greater than 50% juvenile material.

The maximum vent depth and the absolute juvenile volume of Alphonsus deposits appear to be tightly positively correlated (Fig. 2.6e). The remaining vent depths also show a positive correlation with absolute juvenile volume, but they do not fall on the same trend and are generally more scattered. Maximum deposit thickness (Fig. 2.6g,h), average deposit thickness near the vent (Fig. 2.6i,j), and average overall thickness (Fig. 2.6k,l) are all positively correlated with total juvenile volume and juvenile percentage. While there is some clustering of deposits from the same locations on these charts, particularly the Alphonsus deposits, geomorphic characteristics do not appear to be strongly dictated by location. Instead, the relationships suggest that LPD deposit size is controlled by the proportion of juvenile magma that participated in the eruption. While the observation by Wilson and Head (1979) that the deposits at Alphonsus Crater are low in juvenile content

is generally consistent with our measurements, it appears that those deposits represent only part of a larger morphometric trend for localized pyroclastic deposits.

2.4.2 Comparison with remote sensing studies

Spectral observations from the Moon Mineralogy Mapper (M^3) aboard Chandrayaan-1 (Pieters et al., 2009) and the Diviner Lunar Radiometer Experiment aboard the Lunar Reconnaissance Orbiter (Paige et al., 2010) together allow for much more precise measurement of iron-bearing minerals and glasses compared to Clementine-based results. Using these datasets, Bennett et al. (2016) found that the Oppenheimer 1 and 3 deposits bear strong glass signatures with traces of clinopyroxene (interpreted as juvenile material), with Oppenheimer 3 in particular exhibiting spectral characteristics suggesting that it is nearly entirely composed of glass, consistent with our morphometric-based estimates that these deposits are likely almost entirely juvenile. On the other hand, Oppenheimer 2 was found by Bennett et al. (2016) to be a mixture of glass and clinopyroxene. This finding conflicts with our results for this deposit, which indicate that it should be composed of a roughly equal mixture of juvenile material (glass and clinopyroxene) and crater floor material (orthopyroxene). However, failure to detect orthopyroxene by spectral methods does not necessarily indicate its absence in the deposit, only that it is probably not present in detectable quantities on the surface of the deposit (i.e., late stage erupted products might be entirely juvenile). Finally, Oppenheimer 4 was only faintly detectable in glass band depth parameters (Bennett et al. 2016), suggesting that it contains very little glass, though with a surface area of only 5 km^2, it may simply be too small for a signature to be visible through the noise in their M^3 glass band depth map.

Gaddis et al. (2016) also used M^3 data to analyze the deposits in Alphonsus crater. Their findings indicate that all of the deposits in the crater are othropyroxene-rich, but the largest deposits (Alphonsus 1, 4, 7, 9, 10, and 11) also contain mixtures of clinopyroxene and glass. In particular, the western cluster of vents (9–11) contain a significant glass+orthopyroxene component, particularly near the southern deposit (11). Another recent study (Allen et al., 2013) applying M^3 and Diviner data to LPDs in Alphonsus Crater found elevated abundances of FeO in the deposits (13.8 ± 3.3 wt.%) compared to that of the crater floor material (7.5 ± 1.4 wt.%) yet within the range of iron oxide abundances measured in pyroclastic glasses (Papike, 1998). The results of these studies are consistent with our results, which show very little to no juvenile material for the smallest deposits (by area) and moderate to significant juvenile component (~20–60%) for the larger deposits in Alphonsus crater.

Finally, Besse et al. (2014) found using M^3 data that the deposit at Birt E has a signature indicating a mixture of glass with a basaltic component. Since the deposit is located within a mare basalt unit, the source of its basaltic component may be the country rock or crystalline juvenile material from the same eruption(s) that produced the glassy material. Our estimate of ~90–93% juvenile material suggests the latter as the primary source of the signature.

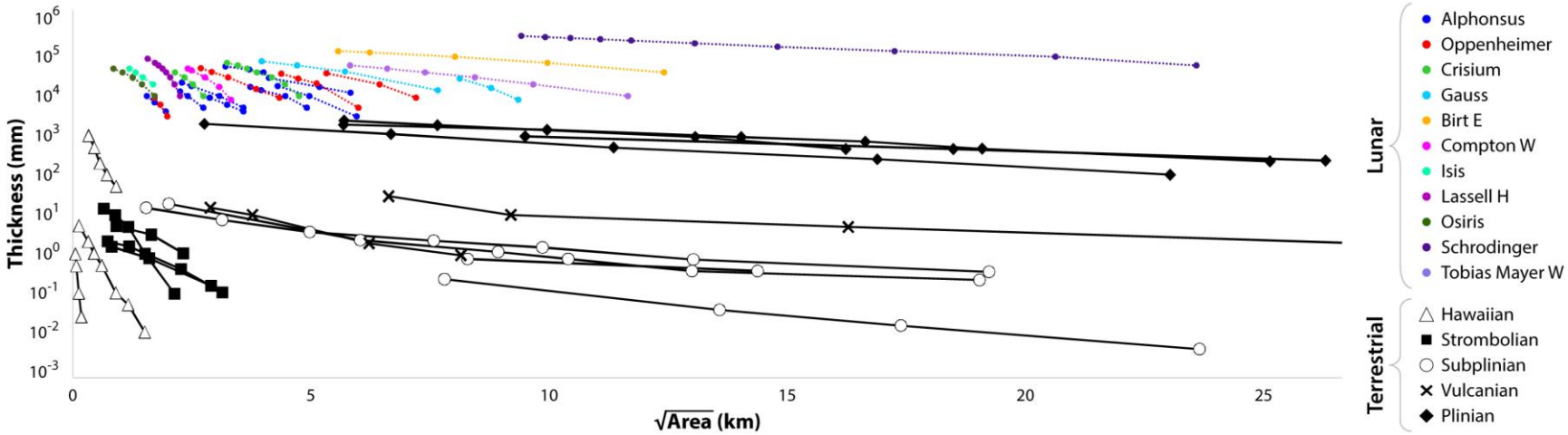

Figure 2.7. Thinning trends for deposits in this study alongside thinning profiles from terrestrial deposits of known eruption type (Bonadonna et al., 2002; Houghton et al., 2008, 2015; Taddeucci et al., 2015; Romero et al., 2017).

2.4.3 Eruption dynamics

It has long been thought that cones, localized dark mantle deposits, and regional dark mantle deposits represent separate eruption mechanisms and have thus been treated as separate classes of pyroclastic deposits with distinct eruption models (e.g., Head and Wilson, 1979, 2017). However, recent spectral studies of LPDs have uncovered a wider compositional diversity among deposits than previously postulated (e.g., Gaddis et al., 2000, 2003; Besse et al., 2014; Jawin et al., 2015; Bennett et al., 2016). The slow ascent rates associated with the simple lunar Vulcanian model would hinder the eruption of juvenile material, yet glass and clinopyroxene have been identified in small to moderate amounts at Alphonsus Crater (Jawin et al., 2015; Gaddis et al., 2016) and in moderate to large amounts at Oppenheimer Crater (Bennett et al., 2016). Figure 2.7 shows the thinning trends of the deposits in this study, where each point represents the square root of the area enclosed by the corresponding isopach (i.e., thickness contour), alongside terrestrial deposits produced by various eruptive mechanisms. This method of plotting profiles of pyroclastic deposits was first implemented by Walker (1973) and is most often used by terrestrial volcanologists to calculate deposit volumes by methodology described by Pyle (1989). However, the slope of the thinning profile has also been correlated with eruption type (e.g., Houghton et al., 2000, 2008, 2015; Bonadonna et al., 2009; Alfano et al., 2011). We generated the lunar data by plotting thickness contours using the difference DTM for each deposit and calculating the enclosed area for several thicknesses at different distances from the vent. The lunar profiles are consistently thicker than their terrestrial counterparts, suggesting that they may be polygenetic or that they underwent longer eruption durations than is typical for analogous eruption types on Earth. The slopes vary from steep (similar

to Strombolian-type on Earth) to very shallow (matching Plinian-type on Earth). Interestingly, deposits from the same sites appear to exhibit similar slopes to one another despite having different juvenile proportions, perhaps implying that eruptions occurring near one another share eruption rates and style, but not necessarily eruption durations and volumes.

Fundamental differences between eruptive environments of the Earth and the Moon, most importantly the presence of an atmosphere on Earth that allows for the formation of tall convective columns, make direct correlations of eruption styles between the two bodies problematic. We merely suggest that the broad range of profile slopes, along with the diversity of morphometric relationships with juvenile composition shown in Fig. 2.6 and the aforementioned observations of compositional diversity among LPDs in previous studies, cannot be explained by a single eruptive mechanism or a single eruption scale. Furthermore, our results show that deposits considered cones in the literature (Crisium 1 and 2, Isis, Osiris, and Lassell H) and deposits considered localized dark mantle deposits (all others) fall along a common morphological continuum, with no clear separation between the two groups. Therefore, we propose that the models for LDMDs and cones be treated as end-member scenarios, with the Alphonsus deposits representing lunar Vulcanian, cones representing Hawaiian or Strombolian, and most other deposits forming a middle ground, with Vulcanian-type depressurization followed by Hawaiian or pure-jet subplinian eruption of varying energies (as suggested by Bennett et al., 2016). Variations in size and juvenile content among LPDs may be due to differences in eruption durations and local variations in ascent rate due to differences in subsurface fracture widths, subsurface storage depths and pressures, and magma volatile contents.

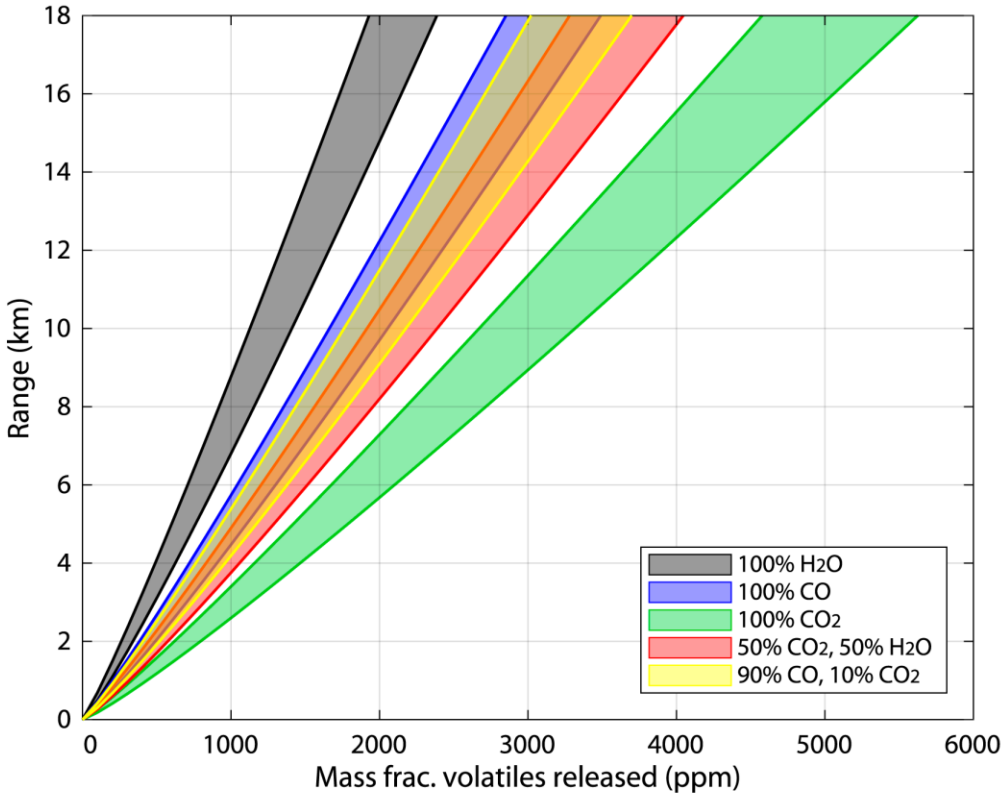

Figure 2.8. Ranges of ejected 0.03–0.3 mm pyroclasts for a 1500 K magma and multiple gas compositions calculated using equations from Wilson and Head (2017).

A model developed by Wilson and Head (2017) for lunar eruptions considers magma ascent, vesiculation, fragmentation, and ballistic emplacement of tephra in a vacuum. Figure 2.8 plots results of that model for a range of possible volatile contents responsible for producing the footprints of the deposits in this study, which have a maximum range of about 17 km. In these runs, we use a magma density of 2900 kg/m^3, a crustal density of 2550 kg/m^3, a temperature of 1500 K, a range of particle diameters of 0.3–3 mm, and a range of volatile contents as illustrated in Figure 2.8. Results suggest that the volatile contents may have been very high for the widest deposits, between ~2000 ppm and ~5000 ppm, depending on gas composition. This agrees with findings from Hauri et al. (2011), who measured up to 1410 ppm of water in olivine-hosted melt inclusions in

Apollo 17 glass beads. Given the lower solubility of CO_2 and CO in basalt compared to water, it is likely that those species had been exsolved prior to formation of the melt inclusions in the Hauri et al. (2011) study. It is therefore reasonable to surmise that the total fraction of volatiles dissolved in the magma at depth was greater by a nontrivial amount. Figure 2.8 also highlights the significance of gas composition in determining how explosive an eruption is. It is worth speculating as to what extent gas composition varied in lunar magmas, and what role any diversity in gas compositions may have had in producing the variety of volcanic landforms we observe today.

As a final note, we encourage the lunar community to develop new terms for lunar eruption types that are independent of terrestrial eruption types, as the application of terrestrial terms to lunar eruptions is often misleading, particularly for terrestrial workers accustomed to strict definitions for eruption types on Earth.

2.5. Summary and Conclusions

The results of our analysis of 23 localized pyroclastic deposits (LPDs) can be summarized by the following:

1. LPDs have a much wider range of juvenile fractions than previously recognized. There is a broadly positive relationship between various morphometrics (most notably deposit thickness and deposit area) and juvenile content of LPDs, both in terms of juvenile proportion and total juvenile volume.
2. The range of our estimates for Alphonsus generally agree with those from Head and Wilson (1979), with juvenile contents ranging from 0 to 60%. However, other deposits previously hypothesized to contain similarly low juvenile proportions to the Alphonsus deposits in fact contain as much as 97% juvenile material. Only

Tobias Mayer W and two Oppenheimer deposits contain juvenile proportions in the same range as our estimates for the Alphonsus deposits; all others contain more than 60%. The juvenile volume of many of these deposits is also quite high. Most fall in the range of 0.05–1 km^3 dense-rock-equivalent volume, but the largest, Schrödinger, contains over 50 km^3, which is of particular interest for future in-situ resource extraction applications (e.g., Hawke et al., 1990).

3. Observations combined with dynamic modeling suggest that the juvenile magma involved in many of these eruptions had significant dissolved volatile fractions. This finding, along with the large volumes of juvenile material also documented here, suggests that the total quantity of volatiles released from these eruptions is larger than previously thought, on the order of 10^9 kg in total.
4. LPDs bear a wide range of thinning relationships that would span multiple eruption styles on Earth. This suggests that a single formative mechanism hypothesis is not sufficient to explain the morphometry of all LPDs. Additionally, a variety of slopes are represented between the relatively flat Alphonsus deposits to the steeper cones such as Lassell H, instead of clustering into two distinct groups. The existence of a continuum between localized dark mantle deposits and cones in terms of morphometrics and juvenile proportion suggests that they represent a range of related eruptive behaviors between two extremes.
5. Comparison of lunar thinning profiles with terrestrial profiles reveals that the lunar deposits in this study are thicker than terrestrial deposits, suggesting that they are polygenetic or that they underwent longer eruption durations.

6. Previous studies of the glass and mineralogic estimates of LPDs have found greater quantities of juvenile material and overall compositional diversity among deposits than expected. These observations combined with our results show that LPDs represent a range of eruptive behaviors and thus call for more complex modeling of eruption mechanisms including style transitions, for example.

2.6. Acknowledgments

This work was supported by the NASA LRO project (grant number NNG07EK00C) and the NSF GRFP (grant number DGE-1311230). We extend our deepest thanks to Megan Henriksen, Madeleine Manheim, and the rest of the LROC SOCETSET team for making it possible to produce the high-quality DTMs used in this work. We would also like to thank the LROC team as a whole for efforts toward providing the data products used in this work and for scientific feedback during its progress.

CHAPTER 3

EPISODES OF FLUVIAL AND VOLCANIC ACTIVITY IN MANGALA VALLES, MARS

This chapter is reproduced from Icarus, where it was published in January 2015, with permission from the following co-authors: C. W. Hamilton, A. S. McEwen, and I. J Daubar.

3.1 Introduction

The origin and relationships between major Amazonian-age fluvial outflow systems on Mars is a subject of ongoing debate. In particular, there are challenges associated with generating the substantial volumes of water required to erode and transport material out of these systems, which has prompted a wide range of alternative formation hypotheses including aqueous flooding (e.g., Baker and Milton, 1974; Sharp and Malin, 1975), volcanism (e.g., Leverington, 2004), tectonism, glacial erosion (e.g., Lucchitta, 1982), aaeolian erosion (e.g., Cutts and Blasius, 1981), debris flows (e.g., Nummedal and Prior, 1981), or a combination of these processes (e.g., Chapman et al., 2003, 2010; Warner et al., 2009; McEwen et al., 2012). While lack of terrestrial analogs of comparable scale and complexity renders geomorphic comparison of large landscape features in these regions difficult (Mars Channel Working Group, 1983), new high-resolution images allow us to identify smaller surface features that provide clues about the processes that have influenced their overall surface geomorphology, allowing for reconstruction of their activity history. Moreover, relative placement of outflow processes within the martian

global chronology contributes to constraints on global climate models and an understanding of how the martian subsurface has changed in time. Mangala Valles serves as an ideal case study due to its relative isolation from the influence of additional outflow regions, rendering it the best-known example of a relatively closed outflow system on Mars.

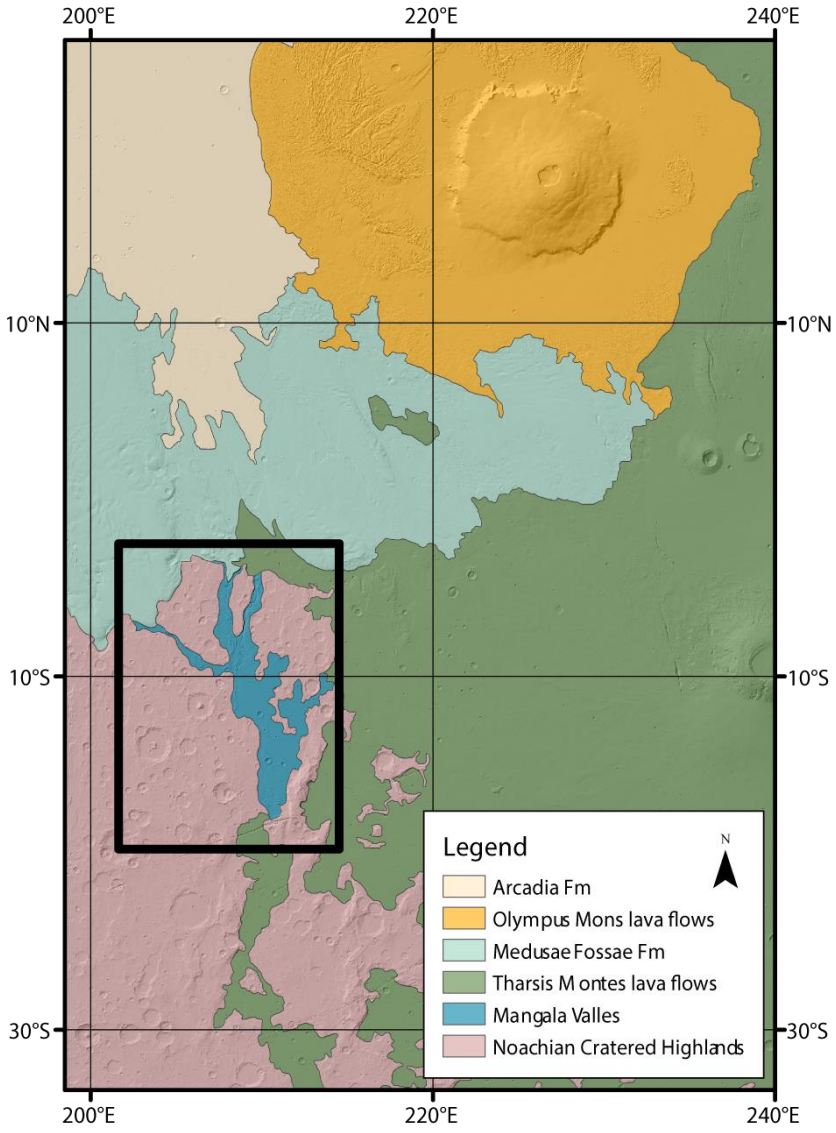

Figure 3.1. Regional context map showing MOLA shaded relief mosaic map overlain by a simplified geologic map based on global map from Skinner et al. (2006). Black inset denotes the study area. All maps use cylindrical projection.

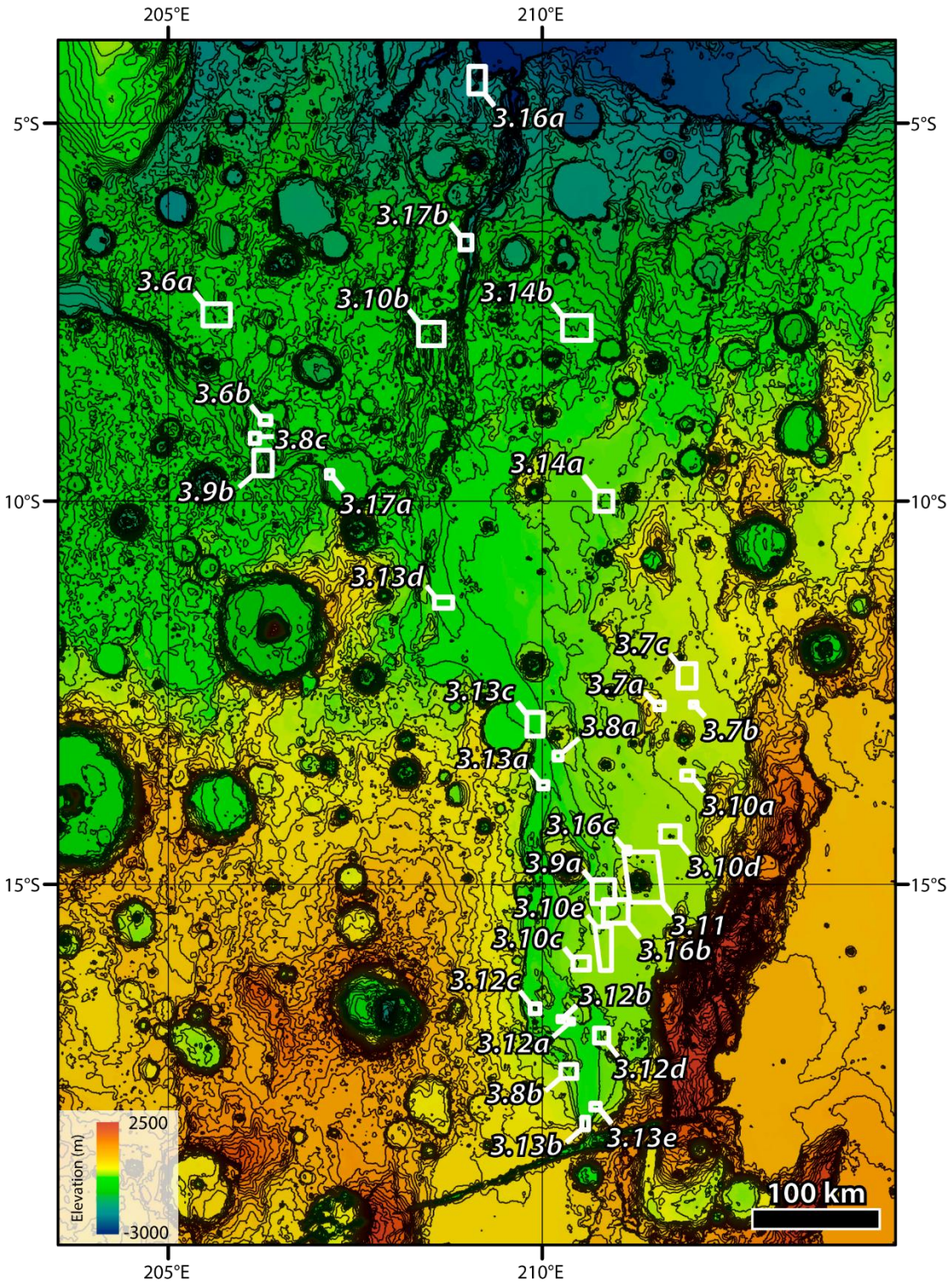

Figure 3.2. MOLA shaded relief/colorized elevation map of study area with white insets denoting figure reference locations. Contour interval 100 m.

Mangala Valles is a 900-km-long north–south trending system of channels and wide valleys southwest of the Tharsis rise, about 800 km south of the equator (Fig. 3.1). It heads at Mangala Fossa, a 200-km-long graben that is part of the Memnonia Fossae graben system. It is about 5–7 km wide at the mouth, and gradually opens to the north for about 300 km, where it then broadens and loses much of its topographic variation (Fig. 3.2). At its widest, Mangala Valles is about 200 km across, north of which it transitions into three narrow channels that drain into Amazonis Planitia. Near its source and in northwestern channel segments, the topographic relief between the channel floors and adjacent plateaus reaches up to 150 m, whereas the broad, middle portion of the system exhibits a rather smooth transition from a topographic low running along its western margin to a topographically high on the eastern side, which is dominated by a high plateau. Mangala Valles is located near the western boundary between the Tharsis volcanic plains and the cratered highlands and surrounded by heavily cratered Noachian Highlands, which includes a narrow mountain range on the eastern side of Mangala Valles that separates it from smooth plains of the Tharsis Montes Formation.

Mangala Valles has been mapped previously, but these maps focus on smaller areas (Chapman et al., 1989a,b,c, 1991; Tanaka and Chapman, 1990, 1993; Craddock and Greeley, 1994; Zimbelman et al., 1994; Basilevsky et al., 2008) and/or are less detailed (Tanaka and Chapman, 1990; Ghatan et al., 2005) due to use of lower-resolution images. The first objective of this study is to map the Mangala Valles using Mars Reconnaissance Orbiter (MRO) Context Camera (CTX) images (Malin et al., 2007) to achieve a level of detail comparable to Basilevsky et al. (2008), but over the outflow channel system in its entirety. CTX images provide a spatial resolution (~6 m/pixel) and coverage that was not

available to previous authors, who relied on High-Resolution Stereo Camera (HRSC) onboard Mars Express (Jauman et al., 2007), Mars Global Surveyor (MGS) Mars Orbiter Camera (MOC) (Malin et al., 2001), MGS Mars Orbiter Laser Altimeter (MOLA) (Smith et al., 2001), and Viking images (Carr et al., 1972). The resolution of CTX images allows for the detection of small, but key surface features that lead to an improved understanding of the stratigraphic relations of larger geologic units. Our second objective is to use the map along with crater counts and additional photogeologic observations of relative stratigraphy to determine the probable sequence of events that led to the present appearance of the system, and to draw comparisons to other martian outflow systems. This study does not include quantitative modeling of the source mechanism nor of erosive flooding events in Mangala Valles; for modeling approaches the reader is referred to Wilson and Head (2002), Thakur et al. (2007), Wilson et al. (2009), Bargery et al. (2011), and references therein.

3.2. Methods

The mapping area extends from roughly 3.5°S to 20°S and 214°E to 203°E, covering a region that is about 925 km in length by 625 km in width. Digital mapping was performed using an image mosaic base layer consisting of daytime infrared images acquired from the Mars Odyssey Thermal Emission Imaging System (THEMIS) instrument (Christensen et al., 2004), with a spatial resolution of 100 m/pixel (Edwards et al., 2011; Hill et al., 2014). Individual CTX images were used for detailed mapping and analysis due to their relatively high resolution (~6 m/pixel), near-ideal illumination conditions (~3 PM), and excellent coverage of the mapping area. Images from the MRO

High Resolution Imaging Science Experiment (HiRISE) (McEwen et al., 2007), which have a scale of 0.3 m/pixel, were also used, though to a lesser extent than CTX because they have very limited spatial coverage in this region. Gridded elevation data from the MOLA (Smith et al., 2001), used in the forms of contours, elevation cross sections, and colorized elevation maps, were crucial for identification of unit contacts and other detailed analyses. Similarly, Digital Terrain Models (DTMs) from the HRSC (Jauman et al., 2007) (~12.5 m/pixel) were useful in determining elevation differences for geologic mapping. All elevations discussed are based on gridded MOLA elevation values, and map coordinates use the IAU2000 reference system. Geologic maps from previous work (Chapman et al., 1989a,b,c, 1991; Tanaka and Chapman, 1990, 1993; Craddock and Greeley, 1994; Zimbelman et al., 1994; Basilevsky et al., 2008) were also used as mapping references. The map units in this study were defined using surface geomorphology alone. Therefore, the map presented is not an interpretive bedrock map, but rather a map of surface features observable in visible high-resolution images. Following correlation and geomorphic characterization, all major geologic units, as well as specific locales of interest, were dated using standard crater counting techniques (as described by Michael and Neukum, 2010). Rectangular areas of ~60–400 km^2 were outlined on CTX images and all craters larger than ~50 m in diameter were counted within the area. Since model age uncertainty increases with decreasing area counted, small features (e.g., streamlined islands) were not dated. The resulting size frequency distributions were plotted with $\sqrt{2}$ diameter binning and model ages were fitted using the chronology and production functions derived in Hartmann (2005) using the Craterstats2 program (Michael and Neukum, 2010). The number of crater diameter bins used to calculate crater retention ages was chosen on a case-by-case basis

based on where the minimum bin unaffected by rollover due to the CTX image resolution limit and the maximum bin unaffected by older resurfacing events occur on each plot. Due to the expectation that many of the surfaces counted underwent one or more resurfacing episodes, differential fits were used as they are more appropriate for fitting multiple resurfacing events (Michael, 2013), which are expressed when an older isochron can be identified in the larger crater bins. Note that crater counting uncertainties are a multivariable statistical description of how well the mean is known based on the number and distribution of samples in the individual crater count and should not be interpreted as the uncertainty of the absolute age determined by the crater count. Additionally, the ages calculated represent the time estimate of surface modification, not necessarily the time of bedrock emplacement.

3.3. Results

Figure 3.3 shows our map of the Mangala Valles region and includes 19 units. The detailed mapping is focused within the confines of the main valley walls with surrounding geologic units defined in accord with the current global geologic map for Mars (Tanaka et al., 2014). Note that all Noachian highland geologic units are shown as one encompassing unit, Nh. Since crater rim and ejecta materials within Nh are apparently not related to major resurfacing events in Mangala Valles, they have not been included on the maps. A detail of the southern portion of the mapping area is provided in Figure 3.4, and a detail of the mapped northwestern channels is provided in Figure 3.5.

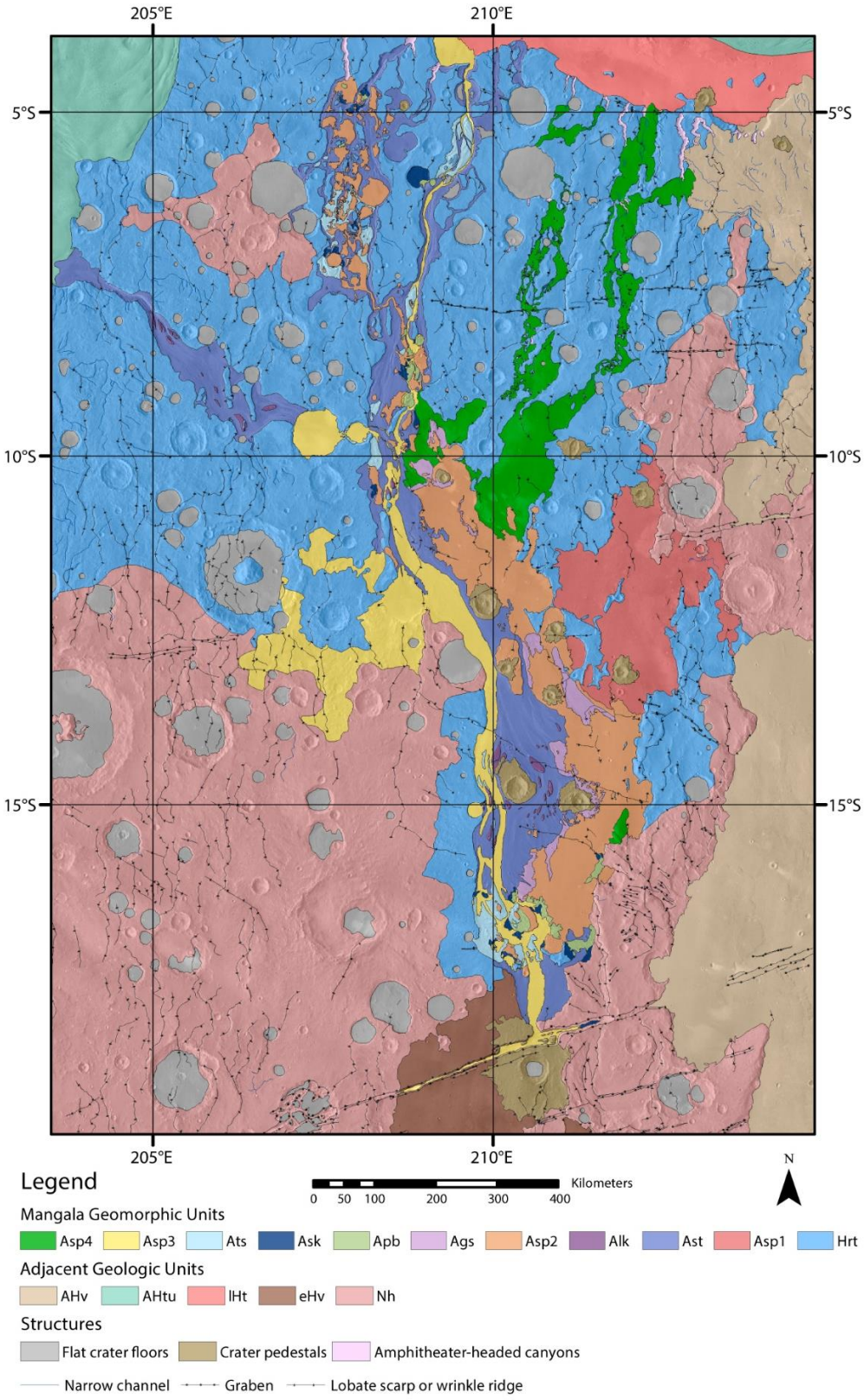

Figure 3.3. A complete geomorphic map of the study area with a THEMIS Day IR v11.6 mosaic base.

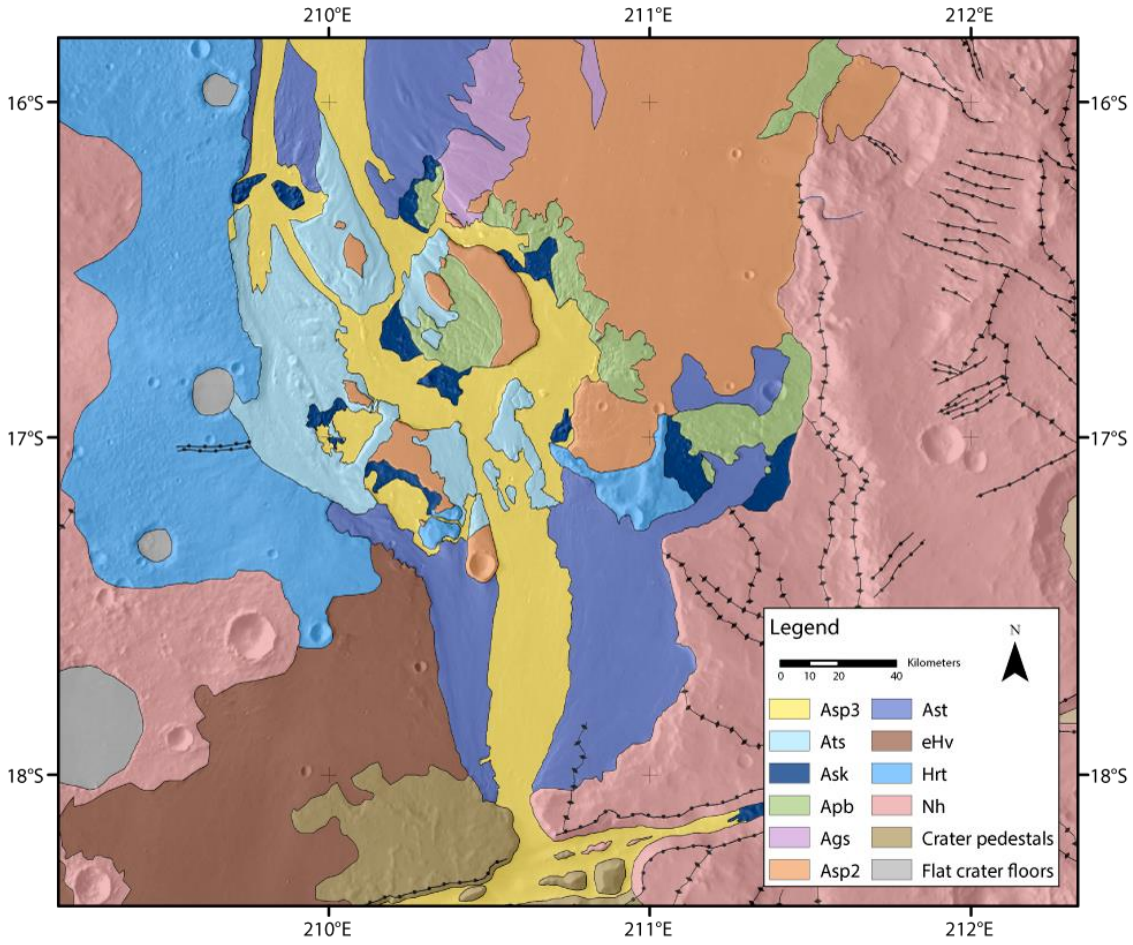

Figure 3.4. A detailed view of the southern portion of the map (THEMIS Day IR v11.6 mosaic base).

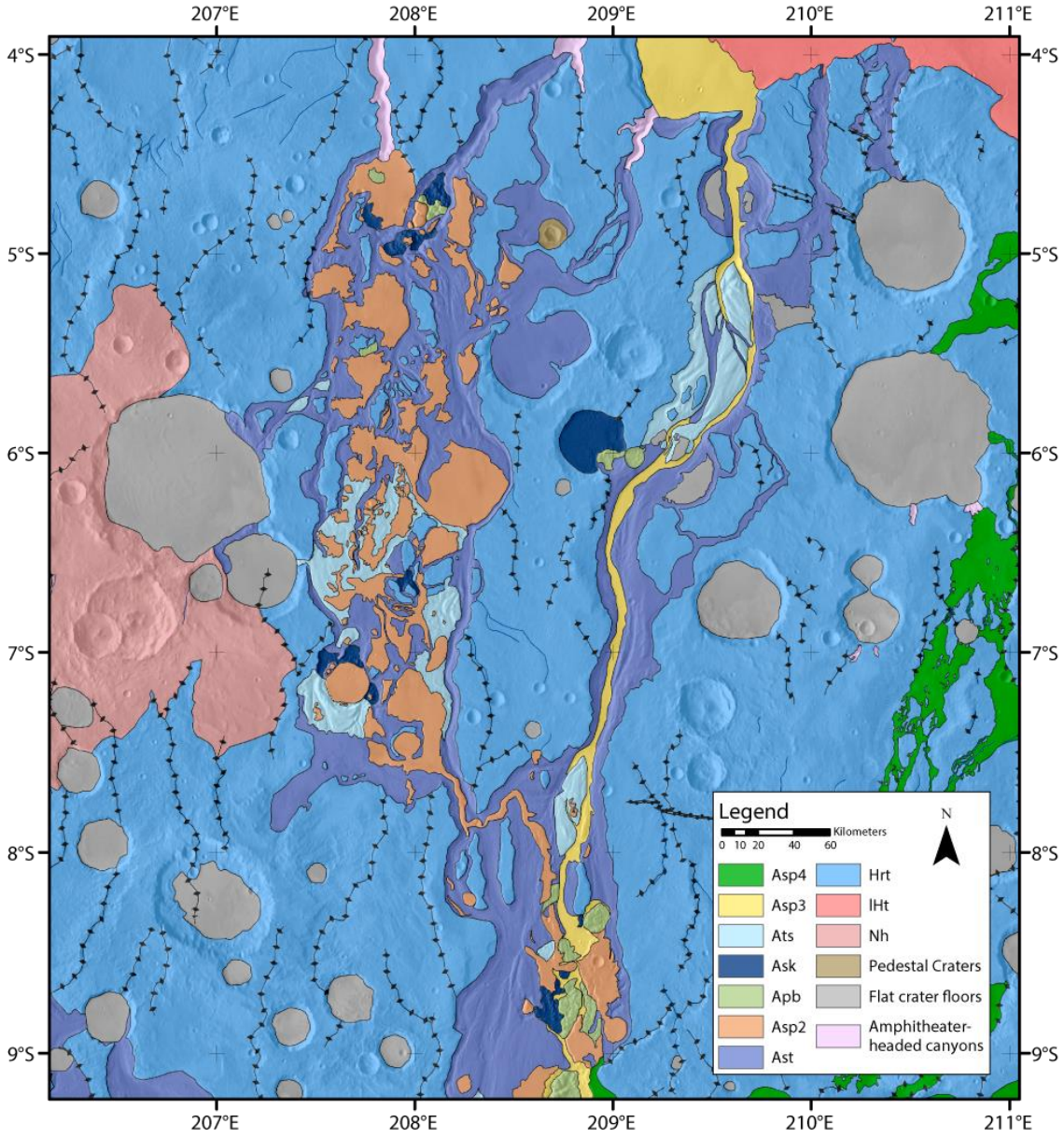

Figure 3.5. A detailed view of the mapped northwestern channels (THEMIS Day IR v11.6 mosaic base).

3.3.1 Mapped Geomorphologies

i. Rough terrain (Hrt)

This unit refers to regions with hummocky, high-relief surfaces that retain high crater densities, yet are distinguishable from unmodified highland terrain by evidence of partial resurfacing and relatively shallow slopes. It is present in much of the northern portion of the study area and in the high-elevation areas surrounding the main valley. Within the main valley and throughout the northern and northwestern channels, Hrt surfaces often manifest as small islands between or within larger geological units and tend to sit higher than the surroundings, with elevations approaching 500 m (Fig. 3.6).

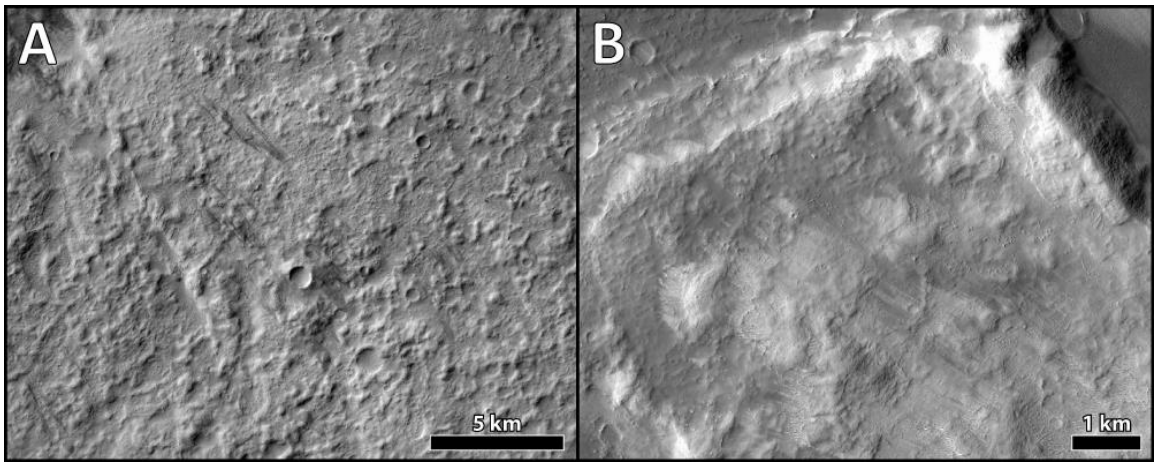

Figure 3.6. Typical rough terrain (Hrt) surfaces. Both images CTX. Illumination is from the left and north is up in all images.

ii. Smooth plain 1 (Asp1)

Asp1 is located in the northeastern portion of the main valley, representing a topographic high within the valley with elevations increasing from 100 m to 450 m toward the northeast. Asp1 is considered a smooth plain due to this relative lack of topographic variation, though it exhibits higher textural variation than the other smooth plains units. Lobes, sinuous channels, pits, hummocky plains, plates, and embayed and infilled impact

craters can be identified throughout its landscape (Fig. 3.7). Its western flank is completely bounded by Hrt, which also appear as embayed islands within Asp1. Similarly, the north and northeastern portions are bounded by highland terrain. To the south, Asp2 stratigraphically overlies Asp1. At its easternmost flank, Asp1 continues southward and is continuous with the topographically higher geologic unit AHv, which shares its geomorphology and crater densities (Fig. 3.15).

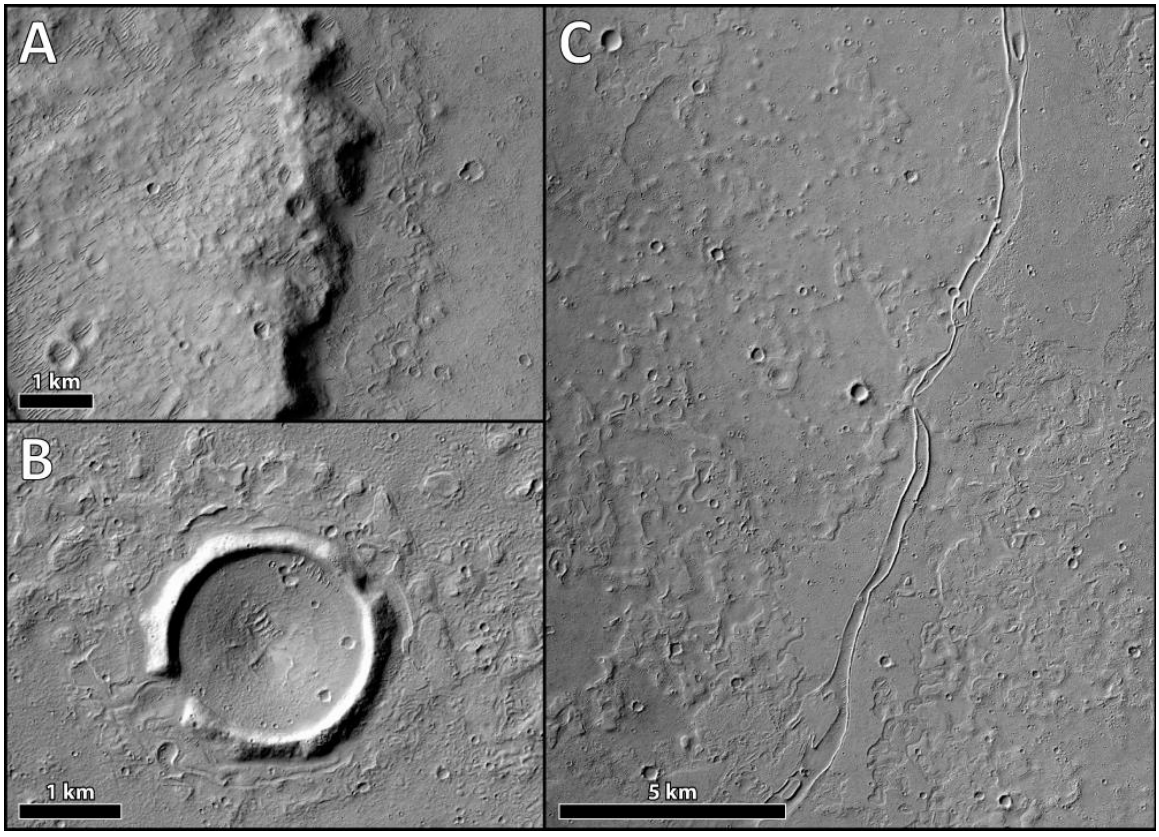

Figure 3.7. a) Hrt embayed by Asp1 on the right. b) An impact crater within Asp1 whose wall has been breached and floor filled. c) Sinuous channel feature in Asp1. CTX.

iii. Scoured terrain (Ast)

The scoured terrain morphology is one of the most prevalent units in Mangala Valles. Its southern reach begins at the valley mouth as two exposures flanking a central deposit of Asp3 to the west and east. However, the bulk of Ast begins about 100 km

northwest of the valley opening and continues northward along the western-central area of the main valley, with a general decrease in elevation from –50 m to –950 m. At the northwest of the main valley, it branches off into three distinctive channel sub-networks, reaching an elevation low of about –2800 m. The geomorphology of Ast is characterized by subparallel linear grooves between sharp ridges that often circumvent obstacles, cut through highland bedrock, and superpose other valley geomorphologies (Fig. 3.8b). Ast is largely composed of vast networks of anastomosing channels, and knobbed streamlined islands are scattered throughout its central body (Fig. 3.9). Benches and horizontal terraces are present on confining walls throughout the unit (Fig. 3.8a).

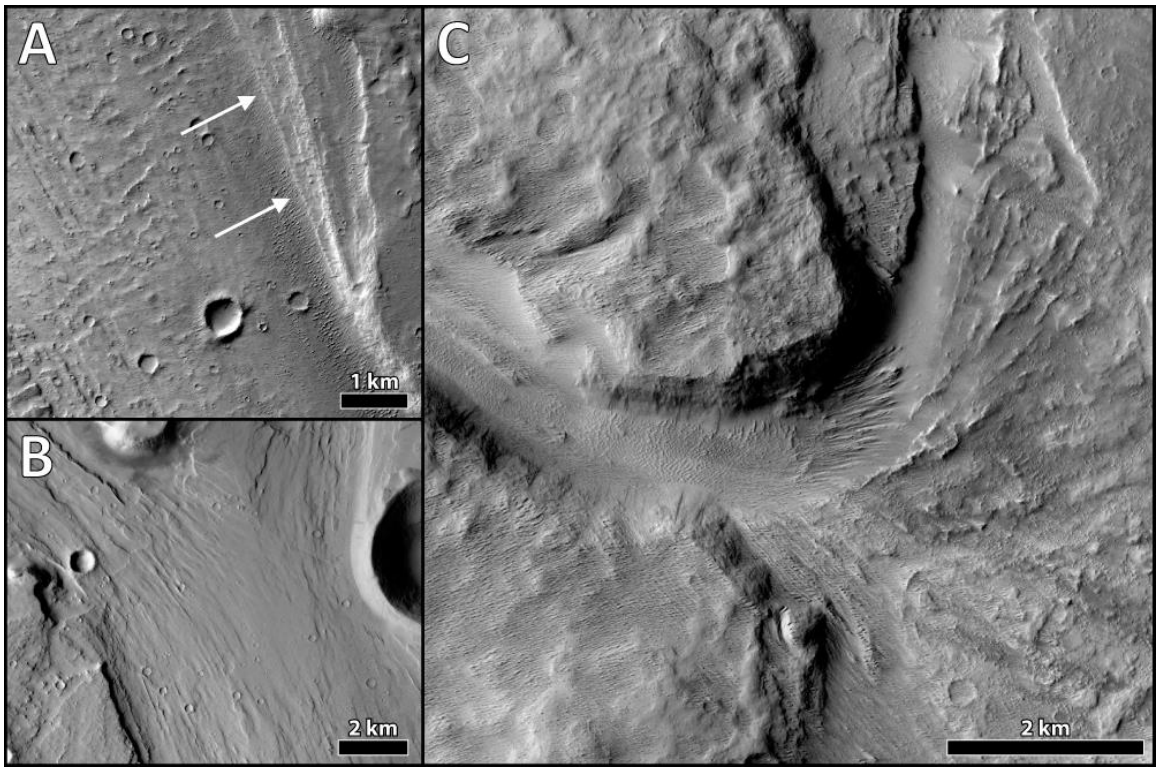

Figure 3.8. a) Typical Ast appearance with ridges and a channel terrace (indicated by black arrows). b) Diverging linear ridges in Ast. c) Hrt landscape dissected by Ast ridges. CTX.

iv. Large knobbed (Alk)

Alk refers to rounded or plateaued islands with teardrop-shaped bars that occur within the main central body and in the northwestern channel network of Ast (Fig. 3.9). Most plateaued knobs are between 150 and 300 m in height, while the more rounded knobs tend to be less than 150 m in height. The stepped/terraced topographic profile of these landforms suggests that these features more likely represent streamlined erosion of layered bedrock rather than depositional bars (Baker and Kochel, 1979; Milton, 1974; Greeley et al., 1977).

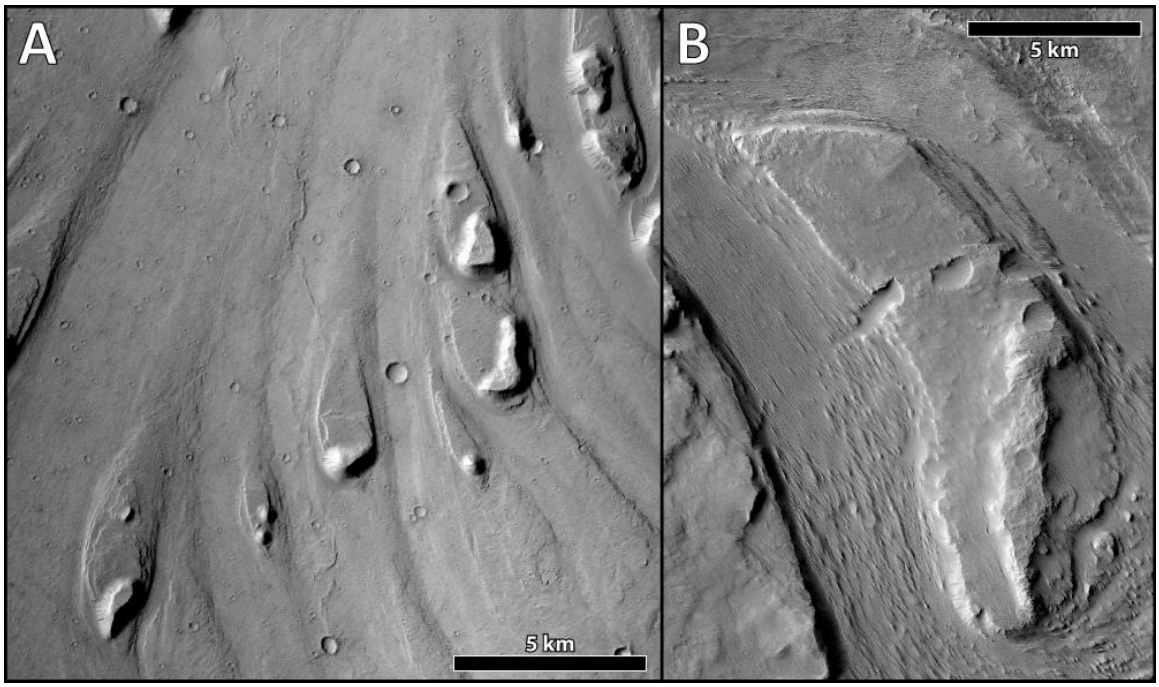

Figure 3.9. Streamlined islands of the Alk unit within Ast. Note the flat tops of these knobs. CTX.

v. Smooth plain 2 (Asp2)

Comprising the majority of the southeastern and middle portion of the valley, Asp2 is one of the largest and most distinctive units in the valles. Its southern portion is quite flat, with only 90 m of relief between 17°S to 13°S. North of this area, it begins to

dramatically decrease in elevation, reaching a low of about –200 m within the valley at 10°S. While the bulk of it is confined to the valley, it is scattered throughout the northwestern channels in disconnected islands of inverted topography (Fig. 3.10c), whose surfaces steadily decrease in elevation northward to a minimum of –1800 m at 4.5°S. It is smooth and flat, and tends to be platy on both small and large scales. It exhibits large crater embayment and infill features, some lobate margins (Fig. 3.10a), and streamlined features (Fig. 3.10d). There is less internal variation than is observed in Asp1, though there is a general increase in heterogeneity northward within the unit. Perhaps the most interesting characteristic of Asp2 is its broken-up appearance (Fig. 3.10c). Sections of it can be identified as residual islands at a distance from the bulk of the unit throughout the valley, but most notably in the southern valley region and in the northwestern channels. Many of these islands, as well as the edges of the main plateau, are heavily scoured with channels and gullies that are oriented in a general northwesterly direction.

vi. Grooved slope (Ags)

These features are transitional from Asp2 to Ast, mapped in multiple locations along the western and northern flanks and in the interior of Asp2. At the western margin of Asp2, these deep, subparallel grooves tend to originate with ridge orientations perpendicular to the orientation of the margin of Asp2—where trough heads break up the edges of the plateau and form complex multitudes of narrow canyons—then curve to the north until they are aligned with the ridges of Ast immediately to the west (Fig. 3.10b). Exposures that begin in the interior of Asp2 are northwest-trending. Beginning at about (211°S, 16°S) on the interior of the Asp2 plateau, a wide, shallow trough approximately 27

km in length and 3.5 km in width cuts into the bedrock and extends toward the edge of the plateau (Fig. 3.10e). Within the trough are scattered dissected, scoured pieces of residual Asp2 material. A similar feature can be found wrapped around a large mid-valley pedestal crater interfacing with the plateau (Fig. 3.11). This deeply incised canyon begins at the south of the crater and debouches at the north, where the ridge orientation rejoins Ast ridges. Again, scoured islands of Asp2 are distributed throughout the trough, and smaller troughs to the south and east of the unit open into the main canyon.

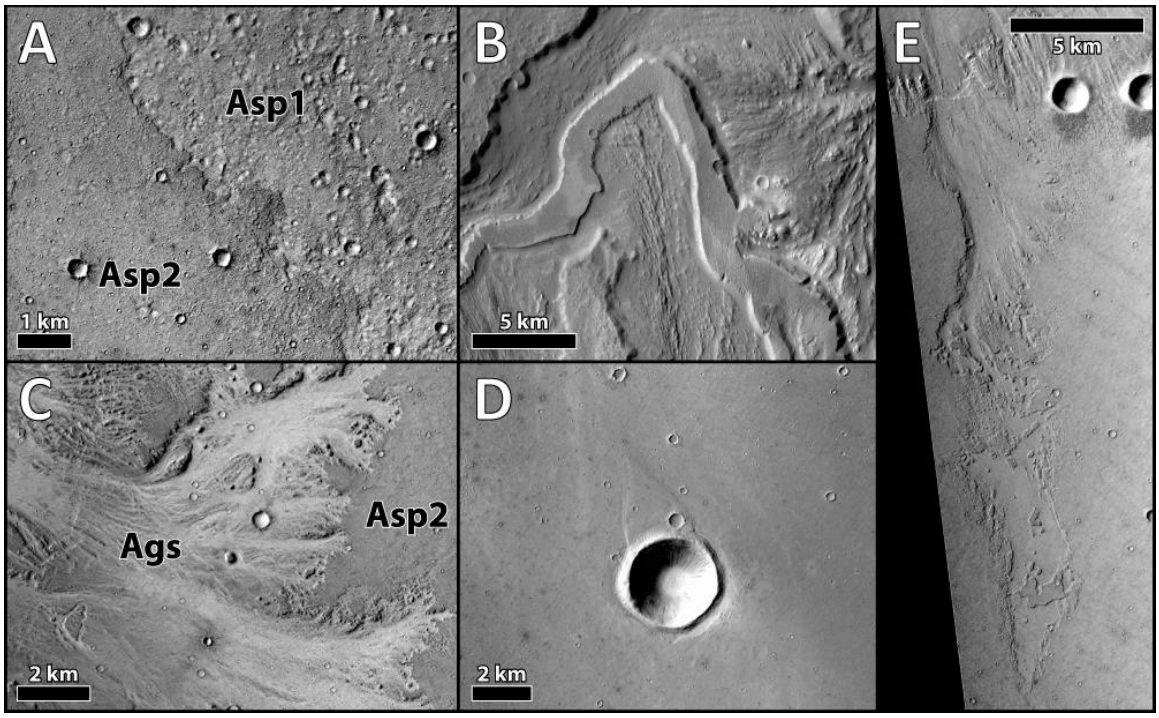

Figure 3.10. a) Uniform appearance of Asp2 and its lobate edges. b) Inverted Asp2 channel in northwestern Mangala channels. c) Grooved slope (Ags) features along the margin of ASp2. Note that Ags flow features tend to begin oriented perpendicular to the plateau edge. d) A streamlined crater and bar in Asp2. e) Wide trough in Asp2. CTX.

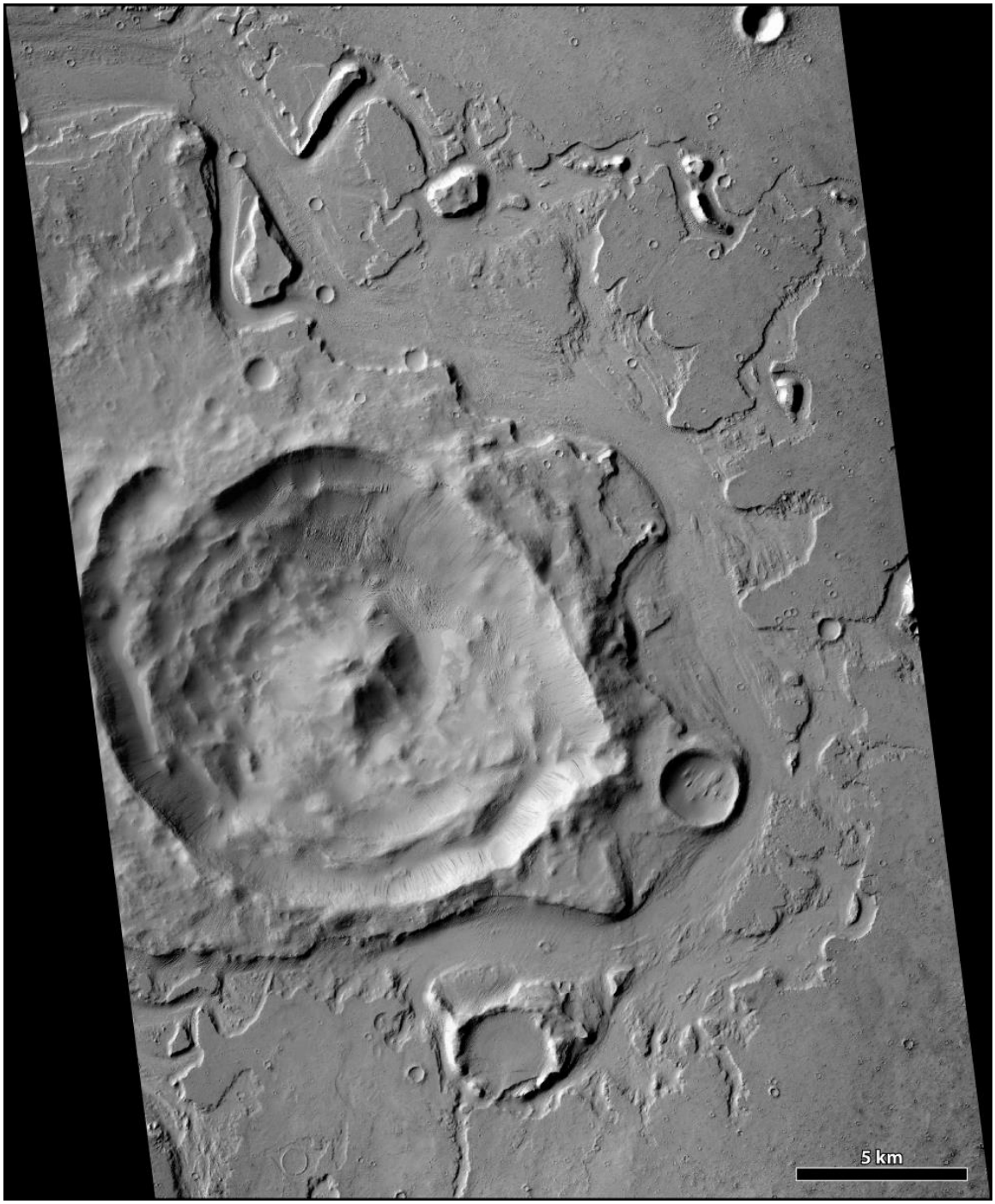

Figure 3.11. A large impact crater circumvented by a wide canyon. CTX.

vii. Polygonal blocked (Apb)

Apb terrain was mapped in the southern valley and in the northwestern channels, appearing as lower, subdivided smooth blocks with dissecting canyons near the edges of Asp2 and Ats (Fig. 3.12a). The polygons range in size from ~300 m to 3 km in width.

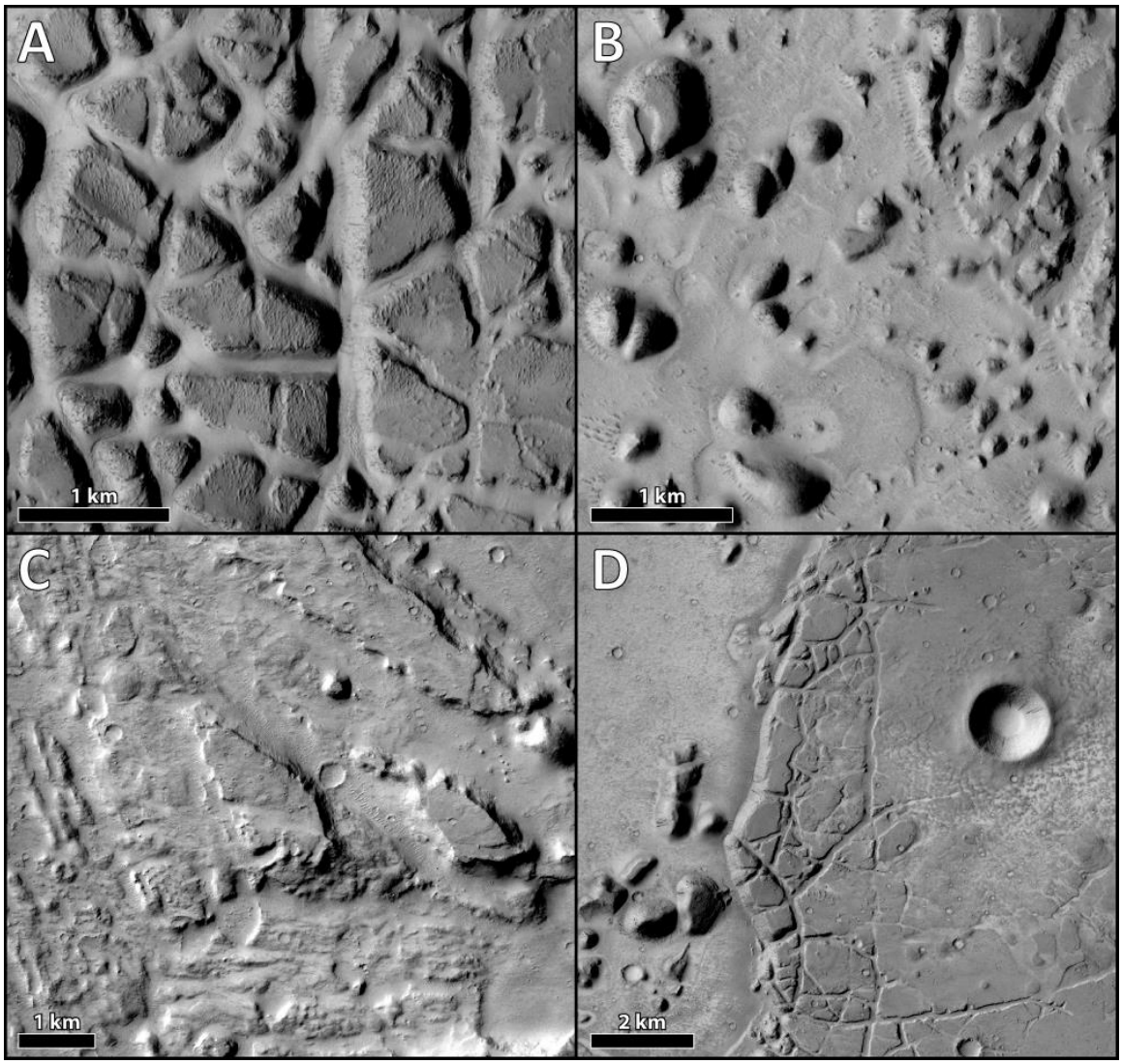

Figure 3.12. a) Polygons of the Apb unit. b) Embayed knobs of the Ask unit. c) Terraced scoured (Ats) unit. d) Blocky margin of Asp2, most likely a transitional phase from Asp2 to Apb. CTX.

viii. Small knobbed (Ask)

Ask features appear in the southern portion of the valley and in the northwestern channels in small batches adjacent to Apb, Ats, and Asp3. They are rounder, more widely

spaced, and generally more uniform in size than Apb, and range from 50–1500 m across. Ask is embayed by Asp3 in the southern valley (Fig. 3.12b).

ix. Terraced scoured (Ats)

The Ats unit occurs predominantly in the southern portion of Mangala Valles, as well as within elongate islands along the western edge of the valley within Asp3. It bears a general scoured or etched appearance, with deep linear grooves and steep walls (Fig. 3.12c), and is confined to isolated high islands and terraces often capped by a small piece of Asp2.

x. Smooth plain 3 (Asp3)

Asp3 begins at Mangala Fossa, covering the entire floor of the fossa as well as the valley opening, and follows the topographic gradient along the west valley wall, into the easternmost northwestern channel, and out onto the flat channel debouchment surface. It begins at about –140 m elevation, increases mid-valley to –90 m, and then gradually decreases in elevation toward the north, terminating at a low of –2800 m in the outlet area. Its floor is smooth with few craters, its edges are lobate in appearance, and it embays islands and large craters. Despite being relatively low in relief, there is significant heterogeneity within the unit. Lobes appear within the unit, sometimes in narrow, sinuous landforms (Fig. 3.13a), and small meandering channels appear at the valley mouth (Fig. 3.13b). One notable characteristic of this unit are shallow pits ~300–400 m in diameter with flat, soft rims that appear all throughout Asp3, but are most abundant in the middle and northern portion of the unit (Fig. 3.13c). These unusual features are most often circular, but many

appear elongated or coalesced. At the contact between Asp3 and the Ast unit, the ridges on the Ast unit often abruptly terminate where the outer lobe of Asp3 begins (Fig. 3.13a,e).

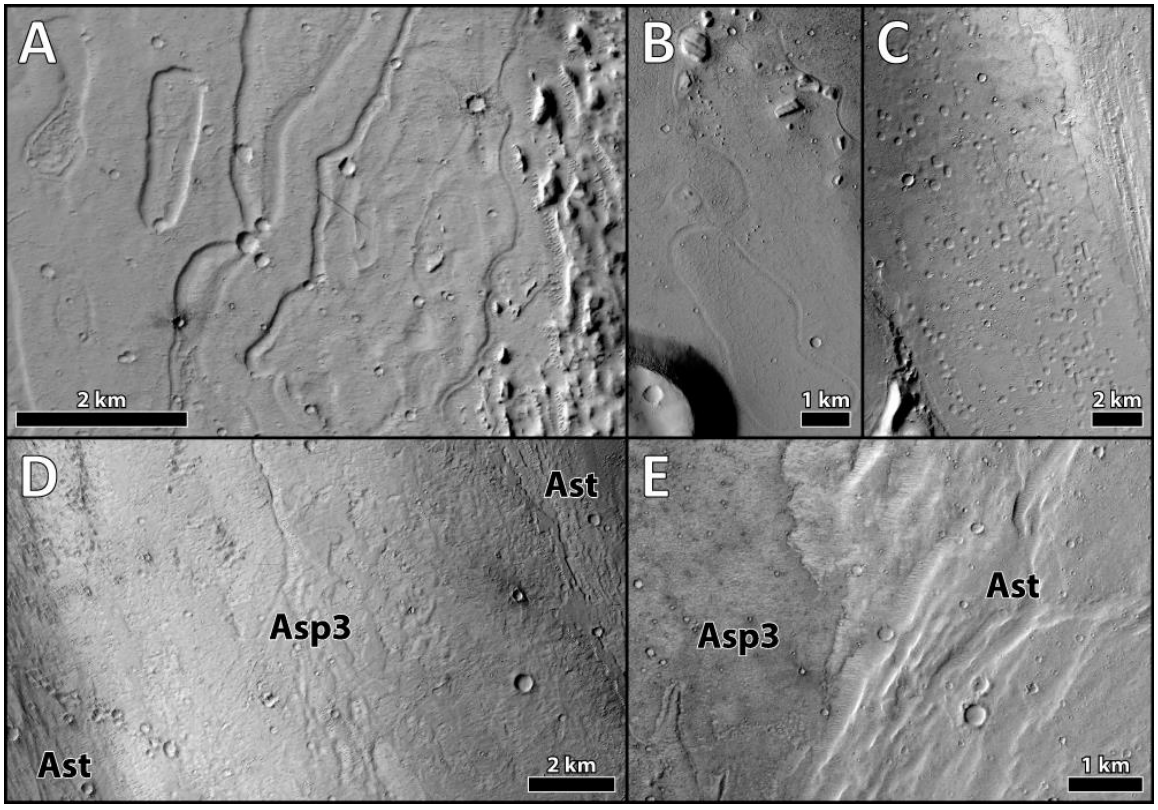

Figure 3.13. a) Sinuous channels in Asp3 along a contact with Ast (right). b) Meandering channels in Asp3 at the valley mouth. c) Unusual pits found in Asp3. d) A location where Asp3 has draped Ast, resulting in muted ridged topography. e) A lobate flow front in Asp3 truncating Ast ridges. CTX.

xii. Smooth plain 4 (Asp4)

Asp4 begins in the northern portion of the main valley where it divides into two branches that continue northward. It is extremely flat in its southern reach (elevation ranges from about –75 m to –100 m), with indistinct, flat interior lobes and muted craters (Fig. 3.14a). There is extensive aaeolian activity and a thick dust mantle, which appears to have buried most craters below ~500 m in diameter. The northern branches of Asp4 include additional muted features, including small, shallow islands (Fig. 3.14b); however, the mantle appears to be somewhat thinner in the western branch and thinnest in the eastern

branch. The elevation within these branches steadily decreases from about –100 m to –2300 m, where they transition to amphitheater-headed canyons that debouch onto the lHt unit.

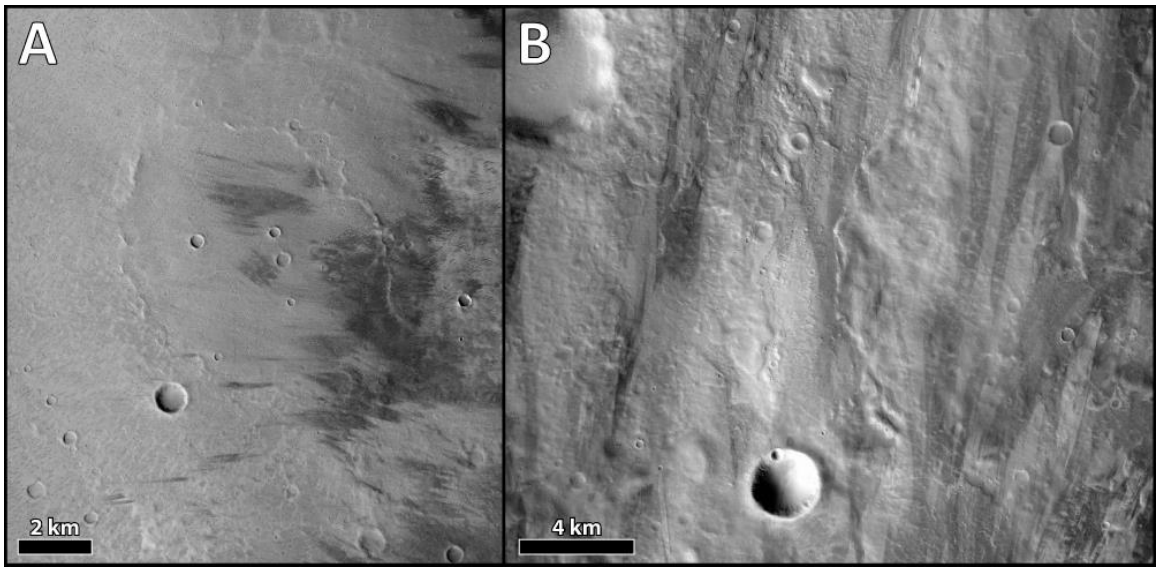

Figure 3.14. a) Large partially buried crater in Asp4. Note muted appearance of small crater rims. b) Asp4 landscape with muted streamlined landforms. CTX.

3.3.2 Crater Counts

Crater counts were performed in 30 locations throughout the area (Table 3.1) (see Supplementary Materials for map of areas counted and for individual size frequency distribution plots). Dating using crater counts introduces the question of what is being dated. A thin veneer of volcanic resurfacing will not erase larger craters from the underlying surface, so only the smaller diameter bins will reflect the younger age. Determining the age of a fluvially resurfaced area is also problematic in that, unlike volcanic resurfacing, the craters may be eroded rather than mantled. While it may be evident that crater erasure has occurred, many craters may appear only partially erased, making the distinction between craters erased by fluvial processes and younger aaeolian processes unclear. This ambiguity additionally complicates attempts to date surfaces that

have undergone multiple fluvial resurfacing events. The distinction between sudden resurfacing events such as a single destructive flood and ongoing long-term processes such as aaeolian erasure can also be difficult to distinguish in crater size frequency distributions. For these reasons, crater retention age is not as much of a measurement of absolute age of the rocks themselves as it is a measure of the crater survival age, the uncertainty of which is very difficult to quantify. Thus, interpretations must be supplemented with geologic observations (Hartmann, 2005; Michael, 2013).

According to the model ages derived from these crater counts, Hrt surfaces are the oldest (average 3680 ±25 Ma) in the valley, units Asp1 (average 878 ±66 Ma) and Ast (average 775 ±64 Ma) are intermediate in age, and Asp2 (average 434 ±37 Ma), Asp3 (average 346 ±41 Ma), and Asp4 (average 330 ±36 Ma) are the youngest. Small differences in model ages between sample areas with overlapping error bars within the same geomorphic unit (e.g., sample areas 11 and 12 within Asp2) likely represent variations due to statistical errors inherent in crater counting rather than real age variations. However, model ages within the same geomorphic unit exhibiting error bars that do not overlap, as is the case with sample areas 20 and 21 in unit Asp1, more likely represent separate events that resulted in similar geomorphologies. Of the units in which crater counts were performed, Asp4 was the most difficult to date where a thick dusty mantle covered small craters, resulting in a shallowly sloped crater size-frequency distribution (SFD) due to the strong sample bias toward larger craters. Thus, errors in the model ages for Asp4 may be larger than the formal uncertainties.

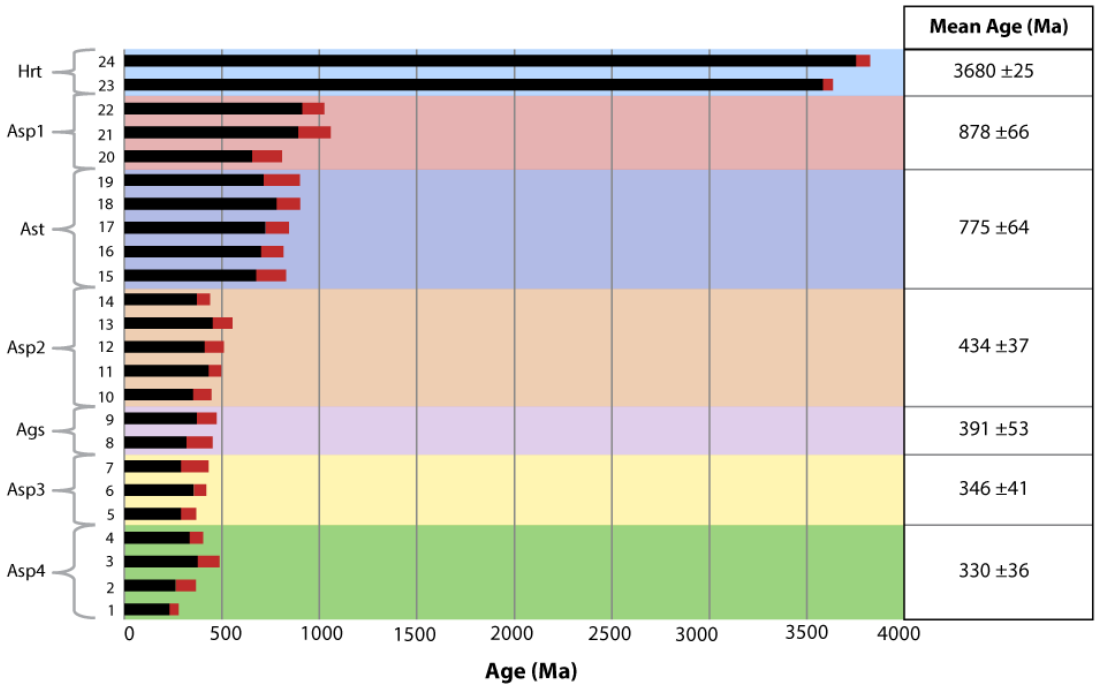

Figure 3.15. Bar plot showing model ages from crater counts arranged in order of decreasing average age with standard errors shown in red. The background colors correspond to the geomorphic map unit colors in Fig. 3.3.

Sample Area	Unit	Example Figure(s)	Area (km^2)	Crater Retention Age (Ma)	N	Minimum Diameter Bin (m)	Maximum Diameter Bin (m)
1	Asp4	3.14	300	243 ± 18	328	62.5	354
2	Asp4		300	302 ± 46	59	125	250
3	Asp4		500	419 ± 50	118	125	354
4	Asp4		300	357 ± 29	200	88.4	250
5	Asp3	3.13	90	316 ± 33	147	62.5	250
6	Asp3		200	375 ± 26	344	62.5	354
7	Asp3		100	348 ± 65	53	88.4	354
8	Ags	3.10c, 3.10e, 3.11, 3.19	200	372 ± 61	55	125	354
9	Ags		100	410 ± 44	141	62.5	250
10	Asp2	3.10a, 3.10d	100	387 ± 41	127	62.5	354
11	Asp2		500	452 ± 27	374	88.4	250
12	Asp2		100	448 ± 44	168	62.5	500
13	Asp2		70	491 ± 45	159	62.5	177
14	Asp2		400	393 ± 28	266	88.4	354
15	Ast	3.8	100	739 ± 71	153	88.4	500
16	Ast		200	746 ± 52	313	88.4	250
17	Ast		200	770 ± 54	317	88.4	250
18	Ast		100	828 ± 54	398	62.5	354
19	Ast		100	794 ± 87	143	88.4	354
20	Asp1	3.7	100	719 ± 70	161	88.4	500
21	Asp1		200	961 ± 75	289	88.4	250
22	Asp1		300	955 ± 51	552	88.4	500
23	Hrt	3.6	200	3590 ± 20	264	177	707
24	Hrt		100	3770 ± 30	68	250	1000
25	AHv	n/a	600	363 ± 25	374	88.4	707
26	AHv		300	386 ± 21	553	62.5	354
27	AHv		200	1160 ± 130	123	125	500
28	AHv		200	1370 ± 80	201	125	500
29	lHt	n/a	200	873 ± 160	44	177	500
30	eHv	n/a	200	517 ± 45	201	88.4	250

Table 3.1. Summary table of the results of 30 crater counts performed within the study area. Errors presented are the standard error of fit. See Supplementary materials for map of area locations and individual size frequency distribution plots.

3.4. Discussion

Large-scale channel landforms in major outflow regions on Mars such as Kasei, Ares, Tiu, Simund, Maja, and Mangala Valles have been compared to the channeled scablands of the Pacific Northwest, leading to general acceptance that these valleys were carved by water during megaflooding events (e.g., McCauley et al., 1972; Baker and Milton, 1974; Sharp and Malin, 1975; Komar, 1979; Burr et al., 2009; Carr and Head, 2010). However, identification of volcanic deposits on the channel floors in some of these regions have led to an alternative hypothesis suggesting that large martian outflow regions such as Mangala Valles were instead carved by vast volumes of lava (Leverington, 2007). Alternate hypotheses for Mangala Valles include the exposure of previously buried volcanic material by flooding (Zimbelman et al., 1992; Ghatan et al., 2005), fluvial activity followed by glacial activity (Head et al., 2004), volcanic deposition following megaflooding events (e.g., McEwen et al., 2012), and intermittent volcanism between flooding events (e.g., Chapman and Tanaka, 1990, 1993; Tanaka and Chapman, 1990).

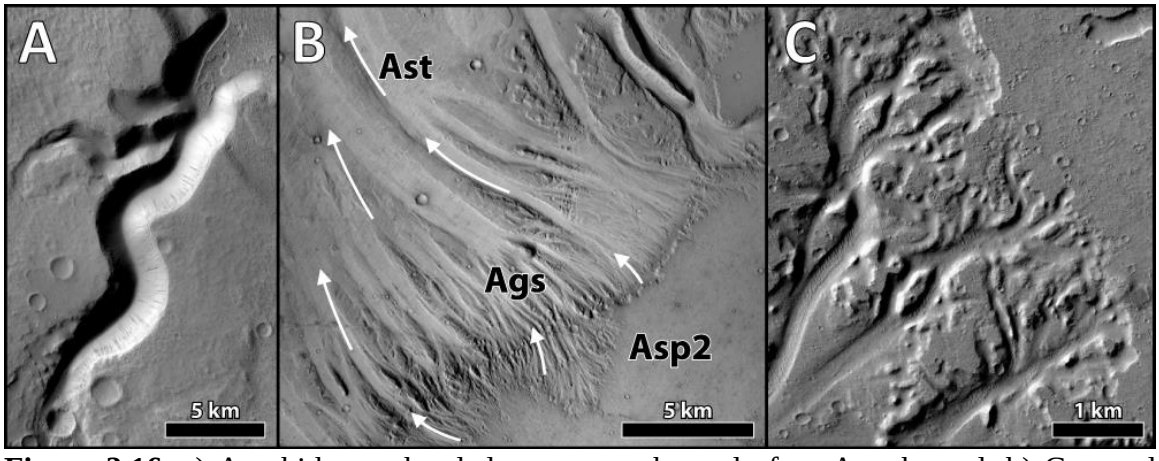

Figure 3.16. a) Amphitheater-headed canyon at the end of an Ast channel. b) Grooved slope (Ags) off of a local Asp2 plateau margin, grading into Ast to the northwest. White arrows indicate interpreted flow direction. A fault can be seen beginning from the bottom right and cutting through Asp2 bedrock toward the northwest. c) Amphitheater-headed canyons cutting into the margin of Asp2. CTX.

3.4.1 Evidence of fluvial activity

In Mangala Valles, we have observed numerous landforms characteristic of fluid flow including streamlined features (Fig. 3.8a, 3.9, 3.10c, 3.11), ridged topography aligned parallel to confining unit walls (Fig. 3.8, 3.9b), downcutting of steep slopes (Fig. 3.8b, 3.19), networks of braided channels, pendent bars (Fig. 3.9), cutbank walls (Fig. 3.8c, 3.9b), cataracts (Fig. 3.8a, 3.10e, 3.11), channel terraces (Fig. 3.8a, 3.8c), and amphitheater-headed canyons (Fig. 3.16a). Pre-fluvial impact craters on fluvial surfaces are observed to have an eroded, rather than covered or filled appearance, with lower, subdued rims. The resemblance of deep longitudinal striae within the Ast unit to Channeled Scabland grooves is suggestive of bedrock erosion by longitudinal roller vortices in powerful floodwaters (McCauley et al., 1972; Baker, 1973; Sharp and Malin, 1975). We consider the features of Ats to be the result of fluvial erosion, and are likely channel terraces and partially eroded topographic highs derived from the same event or events as scoured terrain, since these landforms often grade smoothly down into another fluvial unit of matching flow ridge orientation. Similar arguments apply for Ags features. While there is evidence that turbulent lava flows are locally capable of producing landforms traditionally associated with fluvial activity (e.g., Baker et al., 1992), a well-accepted example of a large lava-carved feature on Mars has yet to be conclusively identified, making a fluvial interpretation more favorable. However, large lava-carved channels have been identified on Mercury (Byrne et al., 2013).

3.4.2 Evidence of volcanic activity

Within the smooth plains units, we have observed features typical of volcanic landforms such as lobate-margined flow fronts (Fig. 3.10a, 3.13a, 3.13e), ridged flows (Fig. 3.17a), collapse pits (Fig. 3.17b), and embayed landforms (Fig. 3.7a, 3.7b, 3.12b, 3.13a, 3.13b). Compared to Ast, smooth plains units have relatively few flow features, the exceptions being sinuous channels and aggradational streamlined features similar to those observed in Kasei Valles (Chapman et al., 2010) (Fig. 3.10d). Older craters with high rims tend to be embayed by what we interpret to be lava flows, whereas smaller craters have a characteristic infilled appearance. This would occur when the thickness of the lava flow exceeds the height of the crater rim and/or breaches it. An infilled appearance can also result if a portion of the crater rim wall is collapsed, allowing for flooding of the crater floor with lava (Fig. 3.7b). Post-lava-emplacement impact craters tend to be accompanied by blocky ejecta, indicative of mechanically resistant bedrock (Basilevsky et al., 2008). The shallow pits observed as part of the Asp3 unit were previously interpreted as thermokarst pits that formed when subsurface ice was exposed and subsequently sublimated during volatile flooding (Chapman and Tanaka, 1993; Levy and Head, 2005). However, we suggest the alternative hypothesis that they are lava-rise pits (Walker, 1991) that formed when lava encountered obstacles on the underlying surface, forcing the lava to inflate around them and resulting in shallow, oblong pits. Morphological features such as these pits and smooth ridges within the unit are interpreted to be the result of lava draping ridged topography, most evident in exposures of older ridges of Ast adjacent to muted ridged landforms within Asp3 of matching size and orientation (Fig. 3.13d). The expression of underlying topography suggests a relatively thin and fluid, probably basaltic, lava flow.

The geomorphology of Asp1, on the other hand, is more pronounced than that of Asp3, having the hummocky, inflated, rafted appearance of similar to terrestrial inflated pahoehoe basalt surface morphology (see Keszthelyi et al., 2000, 2004).

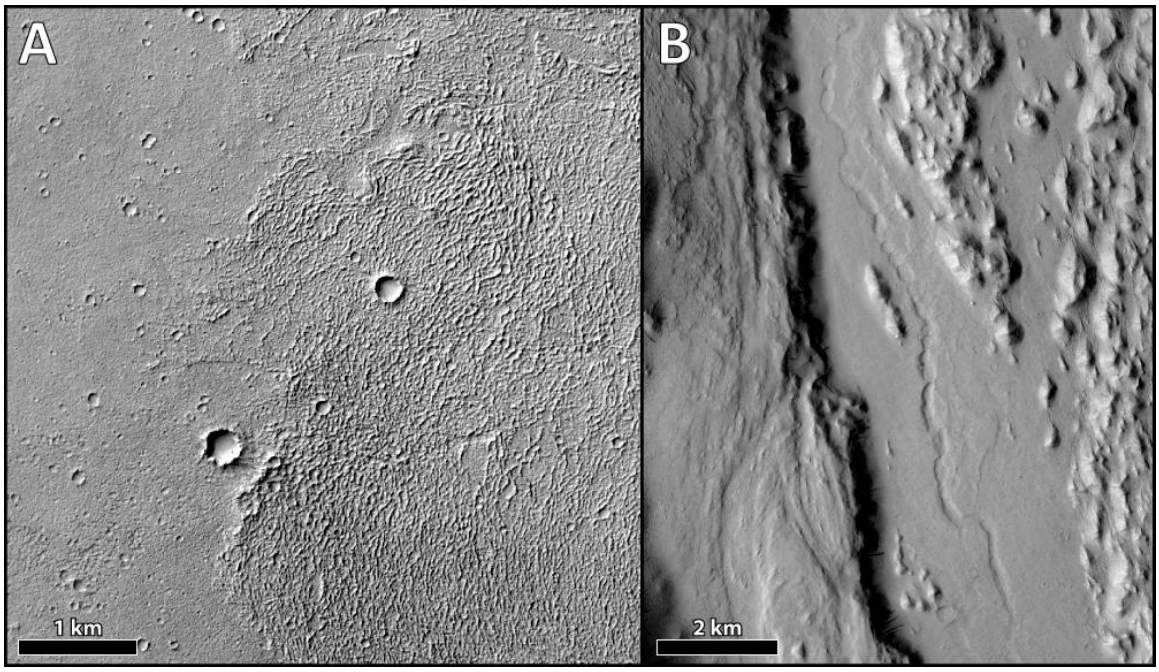

Figure 3.17. a) Ridged flow front in Asp3. b) Lavas tube collapse pits in Asp3. CTX.

Asp2 is characterized by sheet-like, homogeneous surfaces devoid of inflation features or expression of any underlying topographic features, resembling more closely lunar mare lavas or Archean high-Mg basalts on Earth, which are believed to be assemblages of fluid lava flows (Head, 1976). Asp4 is similarly homogeneous. Though much of its surface is coated in a fine mantle that obscures most of its features, it has an erosional pattern suggesting poorly consolidated material. Two candidate hypotheses arise for these observations: (1) it is a locally derived tephra deposit whose relatively soft bedrock is easily eroded and reworked, allowing for development of a large a dune field at the surface, or (2) it is a more distally sourced, unconsolidated tephra deposit that has been transported from the Upper Member Medusae Fossae Formation to the north.

The aforementioned shallow pits observed as part of the Asp3 unit were previously interpreted as thermokarst pits that formed when subsurface ice was exposed and subsequently sublimated during volatile flooding (Chapman and Tanaka, 1993; Levy and Head, 2005). However, we suggest the alternative hypothesis that they are lava-rise pits (Walker, 1991) that formed when lava encountered obstacles on the underlying surface, forcing the lava to inflate around them and resulting in shallow, oblong pits.

3.4.3 Evidence of post-emplacement fluvial modification of volcanic units

While most of the smooth plains units show evidence of only aaeolian and impact modification, there are numerous features within Asp2 suggesting that it has undergone fluvial modification. Many of the crater rims have been eroded and flattened (Fig. 3.11), islands of Hrt and large craters within the unit are outlined in deep trenches (Fig. 3.11), large outcrops of inverted topography are present on its surface and along its flanks surrounded by Ast floor morphologies (Fig. 3.10b), and intact buttes whose heights correlate with that of the Asp2 plateau edge are scattered throughout the valley. Wide, shallow trenches marked by the Ags geomorphology with knickpoints occurring near the center of the plateau as well as on its flanks, and subtle, superficial streaks throughout the Asp2 unit seem to suggest overland flow and powerful bedrock abrasion (Fig. 3.16). Furthermore, the geometry of small amphitheater-headed canyons along its margin (Fig. 3.16c) is analogous to the terrestrial canyons carved in basaltic bedrock by megaflood overland flow (Lamb et al., 2008). These features exist at a smaller scale in Asp4 as well, which hosts amphitheater-headed canyons and streamlined islands (Fig. 3.14b) underneath its mantle.

Most notably in the northwestern channels and the southern valley region, remnant buttes and islands of Asp2 tend to be proximal to Ats, Apb, and Ask units. The Ats unit primarily occurs around islands of Asp2 material and is interpreted to be the result of partial erosion of segments of Asp2. Apb morphologies, which tend to occur at the edges of Asp2, often dividing the interface between Asp2 and Ask, may also represent partially eroded Asp2 material, and Ask more extensively eroded Asp2 material. This hypothesis is supported where transitional phases between Asp2, Apb, and Ask are visible (Fig. 3.12d). The mechanism for differing Ats and Apb morphologies is unclear, but we speculate that it is related to bedrock heterogeneities.

Unit	Bedrock	Modification	Interpretation
Hrt	Nh	Fluvial overland flow erosion, aeolian erosion	Fluvial and aeolian resurfacing of high-standing bedrock
Asp1	AHv	None	Flood basalt. Fill from AHv to the east
Ast	Nh	Fluvial erosion	Fluvial erosion of Nh
Alk	Asp2/Nh	Fluvial erosion	Streamlined islands
Asp2	Asp2	Fluvial overland flow erosion	Volcanic plateau with post-emplacement flooding
Ags	Asp2	Fluvial erosion	Fluvial erosion of Asp2
Apb	Asp2	Fluvial erosion	Fluvial erosion of Asp2
Ask	Asp2	Fluvial erosion	Fluvial erosion of Asp2
Ats	Asp2	Fluvial erosion	Fluvial channel terraces
Asp3	Asp3	None	Young lava flow
Asp4	Asp2	Aeolian deposition	Tephra/dust cover overlying lava flow(s)

Table 3.2. Summary table of interpretations of discussed geomorphologies. Note that evidence of aeolian activity is present on all surfaces, and is therefore not listed unless extensive.

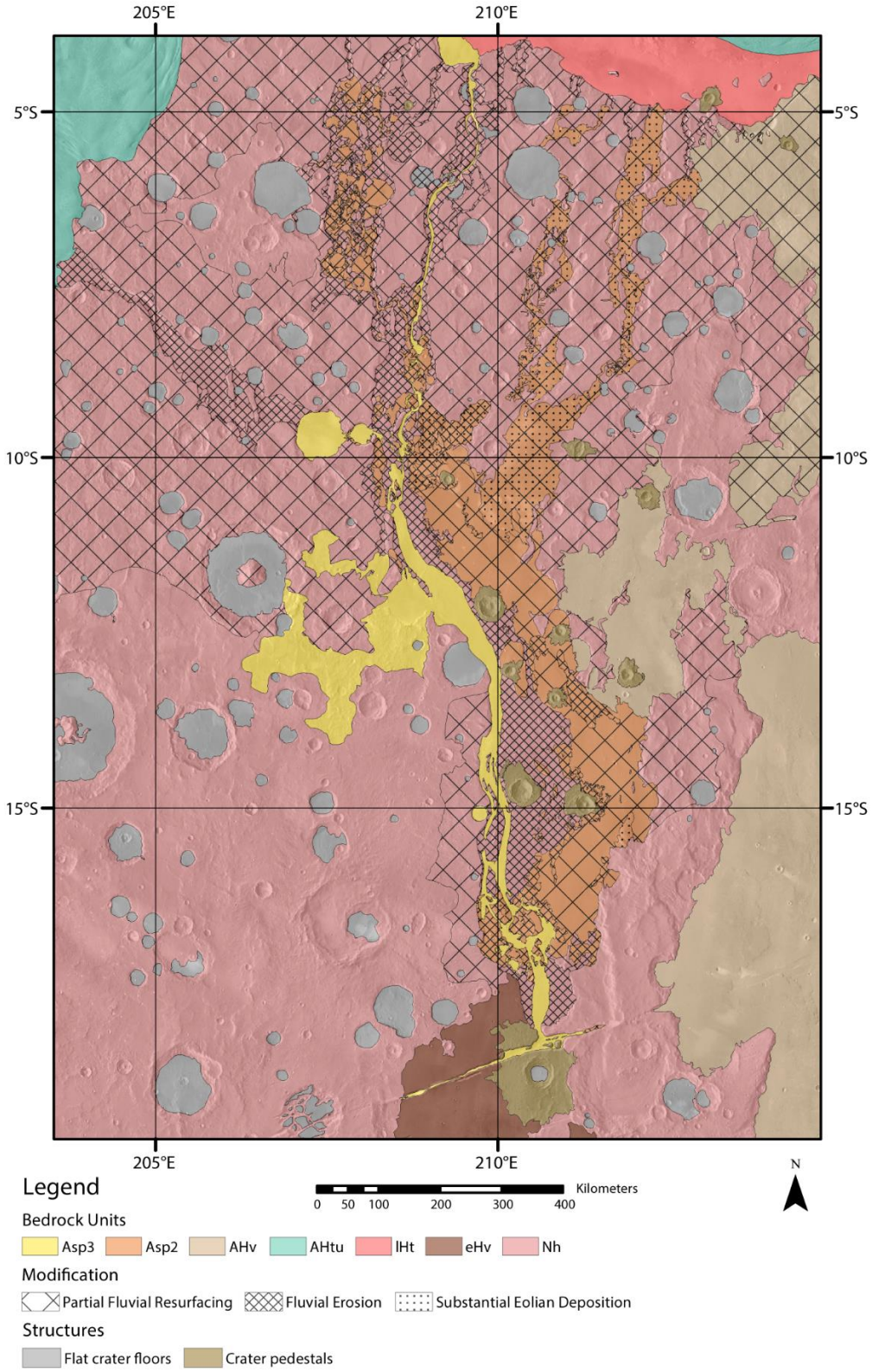

Figure 3.18. Interpretive geologic map showing hypothesized current extent of bedrock units and the distribution of fluvial modification and substantial aeolian deposition (THEMIS Day IR v11.6 mosaic base).

3.4.4 Geological history

The overall geologic interpretation of these units is largely dependent on their relative ages and placement. Aside from Hrt and Asp1, the oldest ages are attributed to Ast, though high numerical errors and a significant spread of individual ages support a multi-event flooding hypothesis, assuming these floods did not resurface the entire area uniformly. Moreover, we cannot rule out possible fluvial events during the ~1–3 Ga period because the crater retention ages of these surfaces have been reset by younger lava deposits or fluvial activity. While this information alone is not necessarily significant, when combined with observations of the fluvial modification of volcanic units, a basic timeline involving periods of flooding alternating with periods of volcanism can be inferred.

Aside from Hrt, crater counts designate Asp1 as having the oldest valley surfaces (~700–950 Ma), the ages of which overlap with some of the oldest Ast ages, making it unclear whether any or all of the originating volcanic events depositing Asp1 material predate or postdate fluvial activity. Since it stratigraphically underlies Asp2, its southern subsurface extent is unknown. Asp3 is the youngest volcanic flow unit, as evidenced by its stratigraphic position above all other valley geologic units besides Asp4 and its relatively young crater retention ages (300–400 Ma). Interestingly, Asp3 age estimates overlap with those of Asp2, though Asp2 ages may be underestimated since there may have been partial resurfacing due to post-depositional fluvial activity. Asp4 has the youngest average crater retention age (~300 Ma), though the individual ages increase with decreasing mantle thickness, suggesting a greater influence of the underlying bedrock on the crater retention ages where the mantle is thin. This renders stratigraphic placement of both the surface material and the underlying bedrock difficult, since there are few clues to the origin of the

mantle in photogeologic analysis, and the crater retention ages are somewhat unreliable for reasons previously discussed. However, since the unit as a whole is topographically continuous with and shares geomorphic features with Asp4, it is probable that the underlying bedrock is part of the Asp4 unit.

Therefore, based on present topographic variation, interpreted stratigraphic relationships, and crater retention model ages, the interpretive minimum sequence of events is (Fig. 3.19):

1. >1 Ga: Formation and modification of the Noachian cratered highlands. A topographic low is produced by an unknown mechanism (possibly initial flooding events), providing accommodation space for later basin fill.
2. 700–1000 Ma: Deposition of Asp1 flows, stratigraphically continuous with AHv of the Tharsis Montes Formation to the east.
3. 700–800 Ma: Initial or continued carving of Mangala Valles into Noachian Highlands bedrock and formation of both the central and western of the northwestern channels by aqueous outburst sourced at Mangala Fossa.
4. 400–500 Ma: A series of flood lava flow events sourced at Mangala Fossa, which extended along the majority of the southern and central valley toward the northern and northwestern reaches of the system, partially filling the easternmost northern channel and filling the central northwestern channel nearly to its mouth.
5. ~400 Ma: Another megaflooding event, which deepened and resurfaced the western side of the valley, widened the original northwestern channels and incised the youngest, easternmost northwestern channel, segmented the entire

western margin of the Asp2 volcanic assemblage, and carved canyons into and partially resurfaced its interior.

6. 300–400 Ma: Continuation of effusive volcanism in relatively low volumes, resulting in the emplacement of the youngest flow along the new topographic lows to form Asp3 surfaces.
7. ~300 Ma: Emplacement of aaeolian sedimentary deposits of unknown source in the northern portion of the study area.

The above dates are given based on crater counts of presently exposed surfaces. Older surfaces that have been modified or buried by later flows and channels cannot be dated, therefore it is difficult to place a reliable lower time constraint on phases of volcanism and channel formation. The events listed above only include those that are directly supported by our observations. We cannot rule out possible additional events that were erased by the events that followed, especially those that preceded the oldest flooding event resolved in our crater counts. Therefore, it is entirely possible that Mangala Valles was primarily incised during multiple megaflooding events that took place within the timeframe of 1–3 Ga.

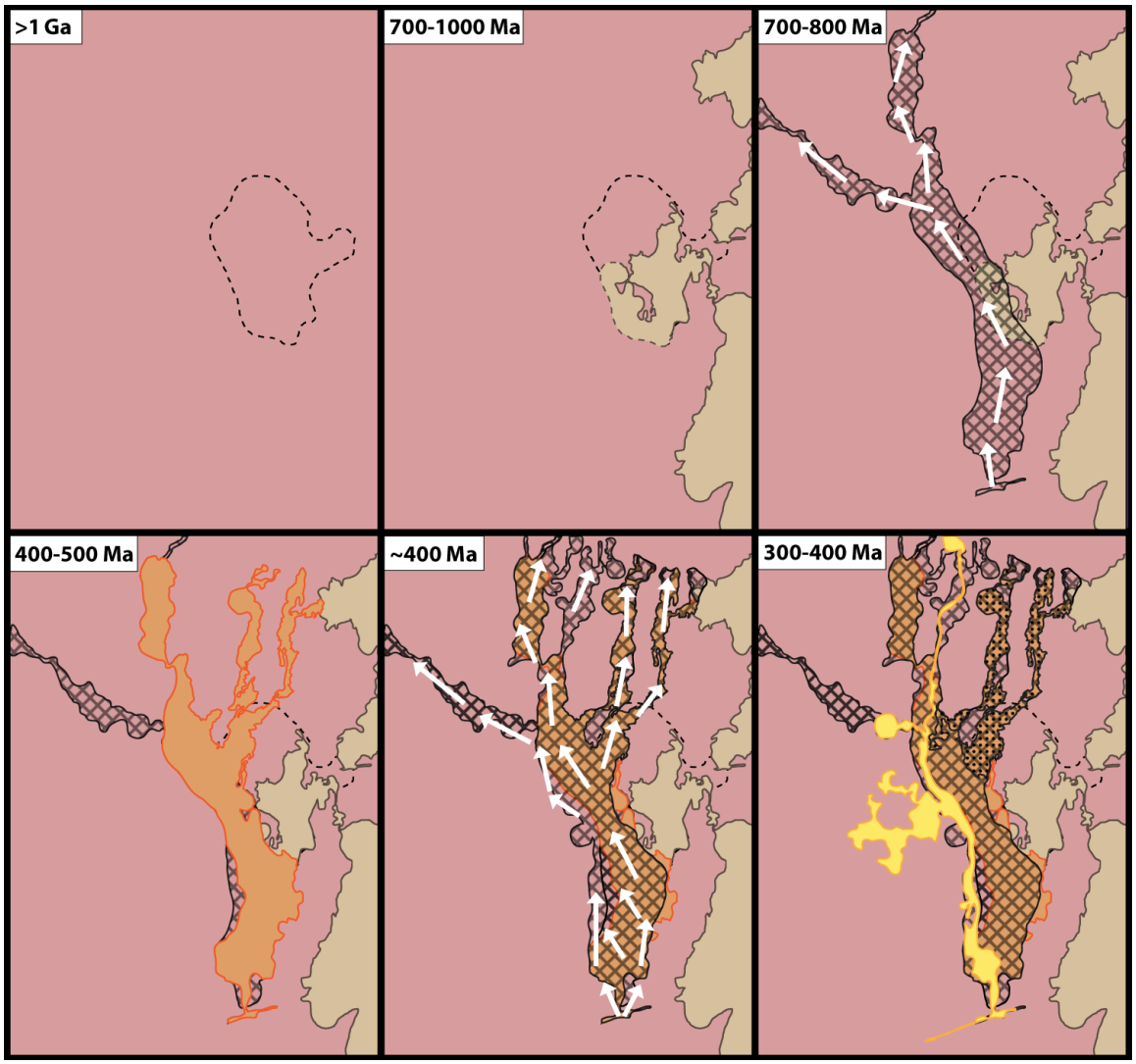

Figure 3.19. Minimum sequence of events as interpreted from crater counts and stratigraphic relations. (1) >1 Ga: A topographic low is produced by an unknown mechanism to an unknown extent, providing accommodation space for later basin fill. (2) 700–1000 Ma: Deposition of Tharsis lava flows (brown) from the east. The southern extent of these flows is unknown. (3) 700–800 Ma: Flooding and incision of Mangala Valles into highland bedrock, sourced at Mangala Fossa. Extent of incision crosshatched, arrows indicate flow direction. Note that there is no evidence suggesting that this was the first flooding/incising event to occur in Mangala. It is entirely possible that older events took place whose evidence has been erased by subsequent events. (4) 400–500 Ma: Deposition of relatively young voluminous lava flows into the valles, sourced at Mangala Fossa (orange). (5) ~400 Ma: Another valley-carving flooding event that deepened and widened the valles toward the west and incised a third northwestern channel. (6) 300-400 Ma: Emplacement of youngest volcanic units along the new topographic low to the west (yellow) and emplacement of sedimentary deposits in the north (extent dotted).

3.4.5 Comparison with previous work

Our geological maps, unit interpretations, and conclusions generally agree with those of Tanaka and Chapman (1990, 1993). These authors hypothesize that there was an initial chaotic fluvial outburst event that carved the original valley, followed by a phase of volcanism that deposited large volcanic plateaus, possibly in concert with more fluvial activity. We generally agree with this hypothesis and augment these interpretations by constraining the sequence of events to include at least seven distinct events or phases. Studies favoring dominantly fluvial processes within Mangala Valles (Zimbelman et al., 1992; Ghatan et al., 2005; Basilevsky et al., 2008) differ from our interpretations in some crucial ways. For instance, volcanic processes, apparent in higher-resolution image data, may better explain some of the features in these studies that were interpreted as produced by fluvial processes.. On the other hand, many of the features we have identified are difficult to explain by volcanic processes alone. We also note that while we cannot rule out the potential role of glacial processes in the formation of the geomorphology of Mangala Valles, we see no features that support that interpretation. Overall, we find that volcanic, fluvial, or aaeolian processes can explain each geomorphology observed, either alone or in combination.

3.5. Conclusions

Results from our mapping and crater counts suggest the occurrence of at least three major volcanic phases and at least two major fluvial events. Given our observations, Mangala Valles was carved by at least one large fluvial event—likely chaotic outburst flooding event(s) resulting from dike intrusion of the subsurface hydrological system at

Mangala Fossa—one of which occurred ~700–800 Ma. This event occurred within the timeframe of the deposition of pahoehoe-like lavas from Tharsis at the northeastern portion of the system during ~700–1000 Ma. A second volcanic phase ending at ~400 Ma saw the emplacement of multiple voluminous, fluid lava flows sourced at Mangala Fossa that filled the majority of the valley. At ~350–400 Ma, another megaflooding event of similar scale to the first resurfaced and expanded the valley. A final volcanic phase occurring at ~350 Ma filled the west valley and much of the floors of the northwestern channels. Although the duration of each phase remains uncertain, it is clear that Mangala Valles remained active over a considerable period of time, with a recurrence of volcanic episodes in between major fluvial episodes.

The close interplay of fluvial and volcanic activity suggests that fluvial activity not only played a major role during a period of volcanism, but also may be linked to, or even triggered by, volcanic processes. If the cryospheric seal of a subsurface aquifer is subject to heating by intrusive igneous activity, resulting in fracture and catastrophic release of its hydrologic reservoir (as modeled by Wilson and Head (2002) and Thakur et al. (2007)), then subsequent eruptive activity may logically follow. Evidence of repeated episodic behavior therefore indicates recharging and repeated interaction of hydrological and igneous subsurface sources over a relatively long period of time in the Late Amazonian. Such activity was no doubt bolstered by the structural activity in the area, the relative youth of which is apparent in the cross-cutting relationships between thrust faults and the younger units (e.g., Fig. 3.16b) (see Tanaka and Chapman (1990) for detailed discussion of regional structural relations). This intimate relationship between tectonic, volcanic, and aqueous activity augments current ideas about complexity of the Memnonia Fossae region and its

relationship to Tharsis-related volcanism and tectonics. Ares Valles and the Kasei Valles and Echus Chasma system have been suggested to share this episodic behavior, but at a much earlier time in martian history (Warner et al., 2009; Chapman et al., 2010), indicating that Mangala Valles represents a younger expression of what may be a similar subsurface process. Detailed comparative studies of other more recently active fluvial–volcanic systems such as Athabasca Valles (Jaeger et al., 2007, 2010) may aid in determining whether repeated fluvial and volcanic behavior has occurred elsewhere contemporaneously or as unique, isolated systems in space and time, potentially providing insight as to whether hydrothermal activity on Mars has been scattered throughout time or has instead occurred in high-volume, global volcanic pulses (Anderson et al., 2001; Wilson, 2001; Neukum et al., 2010).

3.6. Acknowledgments

We are grateful for the detailed and insightful reviews provided by Jim Zimbelman and Mary Chapman. The MRO project and Arizona State University School of Earth and Space Exploration supported this work. CWH acknowledges funding support from MDAP Grant # NNX13AK62G.

CHAPTER 4

MAJA VALLES, MARS: A MULTI-SOURCE FLUVIO-VOLCANIC OUTFLOW CHANNEL SYSTEM

This chapter is a manuscript in preparation co-authored by P. R. Christensen.

4.1. Introduction

Next to impact cratering, effusive volcanism has been the most significant agent of resurfacing on Mars throughout its geologic history, and as a result the majority of the surface is populated by volcanically-derived geologic units (e.g., Greeley and Spudis, 1981; Tanaka et al., 2014). Thus, it is imperative that a volcanic origin is considered for all observed landforms, including for large outflow channels. However, the resemblance of many geomorphic attributes within these channels to those associated with cataclysmic floods of water on Earth, including wide, grooved channel floors and streamlined landforms, has resulted in a prevailing community preference for aqueous flooding on immense scales as the process responsible for the formation of outflow channels on Mars (e.g., Baker and Milton, 1974; Baker, 1978, Mars Channel Working Group, 1983; Head et al., 2003; Komatsu and Baker, 2007; Burr et al., 2009). More recently, this hypothesis has been challenged by observations of lava flow morphologies draping channels in Athabasca Valles that meet the morphometric criteria to allow for flows in the transitional to turbulent flow regime, particularly for low-viscosity flows (Jaeger et al., 2007, 2010). Because the lava that completely coats the channels is sourced from the same set of fissures that sources the channels themselves, Cerberus Fossae, the authors could not eliminate the possibility

that the lava flow thermomechanically eroded the channels. Some investigators have since used these observations at Athabasca to argue that other outflow channels exhibiting effusive volcanic morphologies issuing from the same source as the purported water source may have been instead eroded by lava (e.g., Leverington, 2011). The largest known examples of lava-eroded channel systems in the solar system are located on Venus (e.g., Komatsu et al., 1992, 1993), and are often cited as a volcanic analog for fluvial features observed on Mars (Leverington, 2009, 2011). In particular, a ~300-km segment of the 1200-km long Kallistos Vallis bears a braided, anastomosing appearance common among martian outflow channels (Baker et al., 2015). However, the present-day conditions on the surface of Venus are much more favorable for producing and maintaining the high-temperature, low-viscosity lavas required for erosion in comparison to Mars. Low viscosities and low melting points allowing for longer travel distances and more favorable conditions for turbulence may also be achieved by exotic compositions occasionally found on Earth such as carbonatite or sulfur flows, which have been proposed for Venus (Komatsu et al., 1992, 1993), but lava flows of these compositions have yet to be identified on Mars. The quantities of fluid—lava or water—required to erode martian outflow channels are immense: with excavated volumes on the order of 10^3 km^3 for channels the size of Mangala Valles, the volumes of erosive fluid would have been 10^3–10^4 km^3, depending on a variety of conditions including its erosive and sediment-carrying capacities as well as the strength and structure of the substrate (Komar, 1979, 1980). Mechanisms of subsurface storage, catastrophic release, and subsequent recharge of such volumes remain poorly constrained (Komatsu and Baker, 2007), and it is arguably easier to justify eruption of the same volume as lava, though maintaining a turbulent flow regime is extremely

challenging for the reasons listed above. On the other hand, the absence of enormous lava flow deposits at the outlet of every Martian outflow channel weakens arguments that lava alone is responsible for outflow channel formation. In fact, the imbricate arrangement of boulders as imaged by Pathfinder, which landed in Chryse Planitia at the mouths of multiple outflow channels, offers evidence of fluid flow and sedimentary deposition in that location (Smith et al., 1997; Chapman and Kargel, 1999) that could not be achieved by lava flows. While the fluvial hypothesis remains the predominant view, it is nevertheless important to address the lava erosion formation hypothesis. Here, we present evidence from an as-yet relatively poorly-studied martian outflow channel that shows that it has undergone fluvial and volcanic activity sourced from separate locations, with only the fluvial source having eroded channels. Our findings strengthen the majority view that other martian outflow channels harboring both fluvial and volcanic morphologies issuing from a single source may have a similar history involving water as the erosive agent and lava flows primarily as a constructive agent.

Maja Valles is a 1200-km long outflow system situated to the north of Vallis Marineris and south of the Kasei Valles outflow system in the Chryse Planitia region (Fig. 4.1), where it divides the smooth volcanic plains of Lunae Planum to its west from the older Xanthe Terra highlands at its eastern flank. It originates at Juventae Chasma, a set of canyons that are part of the Vallis Marineris system, extends toward the north, and curves toward the northeast before debouching onto Chryse Planitia. The system was first described by Sharp and Malin (1975) and mapped by Baker and Kochel (1979) using images from Viking (Carr et al., 1972), who along with later authors (Scott and Tanaka, 1986; Witbeck et al., 1991; Rotto and Tanaka, 1995) placed its origin in the late Hesperian

on the basis of impact crater population densities measured using Viking images. However, Chapman et al. (2003) more recently documented evidence of crater density variations within the Maja Valles system derived using images from the Mars Orbiter Camera (MOC) (Malin and Edgett, 2001) suggesting that the formation history of Maja Valles may involve multiple resurfacing events. In this study, we determine the roles played by volcanic and fluvial processes in the geologic history of Maja Valles using morphologic indicators and observations of stratigraphic relationships supplemented by crater retention age dating.

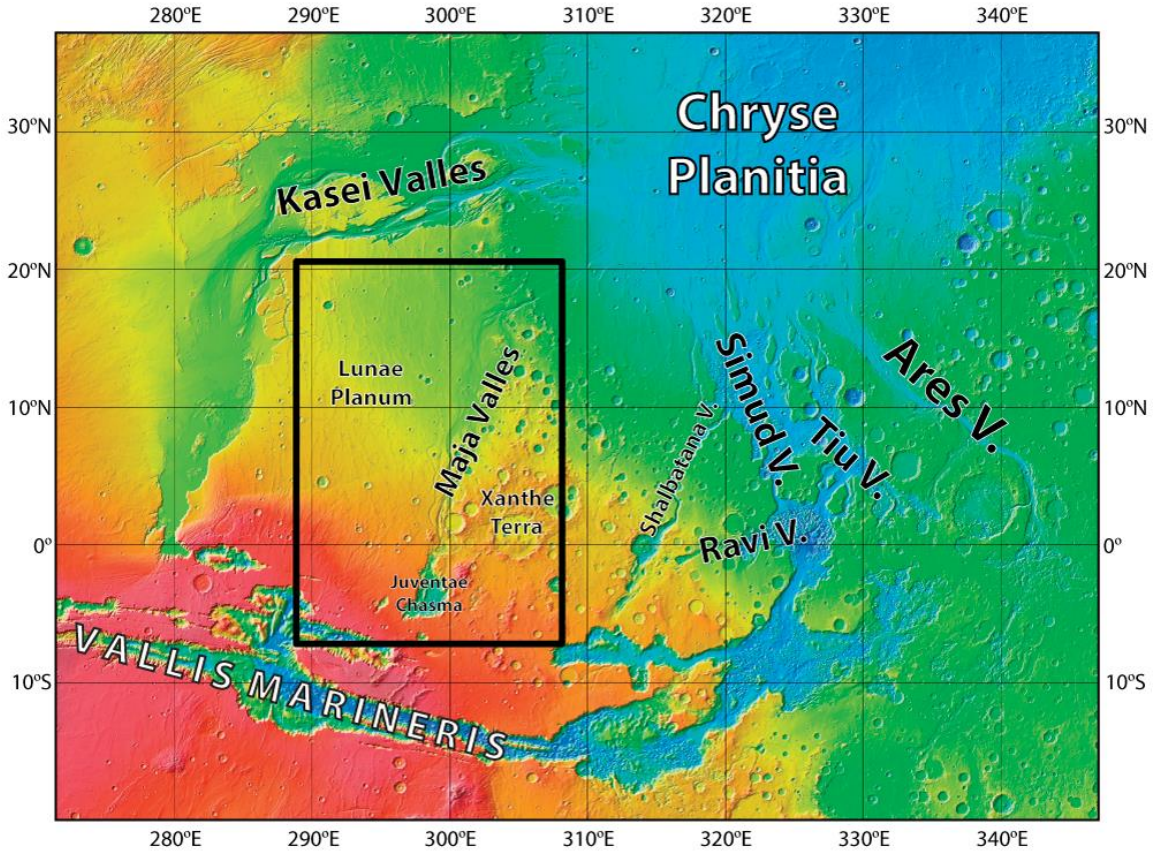

Figure 4.1. Context map of the Chryse Planitia/Valles Marineris region of Mars. Black inset denotes study area. Mars Orbiter Laser Altimeter (MOLA) shaded relief/colorized elevation (Smith et al., 2001).

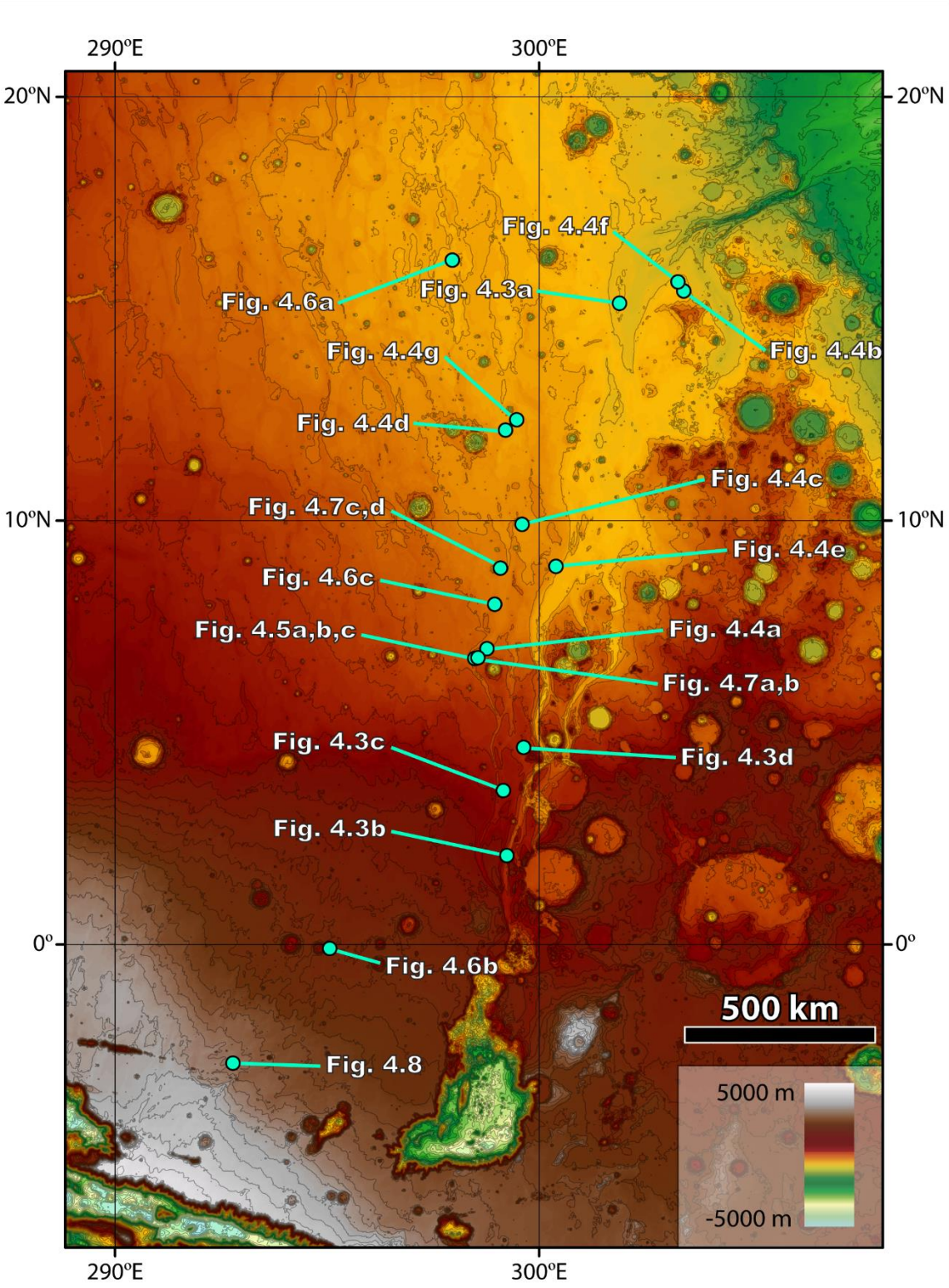

Figure 4.2. MOLA elevation map of the study area with figure locations. Contour interval 200 m.

4.2. Photogeomorphology

4.2.1 Valley fluvial landforms

In order to evaluate erosive processes, the landforms preserved in Maja Valles were examined using all available images from the Context Camera (CTX) (Malin et al., 2007) and the High Resolution Imaging Science Experiment (HiRISE) (McEwen et al., 2007) covering the valles and east Lunae Planum. As noted in previous works, Maja Valles host a vast array of landforms interpreted as fluvial in origin akin those found in other martian outflow channels such as streamlined islands (Fig. 4.3a,e), terraced channels whose floors have been scoured with deep longitudinal grooves (Fig. 4.3a,b), horseshoe-shaped head cuts (Fig. 4.3d), and segments of braided inner channels (Fig. 4.3e). Fluvial features predominate in south Maja Valles and generally diminish in scale and relief downstream, where the channels widen onto flatter terrain (Fig. 4.2). For greater detail of fluvial features found in Maja Valles, we refer the reader to Baker and Kochel (1979) and Chapman et al. (2003).

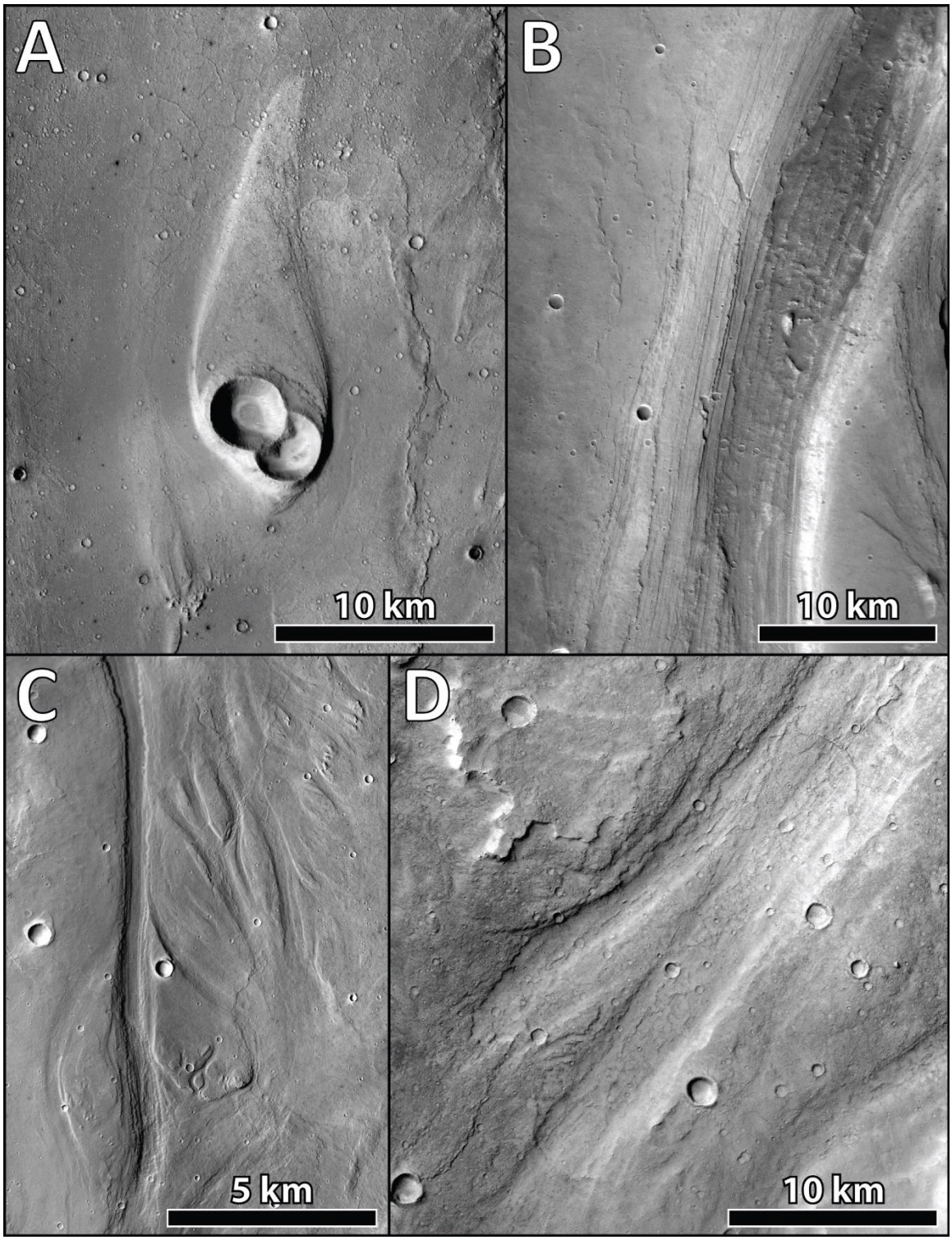

Figure 4.3. A) Streamlined island formed around a double impact crater. Exposed ledge of pre-existing crater rim indicates an erosional (i.e., non- aggradational) origin. B) Narrow channel confined by steep terraces with longitudinal striations on bed. Note small pre-existing impact craters on channel floor exhibiting a subdued appearance. C) Intricate set of anabranching channel forms. D) Horseshoe-shaped head cuts or knickpoints marking stronger downcutting as floodwaters were forced into a narrower channel. All images CTX.

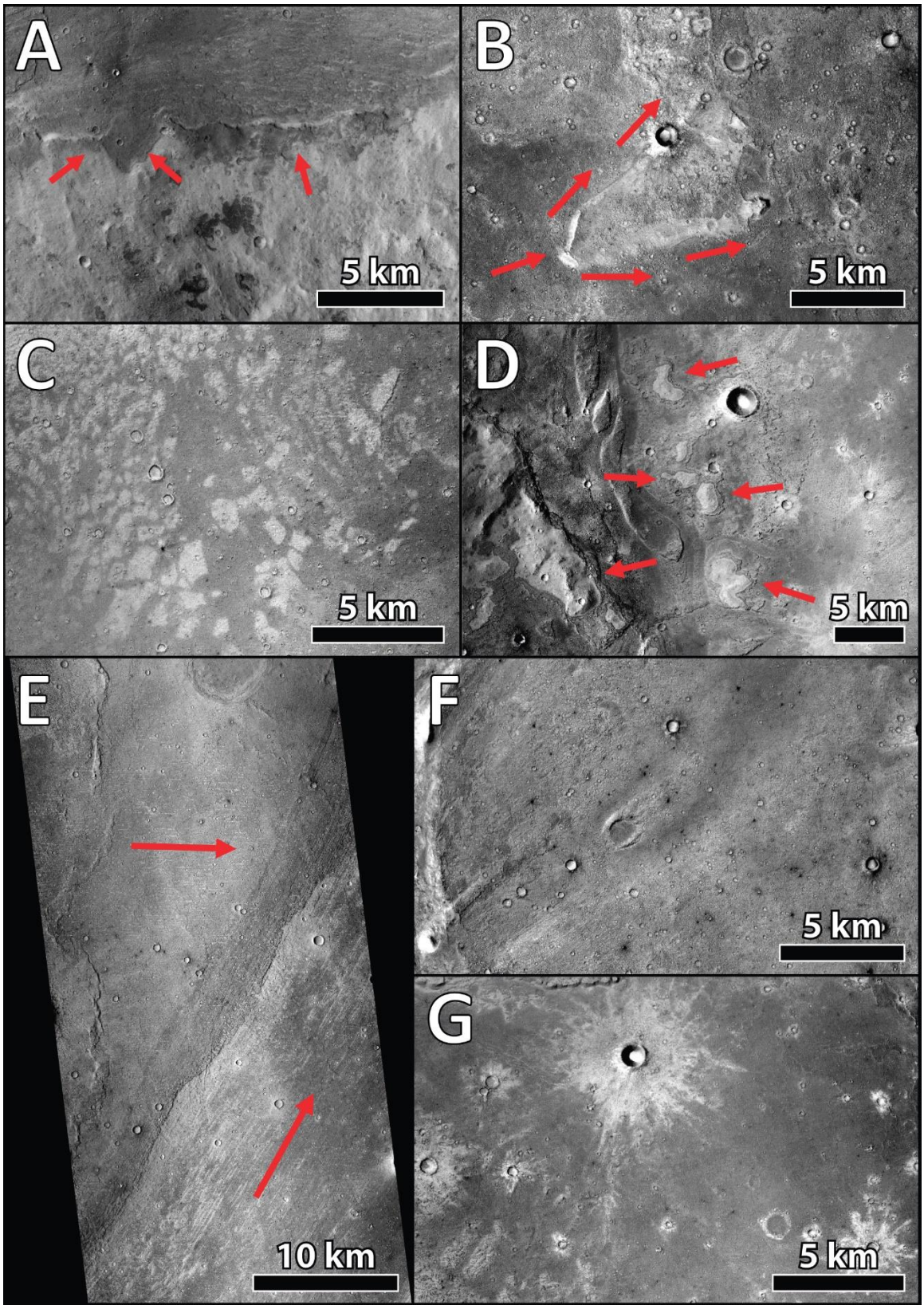
A
5 km
B
5 km
C
5 km
D
5 km
E
10 km
F
5 km
G
5 km

Figure 4.4. Examples of morphologies suggesting effusive volcanism in the valles (CTX). A) Arrows indicate a bench where the thickness of the lava flow exceeded the depth of the channel and spilled over its banks. B) A wake formed behind an obstacle in the pre-existing topography. This image also shows the pockmarked appearance of these lava flows, which indicate a pitted surface. Arrows denote interpreted flow direction. C) Albedo variations in the form of polygons, which may have formed as a cooled surface was torn apart and rafted. D) Arrows mark bathtub rings marking kipukas formed around pre-existing knobs in the terrain. E) A very thin veneer of lava (dark) unevenly coating a fluvial surface (light), filling in the lows between ridges, having drained away from the highs. Also present are fine striations in the lava flow, oriented independently of pre-existing striations produced by fluvial processes. F) A pre-existing streamlined island that has been partially buried by a later lava flow. G) A high incidence-angle image of craters exhibiting bright ejecta, exposing material from the underlying surface. All images CTX.

4.2.2 Valley volcanic landforms

Most prominently in the northern portion of Maja Valles are many features resembling volcanically-derived landforms including sinuous lava channels, lobate flow fronts (Fig. 4.4a,b,d), lava rise pits, collapse pits, infill of small craters, embayed landforms (Fig. 4.4b,d), kipukas (Fig. 4.4d), bathtub rings (Fig. 4.4d), and platy-ridged morphology resembling rafted lava crust (Fig. 4.4c). Morphological features such as elongated pits and muted ridges (Fig. 4.4e) are interpreted to be the result of lava draping pre-existing ridged topography following drainage, most evident in locations where lava has partially submerged old streamlined islands (Fig. 4.4f). The expression of underlying topography suggests a relatively thin coating from a low-viscosity basaltic lava flow. In high-incidence angle images, ejecta blankets of fresh craters as small as 150 m in diameter appear bright in comparison to the surrounding lava flow (Fig. 4.4g). If the ejecta are bright because they are composed of brighter material that has been excavated from underneath the lava flow, then the lava flow may be on the order of ~13 m thick (from depth/Diameter relationship globally for fresh simple craters from Robbins et al. (2012)). Because ejecta blankets are

typically composed of material from the top third of the crater depth (Melosh, 1989), the thickness of the lava flow may be as thin as 4 m.

Particularly notable features within and off of the margins of these flows are isolated patches of dark, relatively pristine material of similar morphologic and thermal characteristics to their adjacent flows (Fig. 4.5, 4.6). These smooth patches of material tend to occur in places where lava may have pooled during drainage, such as local topographic lows perched at an overall higher elevation than the final elevation of the lava flow surface following drainage (best seen on crater pedestals, Fig. 4.5, 4.6b,c) or in localities where obstructions trapped a portion of the flow (Fig. 4.6a). In many cases, the crust that formed prior to drainage appears to have been fragmented and rafted during drainage (Fig. 4.5c, 4.6a), however HiRISE and CTX Digital Terrain Models show that for the most part individual patches tend to maintain equal elevation along their edges, implying that they were probably at least partially fluid upon emplacement (Fig. 4.7). Therefore, the maximum elevation of the occurrence of these patches may serve as an indicator of the local lava high stand of one or more low-viscosity lava flows in the valles. The higher elevation of the patches relative to their adjacent channel floors indicates emplacement by inflated lava flows that have since drained.

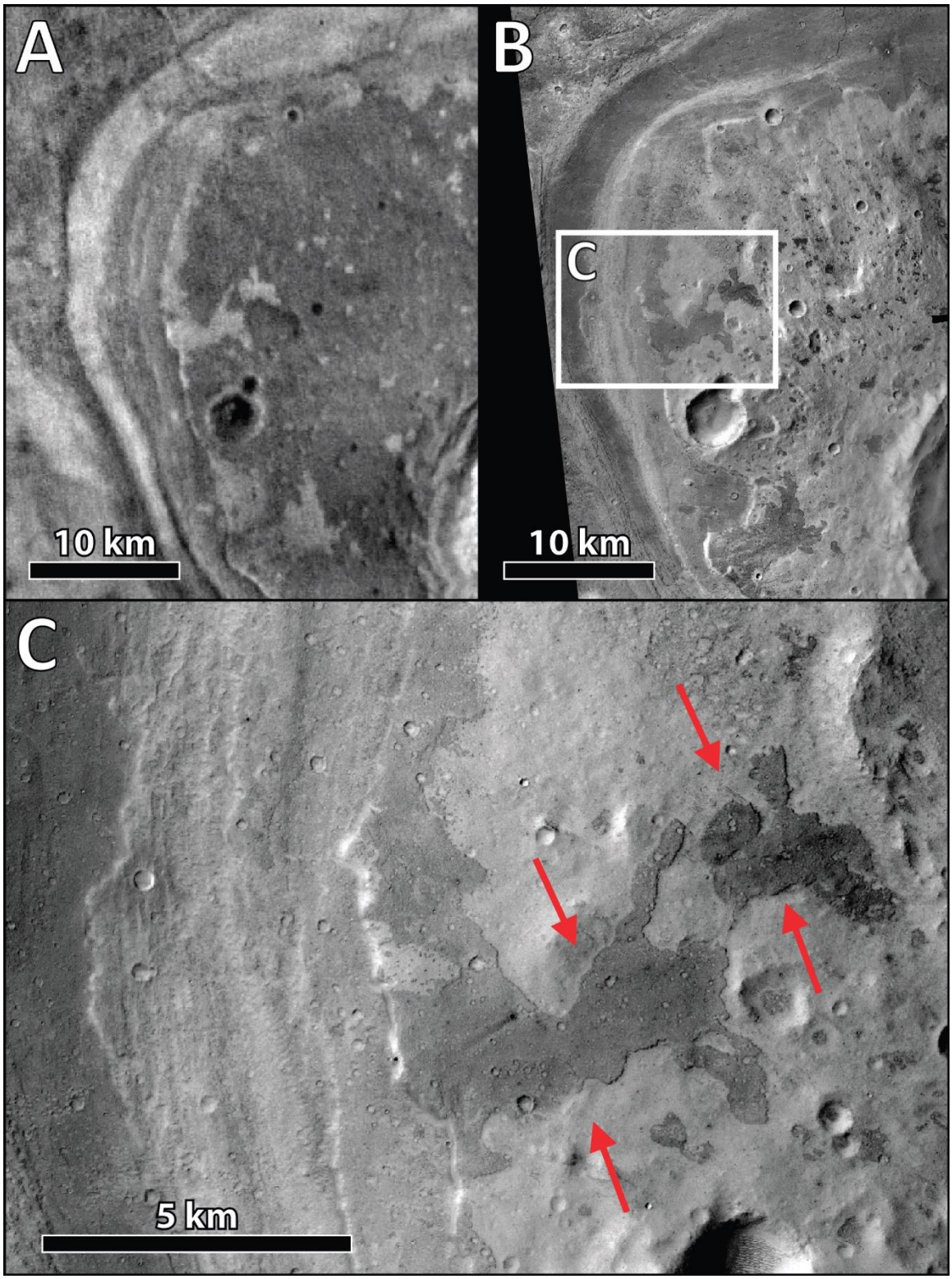

Figure 4.5. Example of smooth patches in Maja Valles. The smooth patches tend to be bright in THEMIS Night IR (A), suggesting that they are composed of more coherent, higher-density material than their surroundings. C (HiRISE) demonstrates the smooth character of the patches, as well as their morphologic similarity to the adjacent flow.

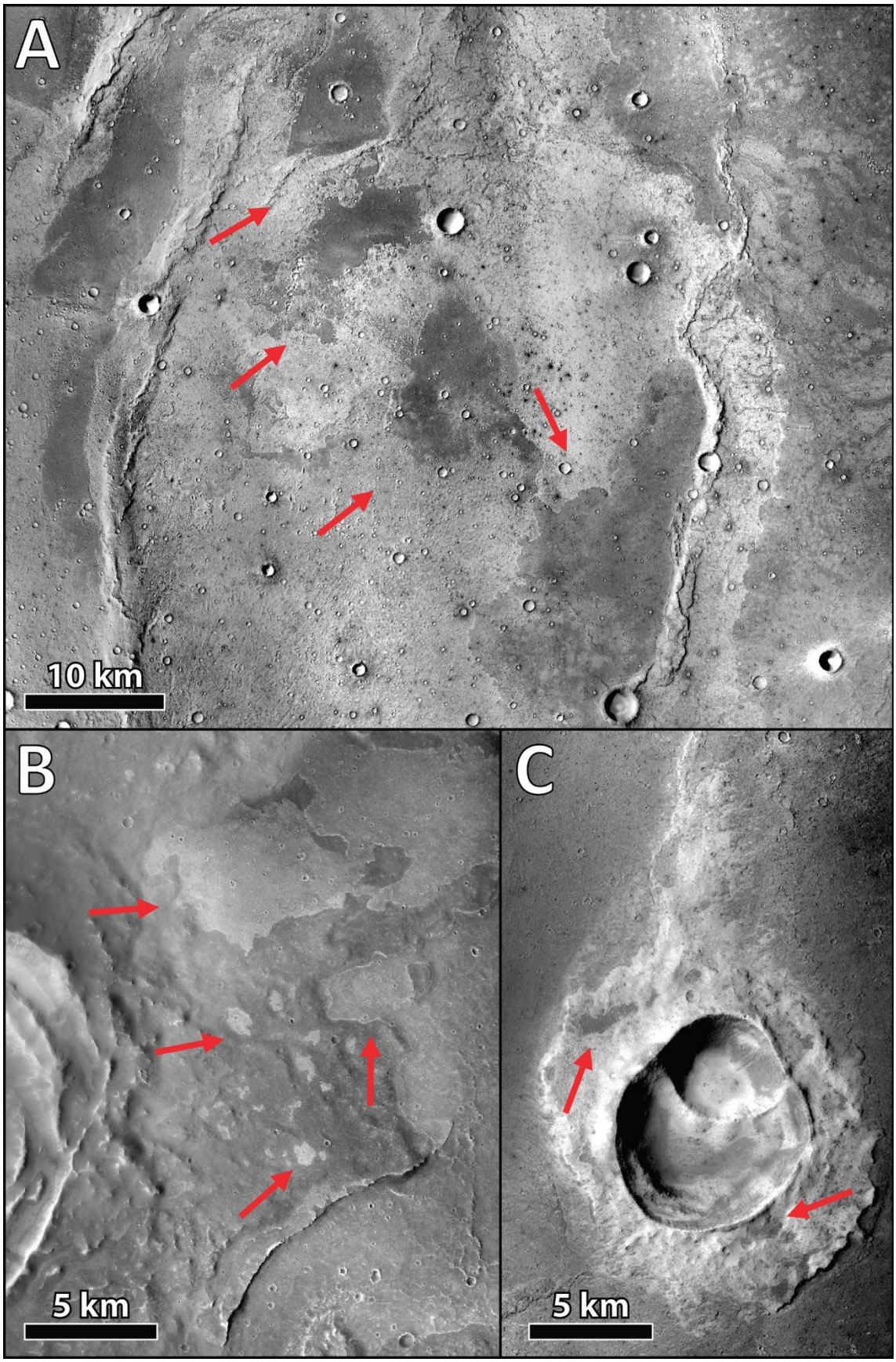
A
10 km
B
5 km
C
5 km

Figure 4.6. Examples of smooth patches identified in Maja Valles and Lunae Planum. While the majority of smooth patches appear dark in visible images (panels A, B), most of the examples in Lunae Planum appear brighter than the surrounding bedrock (panel C). However, even in these cases they still remain brighter than their surroundings in THEMIS Night IR. Most exposures of smooth patches appear on crater pedestals, however panel A shows an example of smooth patches confined between pre-existing wrinkle ridges. The edge of the continuous portion of the flow can be seen on the righthand side of the image. All images CTX.

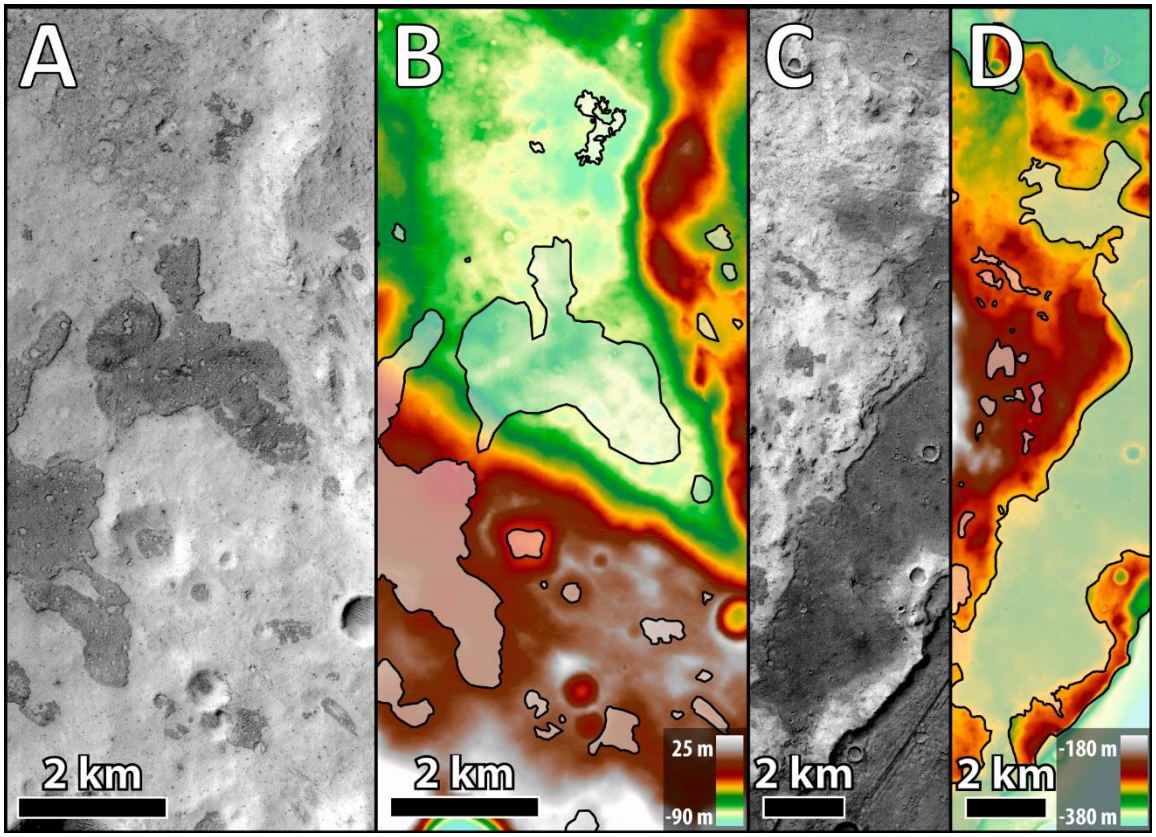

Figure 4.7. HiRISE orthophotos and DTMs showing the tendency of perched smooth patches to pool within local topographic lows, indicative of a fluidic origin.

Due to the thin, draping character of many of the lava flows in this region, tracing their extent using topography and visible images alone is often difficult, even given the high spatial resolution provided by CTX. Despite the area being entirely too dusty to perform any compositional analyses using near-infrared or mid-infrared spectroscopy, many of the flows that are difficult to follow using visible imagery appear sufficiently bright in the night infrared mosaic from Thermal Emission Imaging System (THEMIS)

(Christensen et al., 2004) to distinguish from one another. From a regional scale, THEMIS Night IR (used as a basemap in Fig. 4.9) shows that multiple lava flows have fed into Maja Valles from the west that appear to be sourced from a chain of pits in south Lunae Planum (which includes Ganges Catena and Ceti Chasma), west of Juventae Chasma. Marra et al. (2015) interpreted the flows from these pits as fluvial outflow channels; however, erosional streamlined features, ridged topography, or any other diagnostic morphological indicators pointing exclusively to fluvial erosion are absent. Instead these the pits appear to have issued thick assemblages of lobate landforms, some of which have filled parts of the fissures and are crosscut by leveed lava channels (Fig. 4.8). All of these features point to constructional deposition, rather than erosion. Construction is also supported by the shape of the contours in Lunae Planum (Fig. 4.2), which bow outward along the path of the flows, rather than inward as would be the case for eroded channels, such as the Maja channels. There is also no evidence that any fluvial landforms are buried beneath the lava flows near these pits nor anywhere along their path before intersection with Maja Valles channels. Therefore, it seems these pits served as vents for the lava flows in Lunae Planum.

Presented in Figure 4.9 is a map of lobate margins, sinuous rilles (i.e., lava channels), and smooth patches identified in Maja Valles and east Lunae Planum. Most of the lava flowed generally northward from the source vents until roughly 7°N, where they turned northeastward and spilled into the valles. Some flows took a more directly eastward approach from the vents and intersect the channels nearer Juventae Chasma, though this path appears to have been much less favored. Exposures of lava morphologies become increasingly sparse toward the eastern portion of the valles, and can only be seen on local

highs (such as streamlined islands), or are highly degraded. This may be an effect of thinning of the lava flow(s) eastward or of post-emplacement fluvial activity.

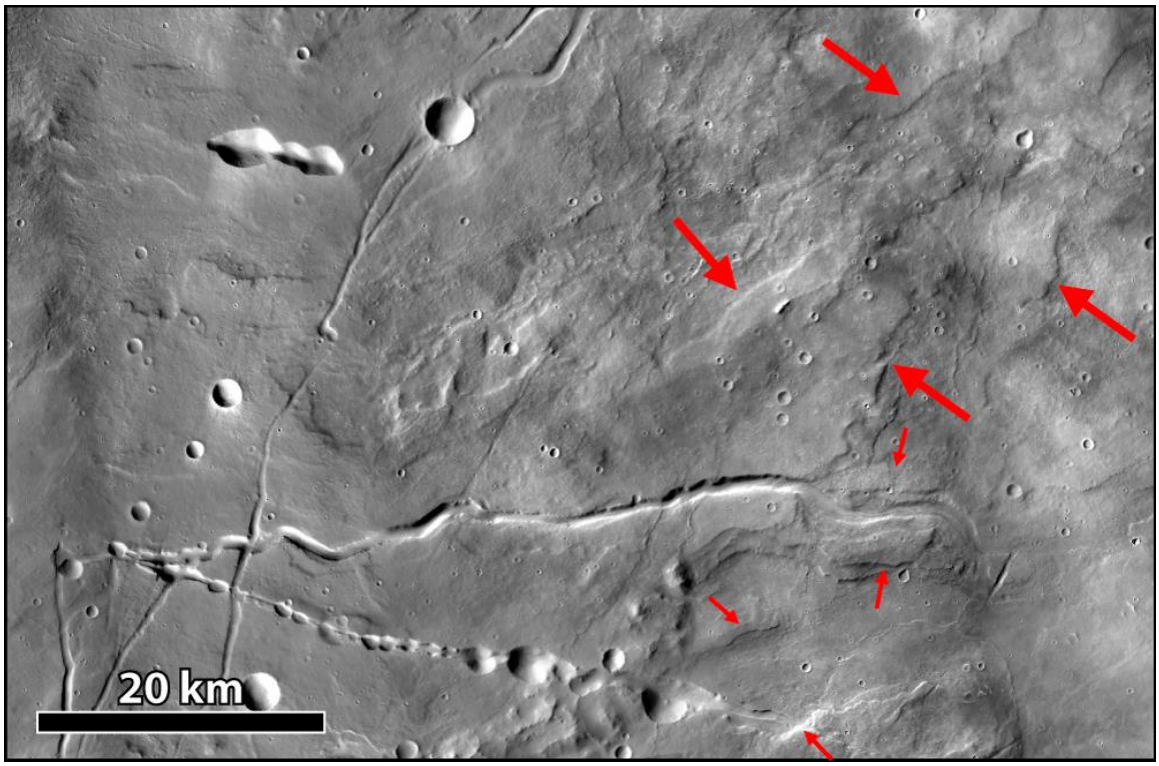

Figure 4.8. Part of the fissure/crater pit chain serving as a source of lava flows in Lunae Planum. The ESE-trending pit chain issues assemblages of lobate landforms flowing NNE (large arrows), which appear to have buried part of the fissure (bottom right). Multiple sinuous lava channels issue from the pits, one of which has constructed levees (upper set of small arrows) along its path across a broader, more shallowly leveed channel (lower set of small arrows) in the bottom right. Another pit chain is present in the upper left (CTX composite).

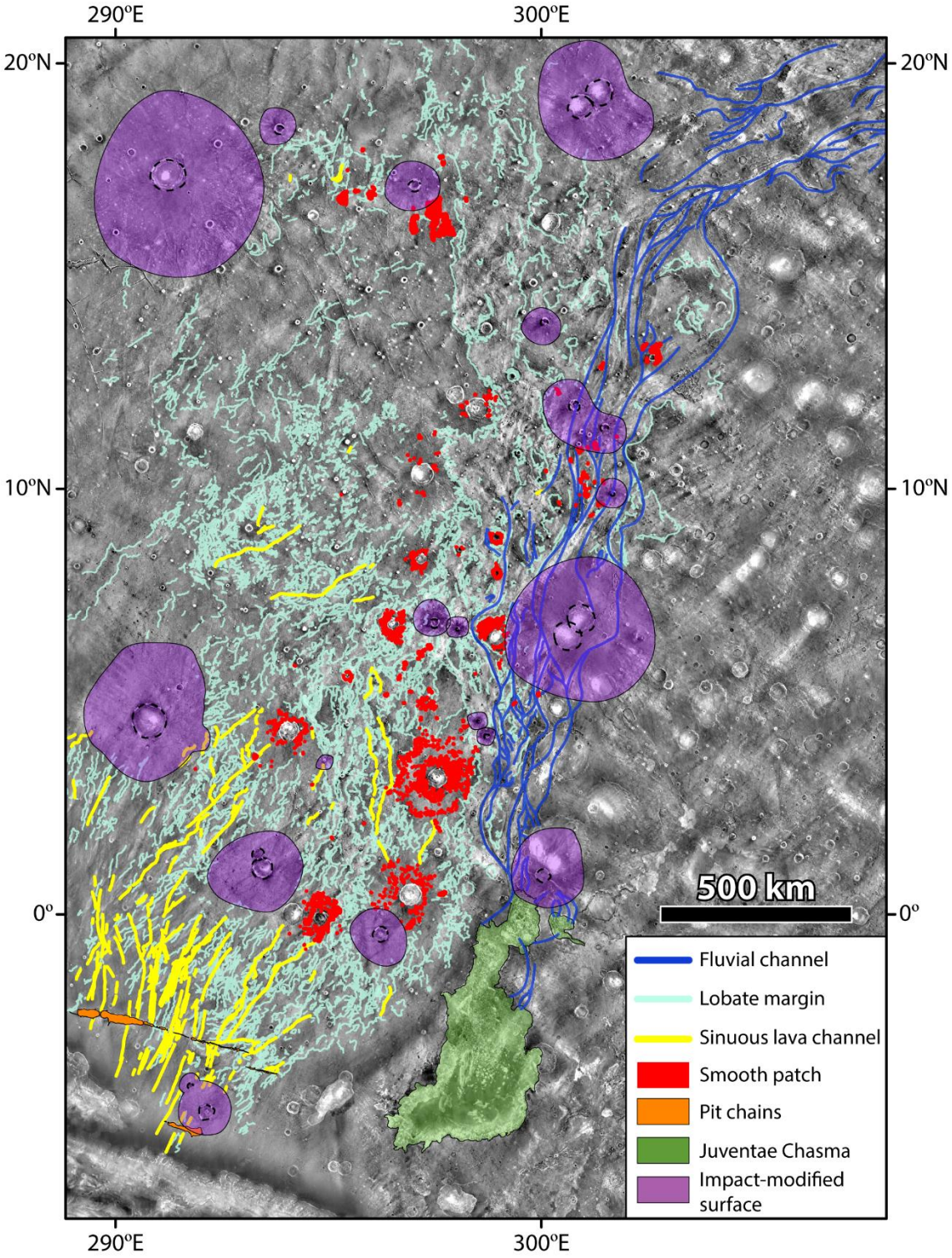

Figure 4.9. Map of lava flow morphologies observed in Maja Valles and east Lunae Planum over THEMIS Night IR mosaic (contrast adjusted).

4.3. Crater retention age dating

Crater population densities were derived using crater counting techniques as described in Michael and Neukum (2010) on a diverse set of surfaces within the study area expected to represent various resurfacing events. All craters larger than 50 m in diameter were counted using CTX images in 28 individual homogeneous areas ranging from ~200 to ~4500 km^2 in surface area per count (Table 1, Fig. 4.10). Model crater retention ages were then fitted using the chronology and production functions derived in Hartmann (2005) with $\sqrt{2}$ crater diameter bins. Bins that were obvious outliers were excluded from the fit (i.e., only bins that together fell along or near a slope matching the slope of the Hartmann chronology function were included). This approach ensures that ages were not underestimated by including craters near the resolution limit of CTX, nor were they overestimated by including bins with craters that were too large to be resurfaced during the event we were attempting to date. It also excludes bins that may have been affected by aeolian degradation, which tends to shallow the slope of the crater size frequency distribution curve for smaller diameters. In cases where the crater size frequency distribution had two segments meeting these criteria for two separate bin ranges (i.e., on older age and a younger age were shown), the younger age is reported in our results. This is because the sample size afforded by smaller bins allows for smaller uncertainties in the results, and it is also often difficult to determine which bins reliably represent the older age.

Performing crater counts in Maja Valles was unusually challenging because the area appears to have undergone one or more partial resurfacing events, resulting in many craters being only partially filled or eroded. This not only affected the counts themselves,

but also made ambiguous which resurfacing process is reflected in many of the counts. For this reason, we have categorized each area as most recently fluvial, most recently volcanic, or uncategorized (Table 4.1). An additional complicating factor is that the most pristine lava flows are populated with small, shallow pits, which poses a serious problem when counting craters on such surfaces, as many of these pits are very crater-like (see Fig. 4.7a for example of texture in close view). Finally, the region is very dusty (~0.95 dust cover index, Ruff and Christensen (2002)), which serves to somewhat mute smaller craters. Therefore, crater retention ages of individual units should be interpreted with extreme caution.

Figure 4.11 is a graphical representation of our results grouped into their interpretive categories of volcanic, fluvial, or uncategorized. Most of the volcanic surfaces have retention ages near one of two clusters, one centering at ~1 Ga (average 1.01 ± 0.14) and the other centering at ~1.6 Ga (average 1.64 ± 0.06). A more conservative interpretation might instead be that these ages represent multiple lava flow events punctuating the timeline between ~0.7–1.7 Ga. In contrast, the fluvial ages fall into two groups that are much more separated: a younger group at ~0.9 Ga (average 0.87 ± 0.16) and an older at ~2.4 Ga (average 2.35 ± 0.28). Interestingly, two of the three older retention ages are located on the flanks of the mouth of the system, Juventae Chasma, while the other is the retention age of the northernmost outlet (also known as Maumee Valles), suggesting that the oldest of the two fluvial events was farther-reaching than the later event, and possibly greater in discharge, since it managed to overtop the source canyons. On the other hand, the later event may have failed to overtop the canyons simply because the pre-existing channels offered a convenient pre-determined route by which floodwaters could

be efficiently conveyed through the system. Pre-existing channels may also be responsible for failure of the more recent flood to resurface the northernmost channel outlets; thus, we cannot speculate as to which event was greater in volume or power.

Count	Facies	Area (km^2)	Age (Ma)	N	Bin Min (m)	Bin Max (m)
v1	volcanic	564	949 ± 30	988	88.4	500
v2	volcanic	390	1020 ± 60	250	125	500
v3	volcanic	314	1660 ± 160	107	177	707
v4	volcanic	468	1580 ± 70	465	125	354
v5	volcanic	337	1010 ± 70	195	125	354
v6	volcanic	453	769 ± 50	226	125	354
v7	volcanic	262	1080 ± 80	182	125	354
v8	volcanic	565	1030 ± 50	395	125	707
v9	volcanic	4671	1690 ± 20	4827	125	707
v10	volcanic	290	1250 ± 80	236	125	500
f1	fluvial	383	2160 ± 160	181	177	707
f2	fluvial	386	2230 ± 300	54	250	707
f3	fluvial	362	944 ± 110	66	177	500
f4	fluvial	395	1000 ± 110	75	177	500
f5	fluvial	1090	769 ± 37	478	125	354
f6	fluvial	452	1010 ± 60	285	125	500
f7	fluvial	433	1000 ± 110	73	177	500
f8	fluvial	352	679 ± 56	134	125	354
f9	fluvial	419	664 ± 50	171	125	500
f10	fluvial	265	1190 ± 80	224	125	707
f11	fluvial	362	2670 ± 180	169	177	500
u1	unclear	638	1130 ± 50	462	125	1000
u2	unclear	385	1020 ± 40	747	88.4	500
u3	unclear	216	807 ± 34	339	88.4	354
u4	unclear	381	1060 ± 70	242	125	500
u5	unclear	420	1270 ± 70	361	125	707
u6	unclear	461	1650 ± 130	149	177	1000
u7	unclear	283	1800 ± 100	331	125	707

Table 4.1. Summary table of the results of 28 crater counts performed within the study area. Errors presented are calculated from the standard error of the crater population sampled. Fits were based on Hartmann (2005). See Figure 4.10 for map of area locations.

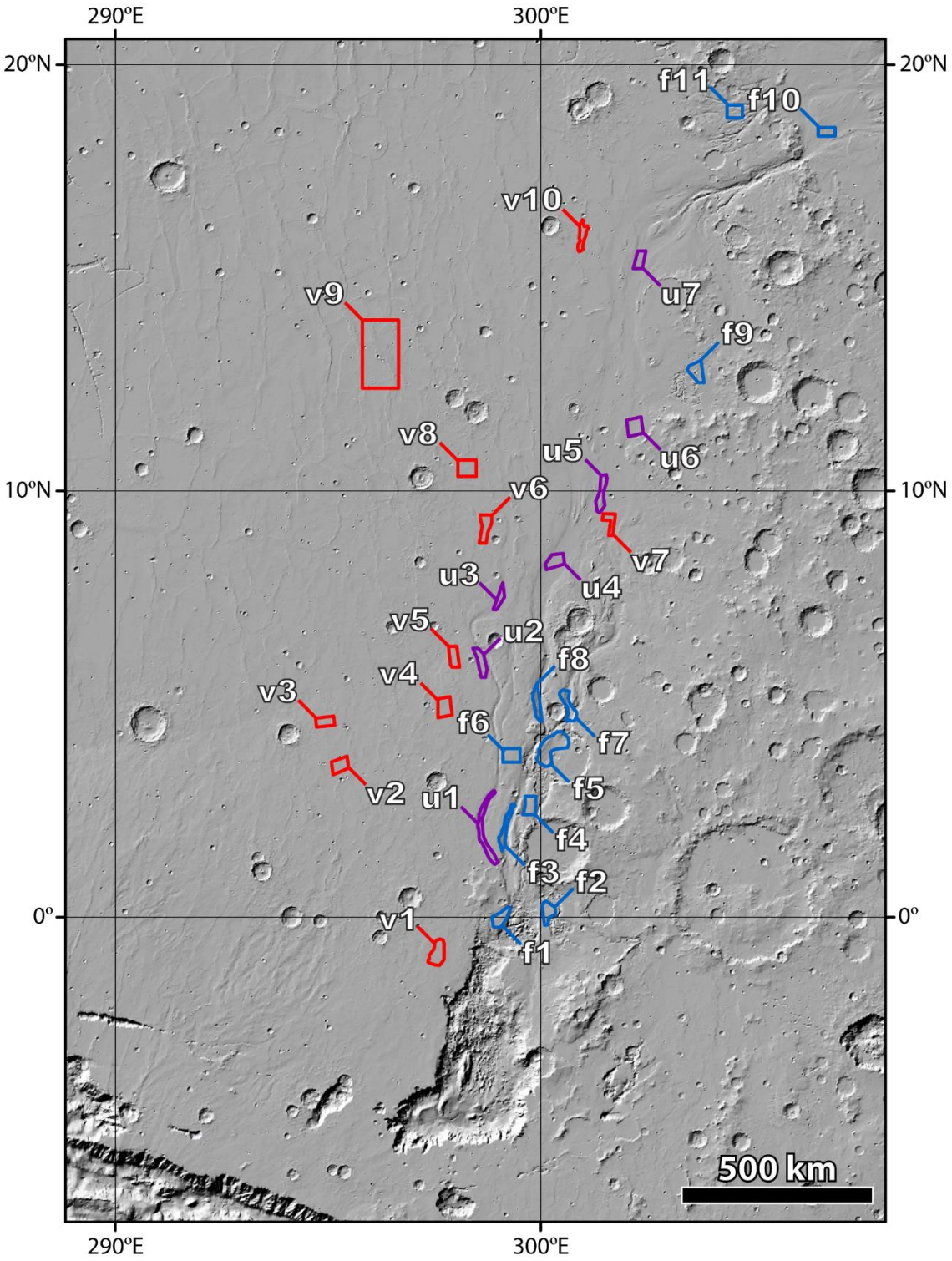

Figure 4.10. Location map of crater counts shown in Fig. 4.11 and Table 4.1, each area labeled with its corresponding crater count number. Red are volcanic areas, blue are fluvial, and purple are uncategorized. Basemap is MOLA shaded relief.

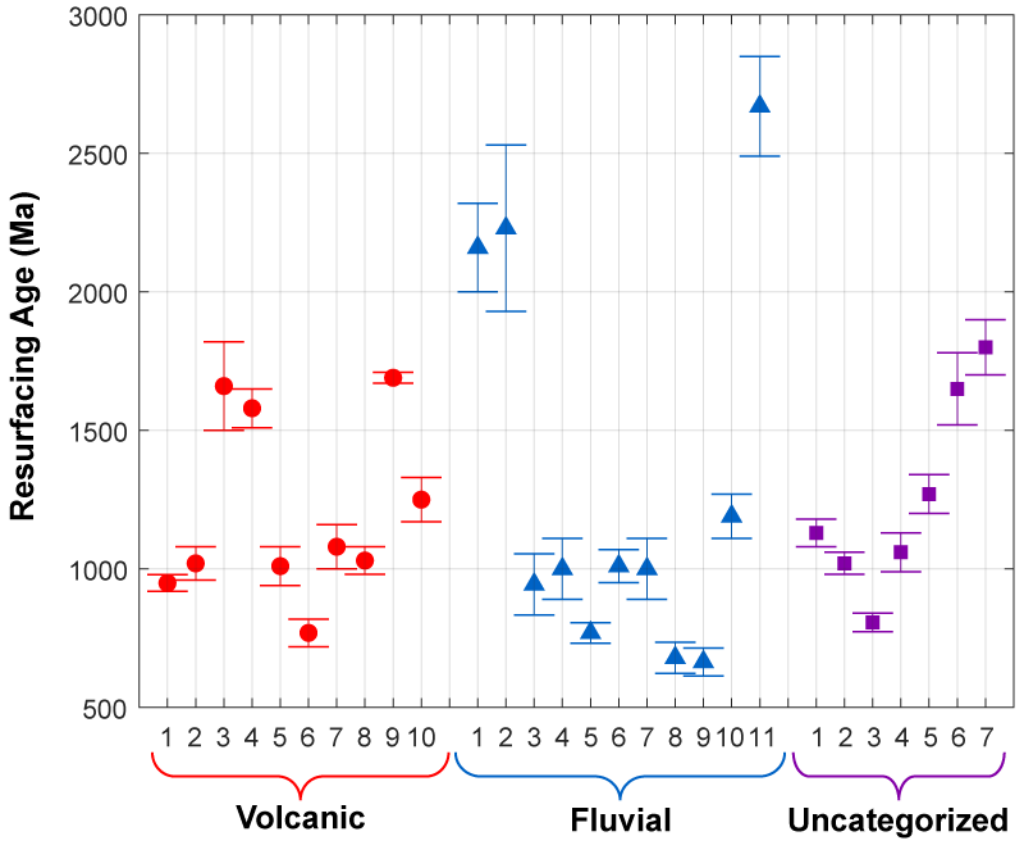

Figure 4.11. A graphical representation of the results of the crater retention ages derived in this study. Red markers denote areas that have been interpreted as most recently volcanically resurfaced, blue markers denote areas that have been interpreted as fluvial surfaces, and purple surfaces are uncategorized. Note that error bars shown represent sampling error alone and therefore do not encompass all uncertainties. Fluvial surfaces are divided into two distinct groups, one ~600–1200 Ma, another ~2100–2600 Ma. Volcanic surfaces also can be divided into two groups of ~700–1200 Ma and ~1600 Ma. These interpretations should be taken with caution given uncertainties inherent in crater counting methodology.

Similar to the younger volcanics, the fluvial and uncategorized retention ages are loosely clustered. This may be a result of varying degrees of resurfacing by thin, mantling lava flows and/or relatively weak floods in these areas. Alternatively, the system may have undergone multiple episodes of activity which took place on a timescale smaller than is resolvable by the crater counting method. Most likely, it is a combination of these factors.

4.4. Discussion and conclusions

4.4.1 Regional geological history

Our findings can be summarized by two main points:

1. Crater retention age dating suggests a sequence of events in Maja Valles involving at least two megaflooding events and at least one, but possibly two lava flow events in the Mid- to Late Amazonian. The disappearance of lava flow morphologies in the eastern portion of the valles leads us to hypothesize that the most recent event in the history of Maja Valles was a fluvial event that flowed predominately along its eastern channels, eroding and/or burying any pre-existing lava flows in sediment. The presence of lava flow morphologies thinly coating and/or embaying pre-existing fluvial landforms indicates that the previous lava flow was preceded by an older fluvial event. Previous authors have indeed hypothesized that the formation of Maja Valles may have involved multiple flooding events (Chapman et al., 2003); here, we provide quantitative support for this hypothesis. Importantly, many of the resurfacing ages derived in this study are remarkably younger than the ages derived in previous studies.

2. There is abundant morphological evidence of both volcanic and fluvial activity within Maja Valles. However, the most pristine flows can be traced to a fissure/pit chain (which we have interpreted as a series of vents) in Lunae Planum, which overlap older lava flows that appear to have followed a similar path. It follows, then, that the source of lavas in Maja is spatially distinct from the source of fluid that incised its channels. Furthermore, despite clear indicators that the lava flows

sourcing from south Lunae Planus were very fluid, there is no topographic evidence that any of the flows carved any prominent erosional channels along their path (Fig. 4.2). In fact, smoother contours and subdued landforms in the portion of the basin filled by lava suggests that it left deposits that coat the valles. Thus, we can say with relative certainty that the process that produced the lava flow deposits in Maja Valles was not the same process that eroded its major channels. While any turbulent medium can theoretically produce the erosional features found in Maja Valles, the absence of lava flow features in the upper reaches of the channels implies that channel incision in Maja most likely occurred by a mechanism other than lava erosion. Water, then, being in abundant supply within the martian subsurface (Boynton et al., 2002), seems the most likely agent of erosion— in agreement with traditional interpretations of outflow channel formation on Mars.

4.4.2 Implications for outflow channel incision on Mars

Competing fluvial and volcanic processes in Maja Valles renders it similar to other Tharsis-related, mid-Amazonian aged volcano-fluvial outflow systems including Mangala Valles (Keske et al., 2014) and the Kasei Valles/Echus Chasma system (Chapman et al., 2010). However, its volcanic features bear morphologic similarity to those found in outflow systems related to the Elysium magmatic system, most notably in Athabasca Valles (Jaeger et al., 2007). Because the channels in Athabasca issue from the same source as the lava flow(s) (Cerberus Fossa), Jaeger et al. (2007) have suggested that erosion by lava in Athabasca may have served an important role in channel incision. However, separate sources of flooding and volcanism, as is the case for Maja Valles, allow for comparison

between the topographic signatures of volcanic and fluvial activity. Our analyses reveal that despite its fluid nature, lava flows in Maja Valles probably did not contribute to channel incision during the Amazonian. This interpretation may be applied to other outflow channels, such as Athabasca Valles, whose source of volcanism and channel incision are spatially indistinguishable. Our findings therefore weaken arguments that outflow channels on Mars may have been incised chiefly by thermomechanical erosion by lava.

That being said, it is probably not a coincidence that the source vents of volcanism in Maja Valles occur along an ESE trend directly in line with Juventae Chasma, a trend that parallels Vallis Marineris. This apparent relationship with regional tectonics shared by the two sources, combined with a similar range of crater retention ages shared between the younger fluvial and younger volcanic surfaces, evidences a profound spatial and temporal relationship between fluvial and volcanic activity at Maja Valles. Volcanic activity may not have directly served as a major agent of erosion in Maja Valles, but it very well may have acted as a subsurface thermal agent that caused melting and catastrophic failure of a cryospheric cap over a pressurized aquifer, resulting in massive discharge of its contents into the surface (e.g., Wilson and Head, 1994). Our observations at Maja Valles support such a model as the mechanism of outburst flooding on Mars and reinforce ideas about how fluvial activity, volcanism, and tectonism relate in the Tharsis system and potentially other magmatic systems on Mars. Moreover, given the apparent link between global volcanism and aqueous activity, it is no wonder fluvial activity has waned over time as volcanism has tapered on this ever-cooling planet.

4.5. Acknowledgments

We thank the MRO HiRISE team for acquiring stereo targets and producing three of the HiRISE DTMs used in this study. We also thank Kelin Whipple and Jim Bell III for their insightful feedback. ALK was funded by the National Science Foundation Graduate Research Fellowship Program (#DGE-1311230).

CHAPTER 5

OBJECT SHARP EDGE DETECTION FOR DISTANCE MEASUREMENT USING BLURRED IMAGES FROM THE THESIS/VIS INSTRUMENTS ON PROX-1

5.1. Introduction

Proximity-1 (Prox-1) is a small satellite mission sponsored by the U.S. Air Force Research Laboratory to deploy the 3U CubeSat containing LightSail 2, a solar sail developed by the Planetary Society (Spencer et al., 2016). Slated to launch into low earth orbit as a secondary payload on the SpaceX Falcon Heavy in 2018, the mission will demonstrate automated trajectory control and navigation by acquiring images of the ejected CubeSat as it recedes from the spacecraft and using them to calculate its position. THESIS/VIS is an imaging suite consisting of two cameras, an 8–12 μm broadband thermal imager (THESIS) and a visible imager (VIS), designed to meet the imaging needs for automated trajectory control during the Prox-1 mission (Fig. 5.1). THESIS uses a 640x512 FLIR Tau 2 microbolometer array coupled with a f/1.6 100 mm Ophir germanium lens, and VIS uses the 1290x960 ICX445 EXview HAD color CCD with a f/1.4 25 mm Fujinon lens (Table 5.1). The inclusion of both a thermal and visible camera provides redundancy to aid orbital determination and ensures that imaging may continue even in shadow. The components were selected based on a number of factors including mass, volume, power, heritage, and interface compatibility.

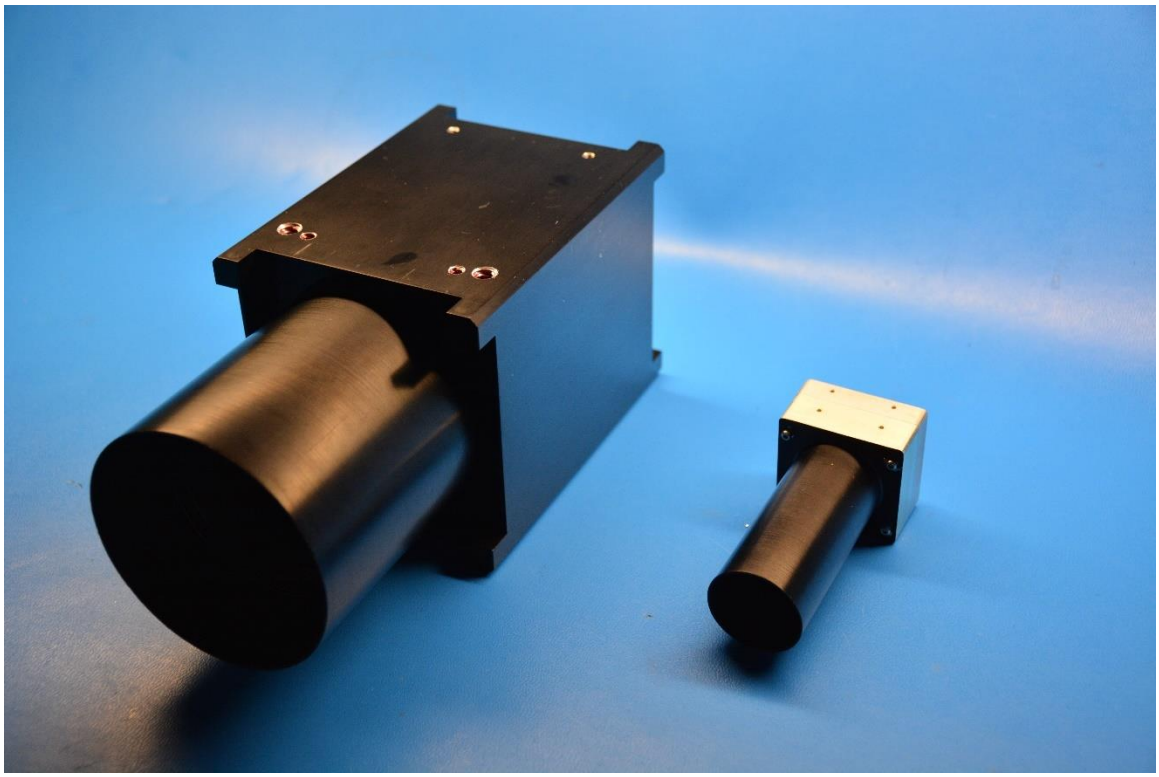

Figure 5.1. THESIS (left) and VIS (right) with custom housing and sun shades.

	Visible Camera (VIS)	**Infrared Camera (THESIS)**
Camera Base	Point Grey Chameleon	FLIR Tau 2
Sensor Type	ICX445 1/3” EXview HAD CCD	Uncooled VOx Microbolometer Array
Array Size	1290 x 960 (1.3 MP)	640 x 512 (0.3 MP)
Pixel Pitch	3.75 µm	17 µm
Optics	Fujinon HF25HA-1B	Ophir 680026
Focal Length	25 mm	100 mm
f/#	1.4	1.6
FOV	10.87° x 8.19°	6.2° x 4.96°
IFOV	0.148 mRad	0.169 mRad
Spectral Range	0.39 µm – 0.75 µm RGB Bayer Pattern	7.5 – 13.5 µm (detector) 8 – 12 µm (optics)

Table 5.1. Specification summary for THESIS/VIS.

Full mission success requires a successful rendezvous with LightSail 2 following ejection. To achieve this, the THESIS/VIS subsystem is required to track the CubeSat while

it is within a distance of 200 meters. This will be done by determining the number of pixels subtended by the CubeSat in acquired images. When the number of pixels N_{px} subtending an object of known width w is determined, its distance d can be calculated using the following formula:

$$d = \frac{wf}{N_{px} l_{px}}$$

where l_{px} is the pixel pitch and f is the focal length of the lens. Since these calculations are to be performed on-board, the images will not need to be downlinked. For this reason, many images can be acquired and processed to minimize uncertainties. However, since the focal distance of the cameras cannot be adjusted during the mission, they will be focused at infinity. This means that the object will appear blurry in images acquired for much of the 0–200-meter range. The goal of this study is to demonstrate that correct pixel counts can be derived from blurry images by incorporating a methodology that I have derived into the image processing algorithm.

5.2. Field testing

To collect data for testing analysis techniques, we conducted a field experiment with both cameras. A 10x10x30-centimeter painted aluminum box mounted on a tripod served as the imaging target for the IR camera, and a test chart containing a 10x30-centimeter rectangle was used for the visible camera (Fig. 5.2, 5.3). We imaged the targets with the respective camera at intervals of 25, 50, 100, 150, and 200 meters. The images collected were collected as raw 16-bit images (.tif and .pgm) using autoexposure. Each image was then cropped to an area containing the target and read into MATLAB for analysis.

Figure 5.2. Field test setup for thermal camera testing: a black painted aluminum box is mounted on the near tripod to represent the CubeSat to be imaged during the mission. THESIS is mounted on the far tripod 25 meters away.

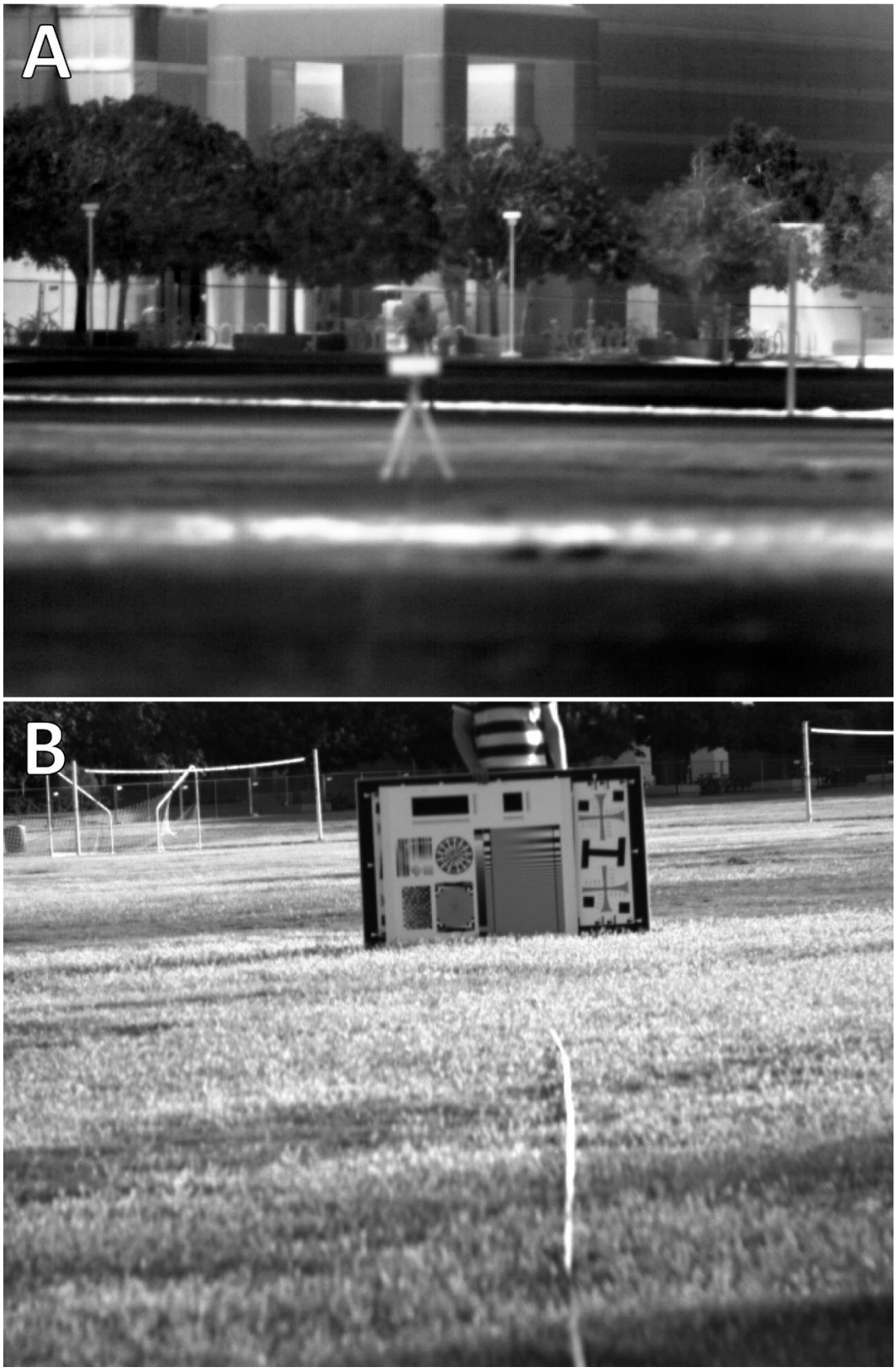

Figure 5.3. Examples of raw test images: A) Thermal image at 50 meters and B) visible monochrome image at 25 meters.

5.3. Analysis

An object may appear blurred in an image on a focal plane array as a result of one or more of a number of causes including motion during exposure of either the imager or the object, improper focusing, or when the system is diffraction-limited. Fundamentally, an object imaged through a circular aperture will appear sharp and is considered resolved in acquired images when the image element size is larger than the Rayleigh criterion for the maximum wavelength emitted by the object incident on the sensor:

$$\theta_R \approx 1.22 \frac{\lambda}{D}$$

where λ is wavelength and D is the diameter of the aperture. In other words, when the diameter of the incident first minimum of the Airy disk is larger than the pixel size, a nontrivial amount of light from the object will bleed into neighboring pixels and produce a false representation of the object imaged, and sharp edges will appear to roll off due to blur (Fig. 5.4). Optical blurring has been studied extensively for microscopy applications, and many approaches have been proposed for deblurring images. As outlined intuitively by Cannell et al. (2006), a sharper image can be deconvolved using the point spread function (PSF) of the optical system as such:

$$F\{i(x,y,z)\} = F\{o(x,y,z)\} \times F\{psf(x,y,z)\}$$

This requires full characterization of the PSF, which can be modeled using knowledge of intimate details of the design of the lens system and advanced ray tracing software such as CODE V. Another approach is by careful laboratory experimentation consisting of careful collection of slices of the PSF (i.e., Airy disks) as the focal plane is adjusted and generating an estimated 3D model (see Cannell et al., 2006 for examples). This is necessary because the Airy disk does not necessarily simply blur with defocusing. As shown by Cannell et al.

(2006), additional structures may arise with defocusing that must be accounted for. In short, deblurring an image is an extremely arduous task not to be taken on lightly.

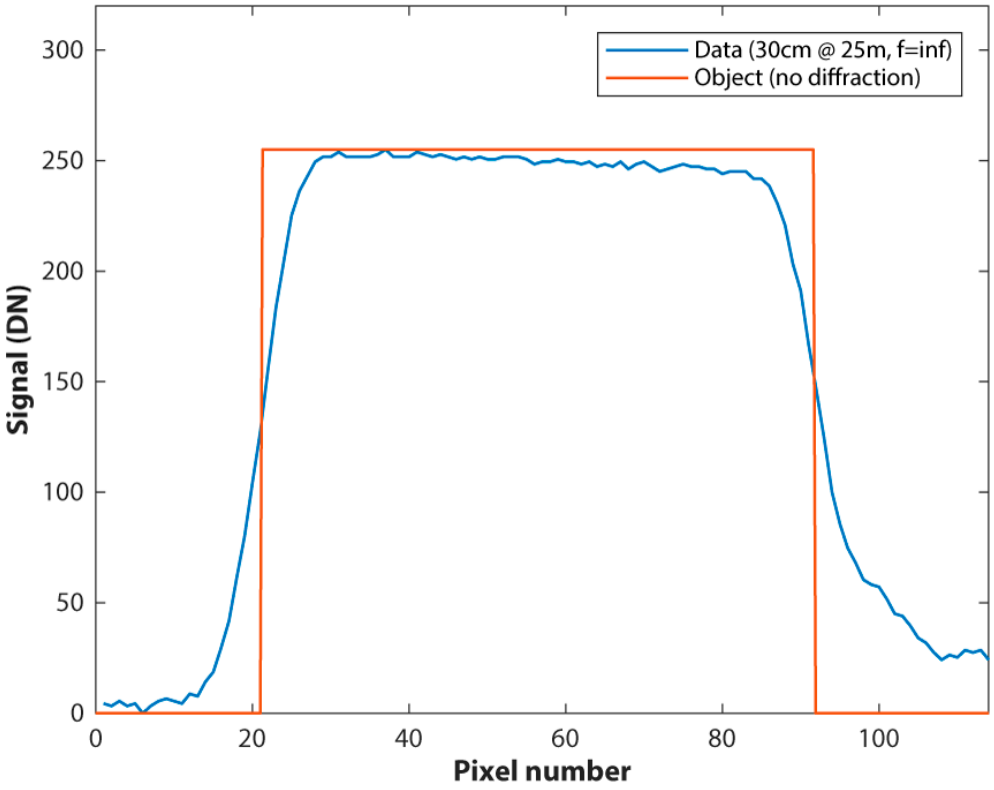

Figure 5.4. Example of signal rolloff in a single line of pixels in one of the thermal images across the 30 centimeters side of the target at a distance of 25 meters (blue) compared to how signal curve would appear if the target were perfectly represented in the image (orange).

5.3.1. Modeling diffraction

THESIS is a diffraction-limited instrument, meaning that even when the lens is perfectly focused on the object, sharp edges will manifest as having some rolloff in the resulting image. To determine to what extend rolloff in our test images was due to diffraction, I created a model that produces a signal curve with diffraction given the instrument specifications (focal length, aperture, pixel pitch, wavelength range) and information about the scene (object temperature, background temperature, object distance,

and object length). This is accomplished by first deriving the energies of 2,250 wavelengths in the wavelength range input (8–12 μm for our study) using the Planck equation:

$$E_\lambda = \frac{2hc^2}{\lambda^5 e^{\frac{hc}{\lambda k_B T}} - 1}$$

where h is Planck's constant, c is the speed of light, k_B is Boltzmann's constant, and T is object temperature. It is then used to calculate the intensity at the center of an Airy disk for each wavelength:

$$I_0 = \frac{\left(\pi\left(\frac{D}{2}\right)^2\right)^2 E_\lambda^2}{2f^2}$$

where f is focal length. Finally, the Airy disk as a function of distance r from the optical axis for each wavelength is calculated:

$$I(r) = I_0\left(\frac{2J_1(x)}{x}\right)^2, \qquad x = \frac{2\pi r D}{\lambda f}$$

where J_1 is a first order Bessell function (Fig. 5.5 top). The disks are then summed to create a compound Airy disk (Fig. 5.5 bottom). This assumes that the target object is a perfect blackbody and that the instrument response function is flat over 8–12 μm with negligible leakage from wavelengths outside of that range. A sharp boundary is simulated by summing the tails of neighboring Airy disks approaching and receding from the boundary. This results in a symmetric curve about the sharp boundary. When applied to our problem and compared to the data, it is clear that diffraction is not the only cause of rolloff in our images (Fig. 5.6). I assume the rest is caused by defocusing. It is possible to model the data by running a gaussian smoothing filter over the Airy disks prior to summing them, but the interval over which smoothing is performed must be adjusted for each data curve individually and varies substantially and nonlinearly. This is likely a result of uncertainties

about how the Airy disks change with defocusing as dictated by the PSF. Another issue is finding a method of automatic background removal that is effective even when object and/or background temperature is uneven without impacting the accuracy of the results. Since the goal of this study is to derive a method that can be implemented automatically on-board the spacecraft, a fitting method is not ideal. Even if I were to fully characterize the PSF for both cameras of sufficient accuracy to produce clear images, the multivariate nature of the problem would result in fits that are non-unique with high uncertainties. Thus, I sought a simpler solution.

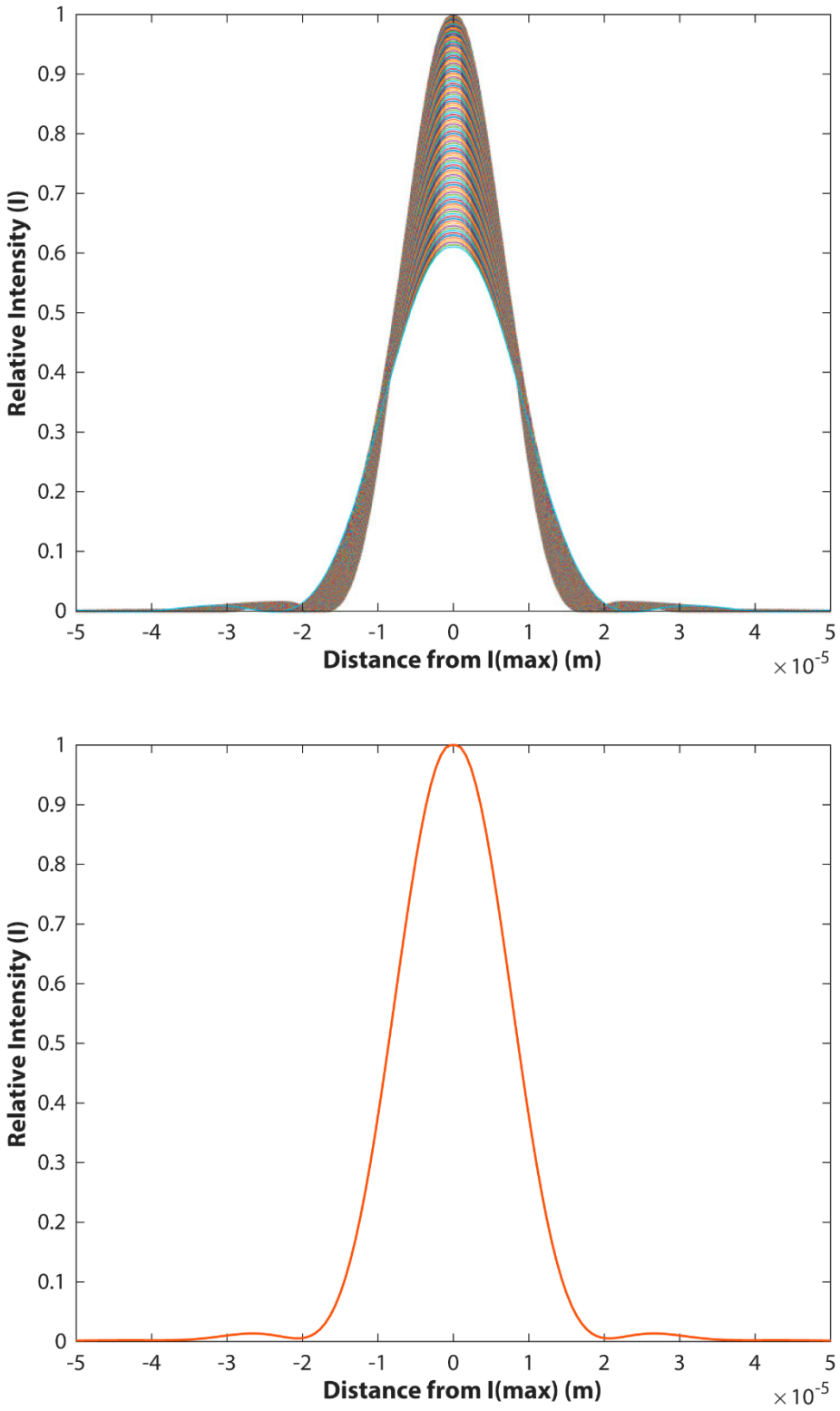

Figure 5.5. Intensity profiles of Airy disks for 2,250 wavelengths between 8–12 μm at 350K, normalized to the maximum intensity (top). These were then summed and renormalized to create a compound Airy disk (bottom).

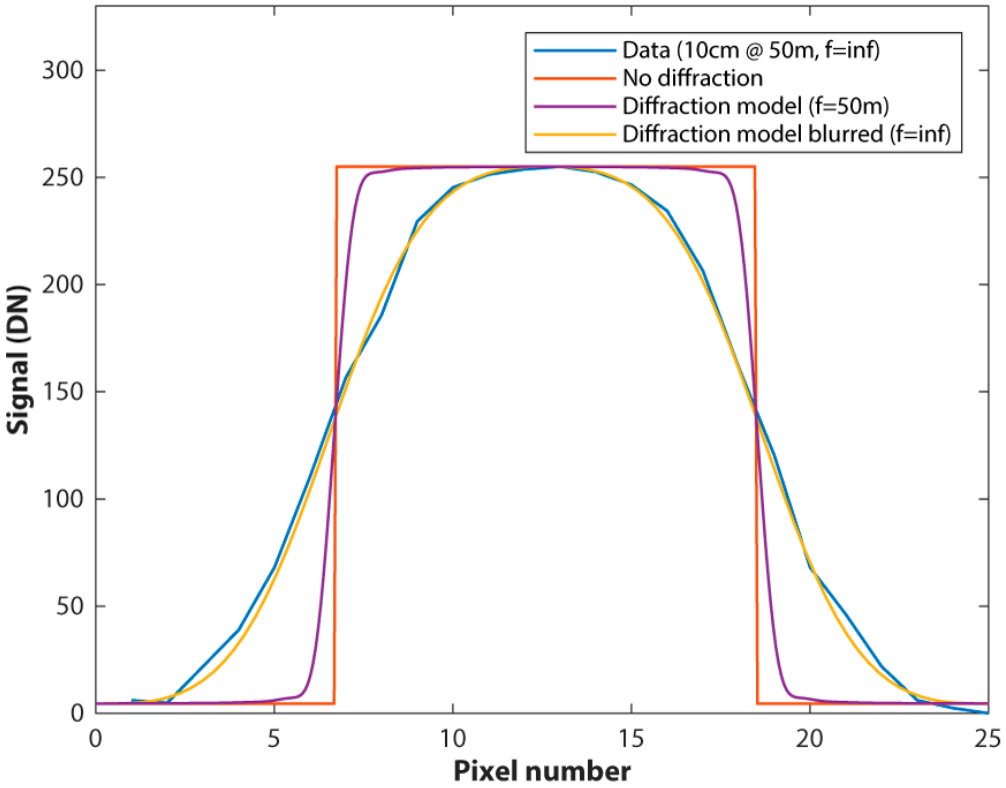

Figure 5.6. Example of actual signal rolloff in our data (thermal at 50 meters, 10-centimeter side) shown in blue, with actual location with perfect optics, no diffraction, and in-focus in orange, modeled in-focus diffraction curve in purple, and a best-fit model curve with blur in yellow.

5.3.2. Edge detection

Because blurring due to defocusing is essentially caused by expansion and structural changes in Airy disks, the degree of blur is effectively the same across the entire image. This means that rolloff should be symmetric about the actual location of the object's sharp edge. Therefore, when the object temperature is even and the background is flat, the actual object width is the full width at half maximum of the signal curve. However, our data show that this is rarely the case (Fig. 5.4, for example), and no single tested background subtraction approach proved to be of sufficient fidelity for automatic use.

Instead, I decided to take advantage of the observation that the point of intersection between rolloff and actual edge location occurs at the point of steepest slope on the rolloff curve. This point can be found by taking the derivative of the curve (Fig. 5.7). There are two ways to use this data: either use the maximum and minimum or approximate the maximum and minimum by finding the average between points on either side of the peak or valley. While the first approach would be the easiest to implement algorithmically, the latter approach produces higher-accuracy results because it is more forgiving of noise in the data. It also produces better results when the actual edge occurs in between two pixels, producing a flatter peak. For these reasons, I have chosen to use the estimation method. A caveat when processing visible data is see-sawing in the signal curves caused by the RGB Bayer pixel pattern (Fig. 5.8). However, this problem was solved by applying a gaussian smoothing filter to the data prior to calculating its derivative. The following data was generated by selecting points by hand, but the method could be carried out programmatically by implementing a subroutine that systematically checks each DN integer value for intersections. If there are exactly two intersections, the pixel numbers are averaged. After completing this task for each DN value, the program may then perform statistics on each cluster of data (for each peak/valley) and return an approximate width. This would have the added advantage of returning an uncertainty value for each individual curve evaluated.

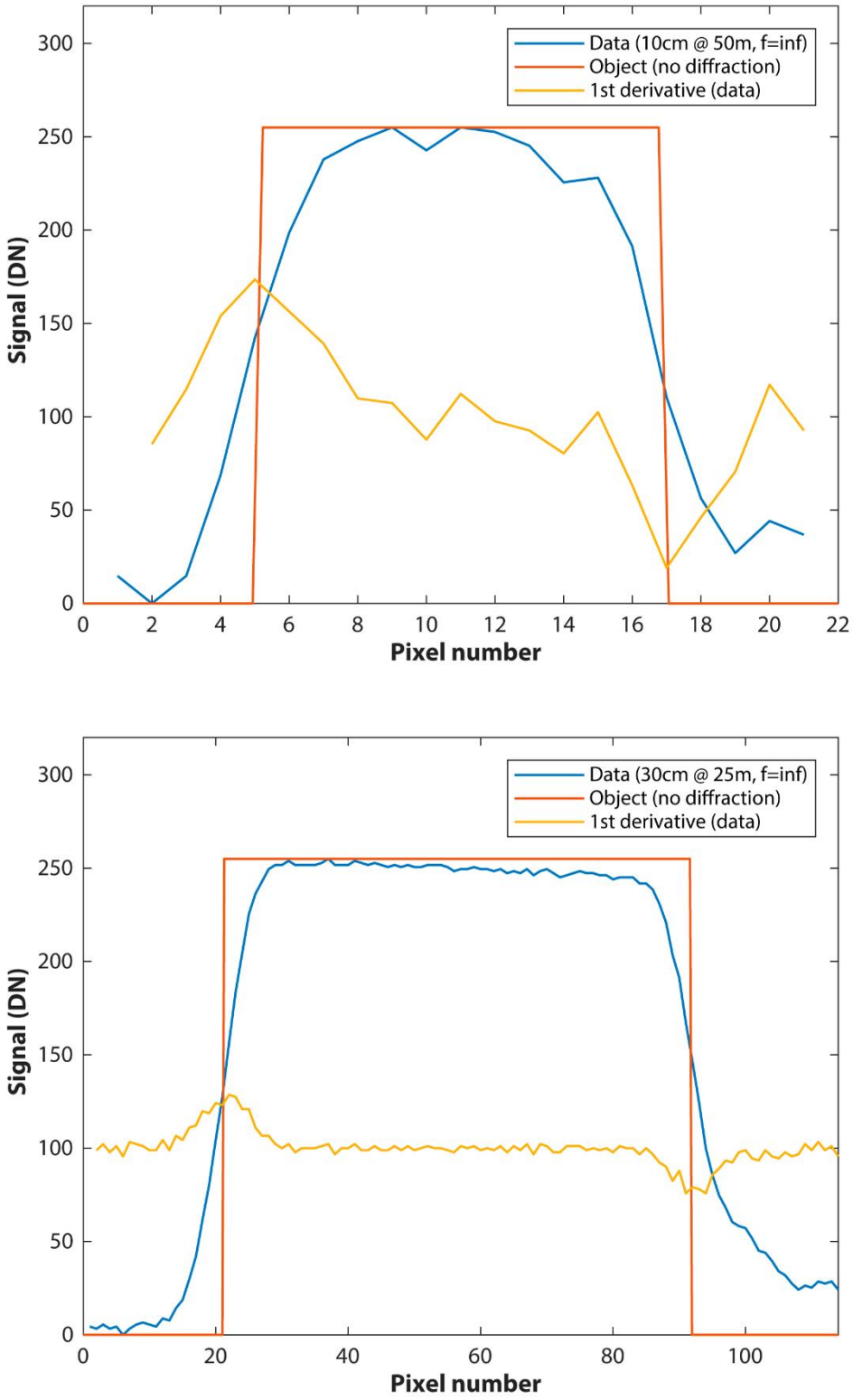

Figure 5.7. Two examples demonstrating how well derivative of the data curve (yellow) correlates with the actual location of the object edge (orange). Both curves are from thermal images.

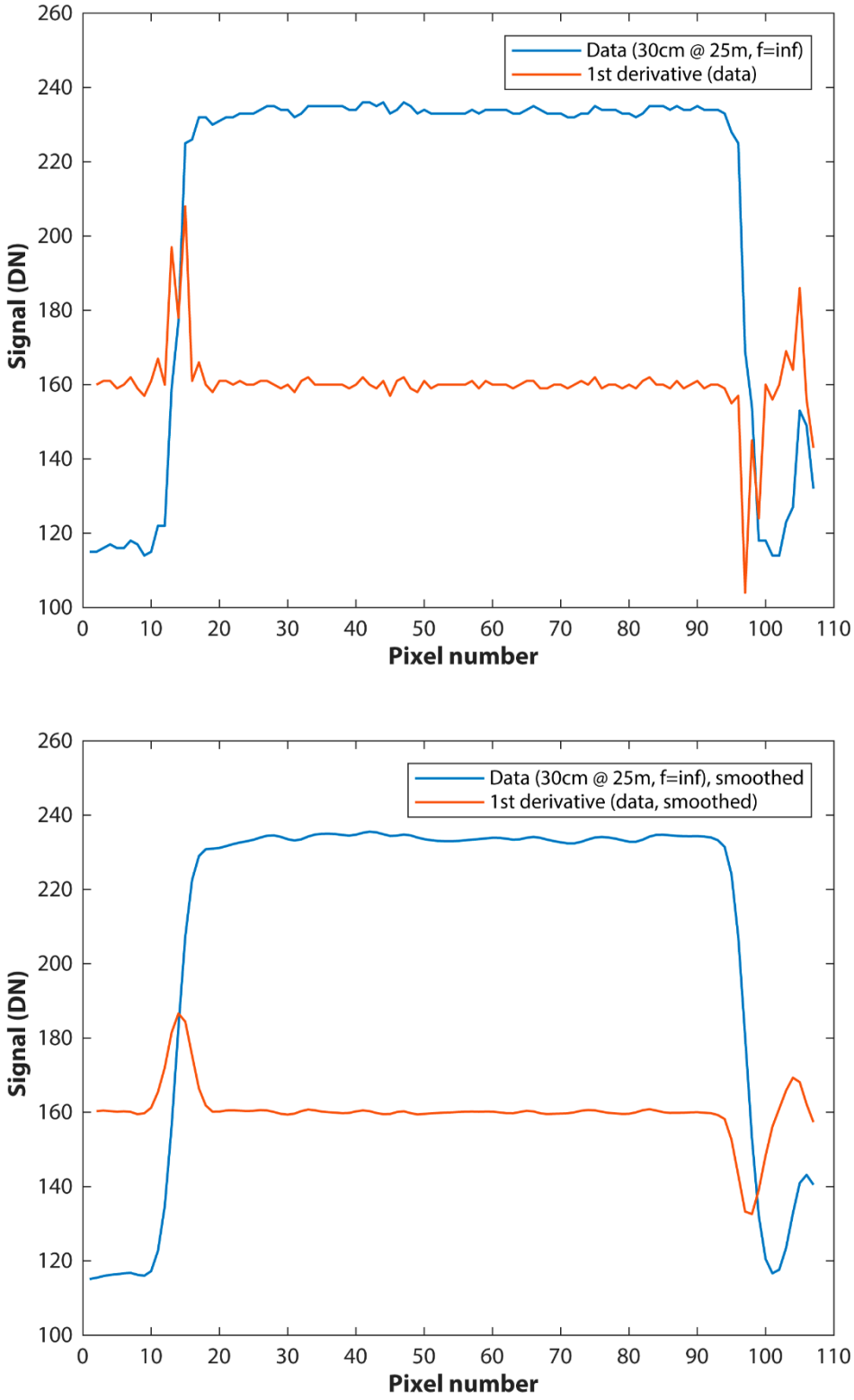

Figure 5.8. Example of the sawtooth pattern in the visible signal curves and their derivatives (top). Smoothing this data with a gaussian smoothing filter fixes the issue (bottom).

Figure 5.9 shows the effectiveness of this method as applied to six images at each distance for each camera. Each point represents the estimated width (in pixels) of individual transects of the 30-centimeter side of the target derived using my method. Shown in dashed lines is the expected width in pixels if the object were in focus without diffraction. A noteworthy drawback of this method, or any method estimating object size in images for that matter, is that saturated values have the potential to return false widths. This is because pixel saturation truncates the true range of values and can thus truncate the top of the signal curve. This will widen the flat top of the signal curve and narrow the rolloff portion, leading to inaccurate width estimates. For this reason, my algorithm rejects signal curves containing a maximum value of 255 DN. Figure 5.10 shows the average and standard deviations of these populations atop the theoretical pixel width curve. It is apparent that the visible data fit more tightly to the expected values. This may be due in part to the smaller degree of diffraction on the images since VIS is not diffraction-limited. A more important influencing factor, however, is most likely the fact that the expected pixel values are integers for all distances except for 150 meters. As discussed previously, when an edge location occurs in between pixel integers, one or both of the peaks tends to be flattened, and the maximum of the curve in the data tends to alternate between the two surrounding pixels for difference transects of the same image. Averaging more transects and from more images allows for greater convergence on the actual pixel width decimal value. But in cases in which object distances happen to result in perfect integer pixel widths, the width value using this method is extremely consistent. This is a flaw in the experiment, as the uncertainties presented cannot be properly extrapolated to non-integer

values. Instead, for the vast majority of object distances, we can expect higher uncertainties.

Figure 5.11 shows the distances corresponding to the averages and standard deviations of estimated widths from Figure 5.9. The red asterisk shows the actual distance of the analog target. For THESIS, the centers of the errorbars match up well with the actual distance for 25, 50, 100, and 150 meters. While the 200-meter estimate is within one standard deviation of the actual value, its center deviates noticeably at 195.5 meters. It is not surprising that accuracy decreases with distance, as the object is smaller in the image and so there are fewer transects available per image for analysis. This is also why uncertainties increase with distance. The visible data predict distances much more accurately, though again this is in part due to the fact that the predicted pixel widths are round integer values for all distances except for 150 meters. Indeed, we can see that the standard deviation of the 150-meter point is noticeably larger than the 200-meter point.

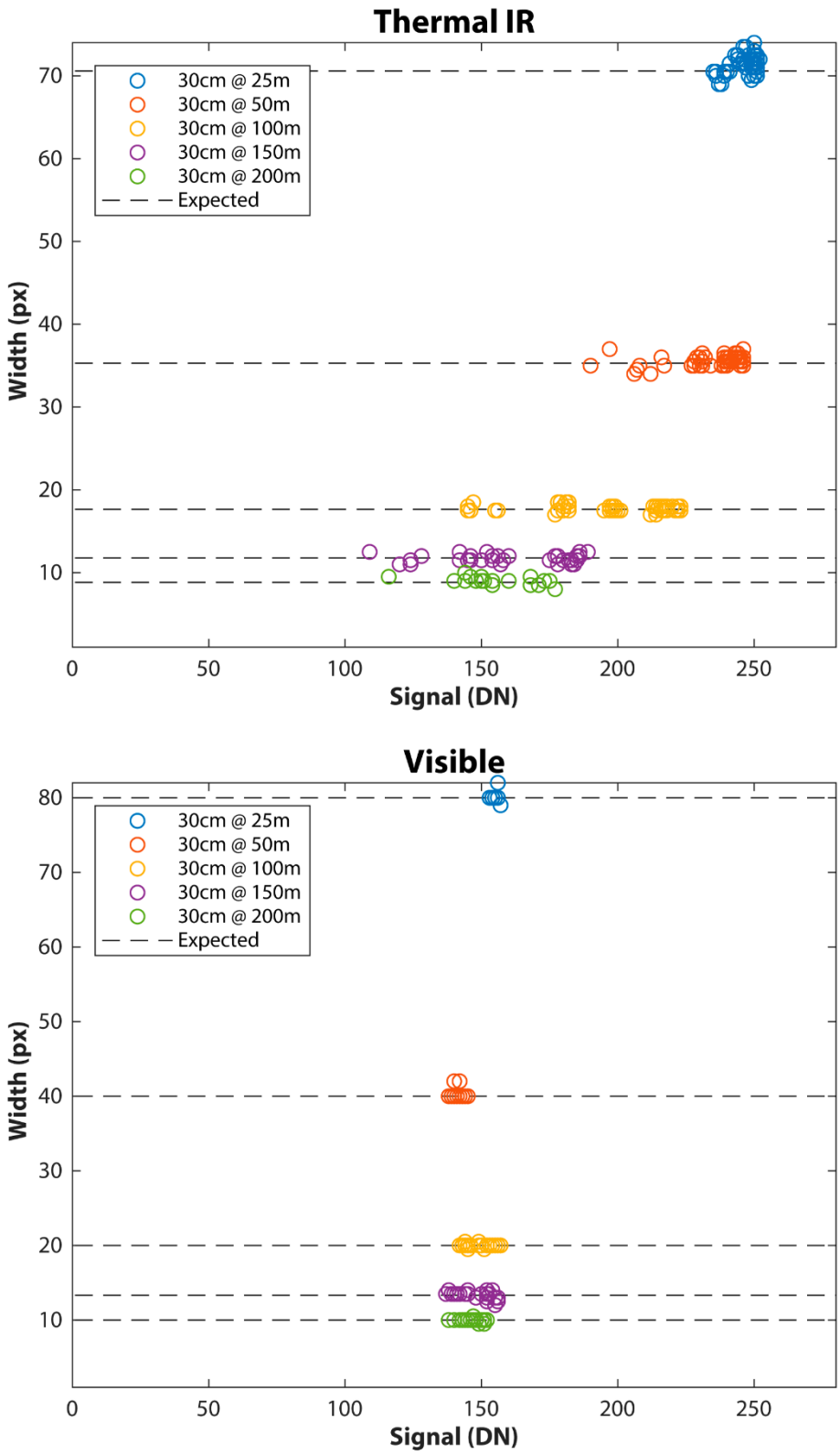

Figure 5.9. The results of applying my method on the field data. Each point is a width result in pixels of a single transect on the 30-centimeter side of the target, which overlie a dotted line showing the theoretical pixel width.

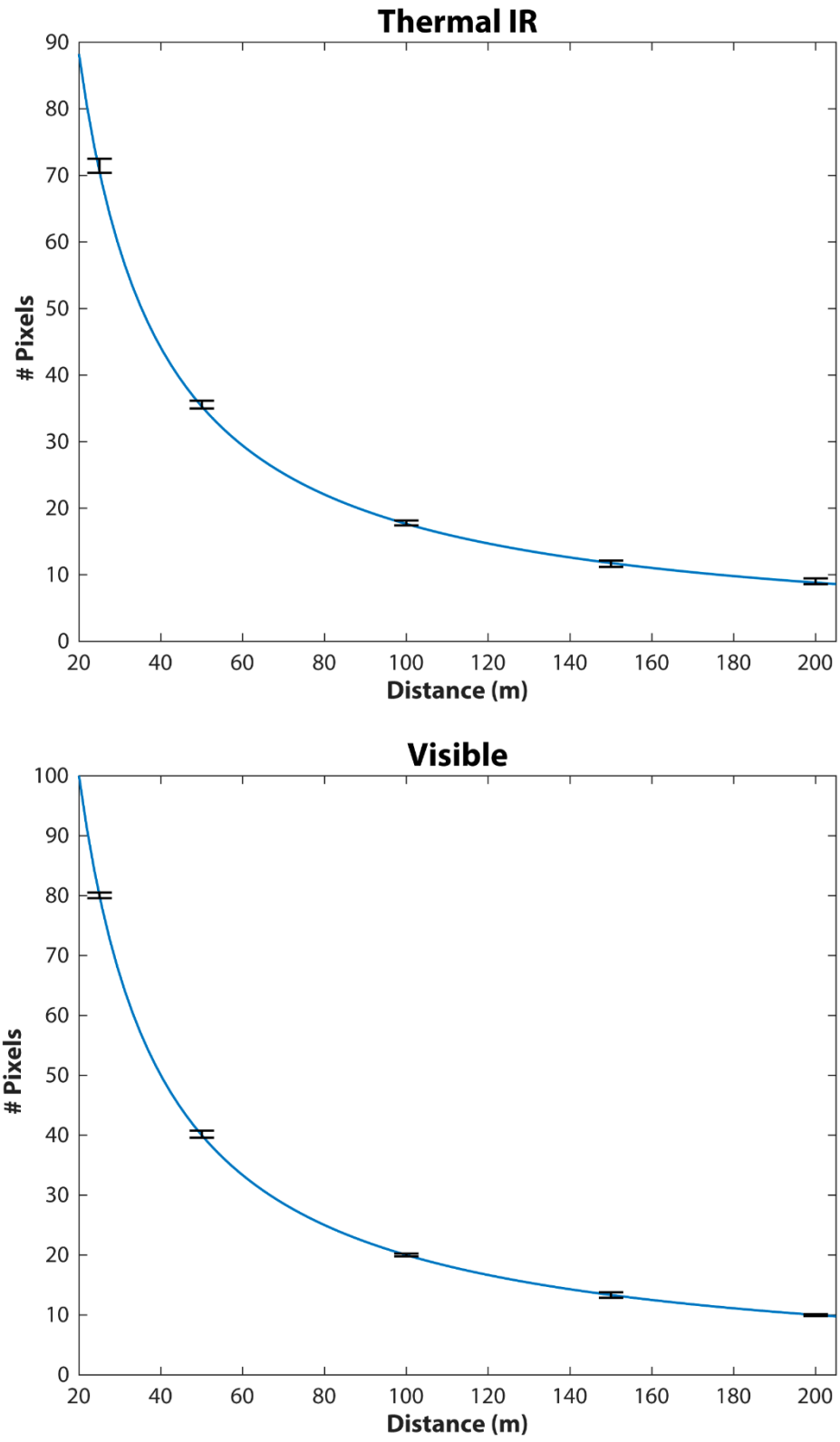

Figure 5.10. Averages and standard deviations of estimated object width in pixels for each distance tested. Shown in blue is the true width in pixels with respect to object distance.

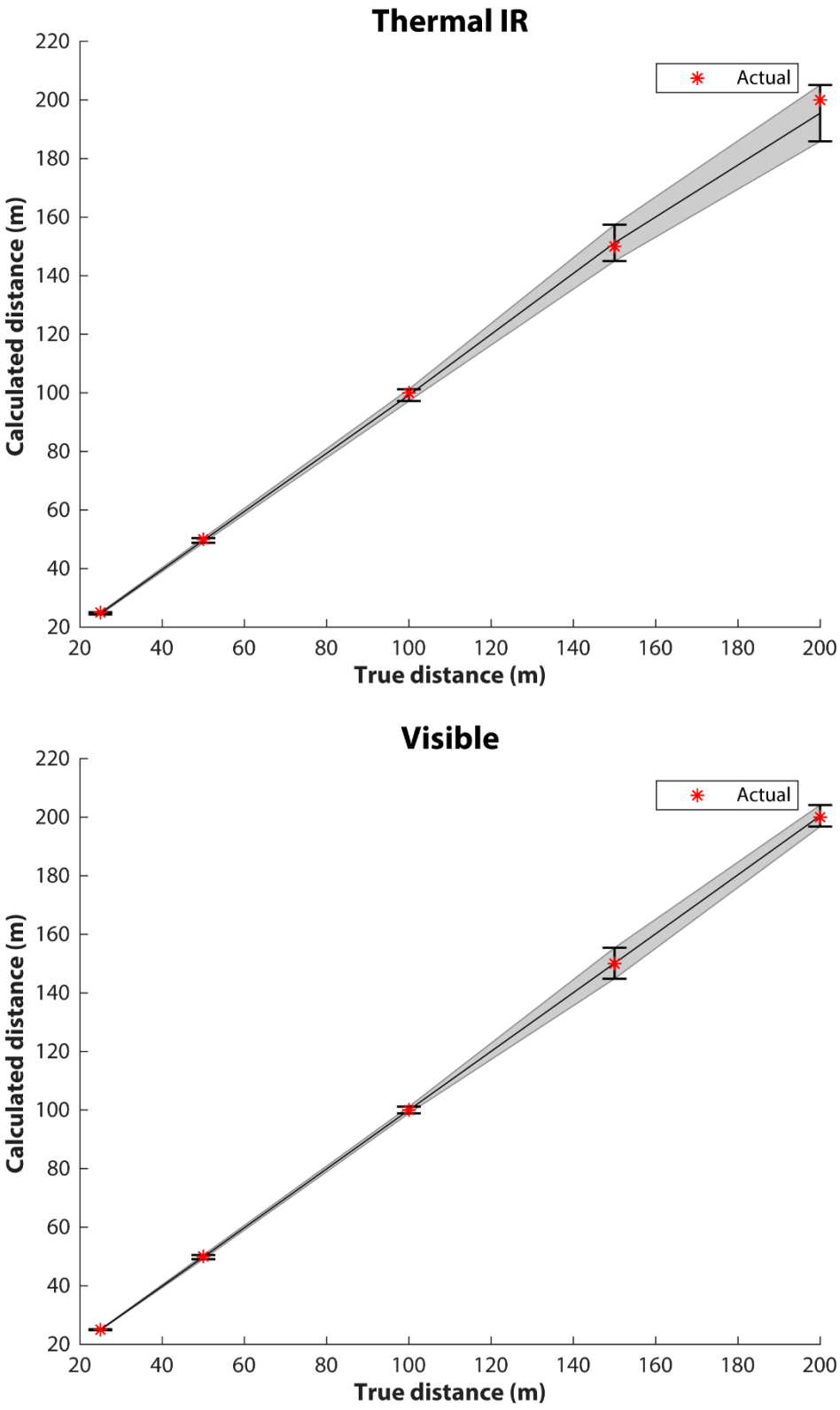

Figure 5.11. Plot showing the result of conversion of the averages and standard deviations of estimated pixel widths to distance estimates. The red asterisk shows the true distance of the object in the image.

5.4. Conclusion

My data show that even though THESIS is diffraction-limited and the CubeSat will be out-of-focus for both THESIS and VIS during the mission, distances can nevertheless be derived from their images within 5 meters using the derivative of the signal curve for each line of pixels subtending it. The slow recession velocity of the CubeSat from the spacecraft will allow for the acquirement of nearly limitless images for analysis, which will greatly improve the distance estimates by this method. The redundancy of the thermal and visible cameras will also serve as mutual verification of the estimate of object distance. This method is simple enough that incorporating it into the image processing algorithm aboard the spacecraft will not utilize much more processing power while still allowing us to meet the measurement requirement. A future version of this test would use distances that are not multiples of five in order to determine more realistic uncertainty values for the visible camera.

5.5. Acknowledgments

I would like to extend my gratitude to Michael Veto for his hard work on the THESIS/VIS subsystem, for helping me with data collection, and for allowing me the privilege of contributing to the Prox-1 project.

CHAPTER 6

SUMMARY

The importance of understanding the roles played by volcanism and aqueous activity in the solar system cannot be overstated. One of the primary goals of planetary science is to understand how fundamental resurfacing processes combine to produce the diverse set of environments we observe today. The work outlined in this dissertation demonstrates ways in which key morphological observations shed light on the physical processes that operated on planetary surfaces in the distant past.

Chapter 2: The Morphometry of Lunar Localized Pyroclastic Deposits

Localized pyroclastic deposits (LPDs) are low-albedo accumulates of pyroclastic material with distinct positive topographic signatures that are found dominantly along highland mare boundaries. Previous workers hypothesized that LPDs represent products of a lunar equivalent of Vulcanian-style eruptions, based in part on the observation that some of the deposits in Alphonsus Crater have large vent volumes in comparison with their deposit volumes, indicating a low proportion of juvenile material in the deposits. The objective of this study is to determine how the proportion of juvenile material, as calculated using deposit and vent volumes, varies among LPDs in Alphonsus Crater and elsewhere on the Moon using contemporary data and methods. We used digital terrain models (DTMs) derived from Lunar Reconnaissance Orbiter Camera Narrow Angle Camera (LROC NAC) observations to create models of pre-eruption surfaces for 23 LPDs from eleven sites and subtracted them from the NAC DTMS to calculate the deposit and vent

volumes. Results show that LPDs have a wide range of juvenile proportions, many of which are more juvenile-rich than previously thought. Additionally, there is a positive relationship between juvenile material proportion and deposit volume and thickness, and a positive relationship between juvenile volume and dispersal area. LPDs also bear a broad range of thinning profiles which span a range of multiple eruption types on Earth. These findings, along with previous studies employing spectroscopic analysis of these deposits, indicate there is greater diversity among LPDs in composition and morphometry than previously understood, and that a simple Vulcanian eruption model may apply only to the deposits containing the least amount of juvenile material, with all others perhaps requiring a combination of multiple eruptive mechanisms. Furthermore, dynamic model results suggest that the most wide-spread lunar deposits in this study formed by magma containing 2000–5000 ppm of dissolved volatiles, consistent with recent estimates via melt-inclusion analysis, but counter to long-held ideas that the Moon was largely degassed during its formation.

Chapter 3: Episodes of Fluvial and Volcanic Activity in Mangala Valles, Mars

A new mapping-based study of the 900-km-long Mangala Valles outflow system was motivated by the availability of new high-resolution images and continued debates about the roles of water and lava in outflow channels on Mars. This study uses photogeologic analysis, geomorphic surface mapping, cratering statistics, and relative stratigraphy. Results show that Mangala Valles underwent at least two episodes of fluvial activity and at least three episodes of volcanic activity during the Late Amazonian. The occurrence of scoured bedrock at the base of the mapped stratigraphy, in addition to

evidence provided by crater retention ages, suggests that fluvial activity preceded the deposition of two of the volcanic units. Crater counts performed at 30 locations throughout the area have allowed us to construct the following timeline: (1) formation of Noachian Highlands and possible initial flooding event(s) before ~1 Ga, (2) emplacement of Tharsis lava flows in the valley from ~700–1000 Ma, (3) a megaflooding event at ~700–800 Ma sourced from Mangala Fossa, (4) valley fill by a sequence of lava flows sourced at Mangala Fossa ~400–500 Ma, (5) another megaflooding event at ~400 Ma, (6) a final phase of volcanism sourced from Mangala Fossa ~300–350 Ma, and (7) emplacement of aeolian sedimentary deposits in the northern portion of the valley ~300 Ma. These results are consistent with alternating episodes of aqueous flooding and volcanism in the valles. This pattern of geologic activity is similar to that of other outflow systems, such as Kasei Valles, suggesting that there is a recurring, and perhaps coupled, nature of these processes on Mars.

Chapter 4: Maja Valles, Mars: A Multi-Source Fluvio-Volcanic Outflow Channel System

It has long been hypothesized that martian outflow channels were formed by catastrophic flooding events, yet many of these channels exhibit lava flow features issuing from the same source as the eroded channels. This relationship has led some authors to suggest that lava may have served as the sole agent of erosion in all martian outflow channels. To address this debate, this study uses cratering statistics paired with stratigraphic relations as determined from surface morphologies to better understand the roles played by fluvial and volcanic processes in the circum-Chryse outflow channel, Maja Valles, during the Amazonian. Results show that while the Maja region hosts a suite of standard fluvial landforms, much of the channel is thinly draped in relatively young lava

flows sourced from Lunae Planum to the west. This sets Maja apart from the other circum-Chryse outflow channels and renders it more analogous to the outflow systems on the flanks of the Elysium volcanic province, which are coated with pristine lava flows. In contrast to the Elysium outflow channels, the source of eroded channels in Maja Valles, Juventae Chasma, is not the source of the lava flows observed in the valles, which instead issue from a fissure/pit chain located in south Lunae Planum to the west. The failure of these lava flows to generate any major channels along their path suggests that the channels of Maja Valles were generated by a separate mechanism, namely fluvial erosion. Crater counting results indicate that the region underwent at least two distinct fluvial episodes at ~1.6 Ga and ~0.9 Ga, the more recent of which occurred within the timeframe of the most recent volcanic episode. This temporal relationship suggests that, despite having separate sources producing morphologically distinctive features, the volcanic and fluvial activity likely share a common thermal driver. The implications of these findings can be used as evidence that other martian outflow channels exhibiting evidence of volcanism and channel erosion from a single source, such as Mangala and Kasei Valles, underwent episodes of both fluvial and volcanic activity.

Chapter 5: Object Sharp Edge Detection for Distance Measurement Using Blurred Images from the THESIS/VIS Instruments on Prox-1

THESIS/VIS is a pair of cameras aboard Prox-1, a low earth orbit mission that will deploy the Planetary Society's Light Sail 2 CubeSat. The primary objective of the THESIS/VIS subsystem, which consists of an 8–12 μm thermal infrared imager and an RGB visible imager, is to image both ejection and rendezvous with the 3U CubeSat with

sufficient resolution to determine the distance its distance up to 200 meters for use in Prox-1's on-board automated trajectory control algorithm. Since the cameras are locked to infinity focus, I derived a method that determines the width of the object in pixels despite image blur using a sharp edge detection method. With the use of six images, my method can determine the distance of the object within 5 meters of accuracy at 200 meters. With incorporation of my method into the onboard image processing algorithm, therefore, THESIS/VIS will be capable of meeting the requirements that will facilitate mission success.

REFERENCES

Alfano, F., Bonadonna, C., Volentik, A. C. M., Connor, C. B., Watt, S. F. L., Pyle, D. M., and Connor, L. J. (2011). Tephra stratigraphy and eruptive volume of the May 2008 Chaitén eruption, Chile. *Bulletin of Volcanology*, *73*, 613–630. https://doi.org/10.1007/s00445-010-0428-x

Allen, C. C. (2015). Taurus Littrow Pyroclastic Deposit: High-Yield Feedstock For Lunar Oxygen. *Proceedings of the 46th Lunar and Planetary Science Conference*, 1140.

Allen, C. C., Donaldson-Hanna, K. L., Pieters, C. M., Moriarty, D. P., Greenhagen, B. T., Bennett, K. A., Kramer, G. Y., and Paige, D. A. (2013). Pyroclastic Deposits in Floor-Fractured Craters – a Unique Style of Lunar Basaltic Volcanism? *Proceedings of the 44th Lunar and Planetary Science Conference*, 1220.

Anderson, R. C., Dohm, J. M., Golombek, M. P., Albert, F. C., Franklin, B. J., Tanaka, K. L., Lias, J., and Peer, B. (2001). Primary centers and secondary concentrations of tectonic activity through time in the western hemisphere of Mars. *Journal of Geophysical Research: Planets*, *106*(E9), 20563–20585. https://doi.org/10.1029/2000JE001278

Arvidson, R., Drozd, R. J., Hohenberg, C. M., Morgan, C. J., and Poupeau, G. (1975). Horizontal Transport of the Regolith, Modification of Features, and Erosion Rates on the Lunar Surface. *The Moon*, *13*, 67–79.

Baker, V. R. (1973). Erosional forms and processes for the catastrophic Pleistocene Missoula floods in eastern Washington. In M. Morisawa (Ed.), *Fluvial Geomorphology* (pp. 123–148). London: Allen & Unwin.

Baker, V. R. (1978). The Spokane Flood controversy and the Martian outflow channels. *Science*, *202*(4374), 1249–1256. https://doi.org/10.1126/science.202.4374.1249

Baker, V. R., Hamilton, C. W., Burr, D. M., Gulick, V. C., Komatsu, G., Luo, W., Rice, J. W., and Rodríguez, J. A. P. (2015). Fluvial geomorphology on Earth-like planetary surfaces: A review. *Geomorphology*, *245*, 149–182. https://doi.org/10.1016/j.geomorph.2015.05.002

Baker, V. R. and Kochel, R. C. (1979). Martian channel morphology: Maja and Kasei valles. *Journal of Geophysical Research: Solid Earth*, *84*(B14), 7961–7983. https://doi.org/10.1029/JB084iB14p07961

Baker, V. R., Komatsu, G., Parker, T. J., Gulick, V. C., Kargel, J. S., and Lewis, J. S. (1992). Channels and valleys on Venus - Preliminary analysis of Magellan data. *Journal of Geophysical Research: Planets*, *97*(E8), 13421–13444. https://doi.org/10.1029/92JE00927

Baker, V. R. and Milton, D. J. (1974). Erosion by Catastrophic Floods on Mars and Earth. *Icarus*, *23*, 27–41. https://doi.org/10.1016/0019-1035(74)90101-8

Baker, V. R., Strom, R. G., Gulick, V. C., and Kargel, J. S. (1991). Ancient oceans, ice sheets and the hydrological cycle on Mars. *Nature*, *352*, 589–594. https://doi.org/10.1038/352589a0

Bargery, A. S. and Wilson, L. (2011). Erosive flood events on the surface of Mars: Application to Mangala and Athabasca Valles. *Icarus*, *212*(2), 520–540. https://doi.org/10.1016/j.icarus.2011.01.001

Barker, M. K., Mazarico, E. M., Neumann, G. A., Zuber, M. T., Haruyama, J., and Smith, D. E. (2016). A new lunar digital elevation model from the Lunar Orbiter Laser Altimeter and SELENE Terrain Camera. *Icarus*, *273*, 346–355. https://doi.org/10.1016/j.icarus.2015.07.039

Basilevsky, A. T., Neukum, G., Werner, S. C., Dumke, A., van Gasselt, S., Kneissl, T., Zuschneid, W., Rommel, D., Wendt, L., Chapman, M. G., Head, J. W., and Greeley, R. (2009). Episodes of floods in Mangala Valles, Mars, from the analysis of HRSC, MOC and THEMIS images. *Planetary and Space Science*, *57*(8–9), 917–943. https://doi.org/10.1016/j.pss.2008.07.023

Bennett, K. A., Horgan, B. H. N., Gaddis, L. R., Greenhagen, B. T., Allen, C. C., Hayne, P. O., Bell, J. F., and Paige, D. A. (2016). Complex Explosive Volcanic Activity on the Moon Within Oppenheimer Crater. *Icarus*, *273*, 296–314. https://doi.org/10.1016/j.icarus.2016.02.007

Besse, S., Sunshine, J. M., and Gaddis, L. R. (2014). Volcanic glass signatures in spectroscopic survey of newly proposed lunar pyroclastic deposits. *Journal of Geophysical Research: Planets*, *119*(2), 355–372. https://doi.org/10.1002/2013JE004537

Bonadonna, C. and Costa, A. (2009). Modeling tephra sedimentation from volcanic plumes. In R. Lopes (Ed.), *Modeling Volcanic Processes: The Physics and Mathematics of Volcanism* (pp. 173–202). Cambridge: Cambridge University Press. https://doi.org/10.1017/CBO9781139021562.009

Bonadonna, C., Mayberry, G. C., Calder, E. S., Sparks, R. S. J., Choux, C., Jackson, P., Lejeune, A. M., Loughlin, S. C., Norton, G. E., Rose, W. I., Ryan, G., and Young, S. R. (2002). Tephra fallout in the eruption of Soufriere Hills Volcano, Montserrat. In T. H. Druitt & B. P. Kokelaar (Eds.), *The Eruption of Soufriere Hills Volcano, Montserrat, from 1995 to 1999* (Vol. 21, pp. 483–516). London: Geological Society, Memoirs.

Boyd, A. K., Nuno, R. G., Robinson, M. S., Denevi, B. W., and Hapke, B. W. (2013). LROC WAC 100 Meter Scale Photometrically Normalized Map of the Moon. *American Geophysical Union Fall Meeting Abstracts*.

Boynton, W. V., Feldman, W. C., Squyres, S. W., Prettyman, T. H., Brückner, J., Evans, L. G., Reedy, R. C., Starr, R. D., Arnold, J. R., Drake, D. M., Englert, P. A. J., Metzger, A. E., Mitrofanov, I., Trombka, J. I., D'Uston, C., Wänke, H., Gasnault, O., Hamara, D. K., Janes, D. M., et al. (2002). Distribution of hydrogen in the near surface of Mars: Evidence for subsurface ice deposits. *Science*, *297*(5578), 81–85. https://doi.org/10.1126/science.1073722

Burr, D. M., Carling, P. A., and Baker, V. R. (2009). *Megaflooding on earth and mars*. *Megaflooding on Earth and Mars*. Cambridge: Cambridge University Press. https://doi.org/10.1017/CBO9780511635632

Byrne, P. K., Klimczak, C., Williams, D. A., Hurwitz, D. M., Solomon, S. C., Head, J. W., Preusker, F., and Oberst, J. (2013). An assemblage of lava flow features on Mercury. *Journal of Geophysical Research: Planets*, *118*(6), 1303–1322. https://doi.org/10.1002/jgre.20052

Cannell, M. B., McMorland, A., and Soeller, C. (2006). Image enhancement by deconvolution. In J. B. Pawley (Ed.), *Handbook of Biological Confocal Microscopy* (3rd ed., pp. 488–500). New York: Springer Science & Business Media, LLC. https://doi.org/10.1007/978-0-387-45524-2_25

Carr, M. H. (1996). Geologic map of the Mare Serenitatis region of the Moon, USGS Misc. Invest. Map I-489. *U.S. Geological Survey, Reston, Va.*

Carr, M. H., Baum, W. A., Briggs, G. A., Masursky, H., Wise, D. U., and Montgomery, D. R. (1972). Imaging experiment: The Viking Mars orbiter. *Icarus*, *16*(1), 17–33. https://doi.org/10.1016/0019-1035(72)90134-0

Carr, M. H. and Head, J. W. (2010). Geologic history of Mars. *Earth and Planetary Science Letters*, *294*(3–4), 185–203. https://doi.org/10.1016/j.epsl.2009.06.042

Chapman, M. G., Gudmundsson, M. T., Russell, A. J., and Hare, T. M. (2003). Possible Juventae Chasma subice volcanic eruptions and Maja Valles ice outburst floods on Mars: Implications of Mars Global Surveyor crater densities, geomorphology, and topography. *Journal of Geophysical Research: Planets*, *108*(E10). https://doi.org/10.1029/2002JE002009

Chapman, M. G. and Kargel, J. S. (1999). Observations at the Mars Pathfinder site: Do they provide "unequivocal" evidence of catastrophic flooding? *Journal of Geophysical Research: Planets*, *104*(E4), 8671–8678. https://doi.org/10.1029/98je02083

Chapman, M. G., Masursky, H., and Dial, A. L. (1989). Geologic Map of Science Study Area 1A, East Mangala Valles Region of Mars, USGS Misc. Invest. Map I-1696. *U.S. Geological Survey, Reston, Va.*

Chapman, M. G., Masursky, H., and Dial, A. L. (1989). Geologic Map of Science Study Area 1A, East Mangala Valles Region of Mars, USGS Misc. Invest. Map I-1962. *U.S. Geological Survey, Reston, Va.*

Chapman, M. G., Masursky, H., and Dial, A. L. (1989). Geologic Map of Science Study Area 1A, East Mangala Valles Region of Mars, USGS Misc. Invest. Map I-1697. *U.S. Geological Survey, Reston, Va.*

Chapman, M. G., Masursky, H., and Dial, A. L. (1991). Geologic Map of Science Study Area 1A, East Mangala Valles Region of Mars, USGS Misc. Invest. Map I-2087. *U.S. Geological Survey, Reston, Va.*

Chapman, M. G., Neukum, G., Dumke, A., Michael, G. G., van Gasselt, S., Kneissl, T., Zuschneid, W., Hauber, E., Ansan, V., Mangold, N., and Masson, P. (2010). Noachian–Hesperian geologic history of the Echus Chasma and Kasei Valles system on Mars: New data and interpretations. *Earth and Planetary Science Letters*, *294*(3–4), 256–271. https://doi.org/10.1016/j.epsl.2009.11.032

Chapman, M. G. and Tanaka, K. L. (1990). Small Valleys and Hydrologic History of the Lower Mangala Valles Region, Mars. *Proceedings of the 20th Lunar and Planetary Science Conference*, 531–539.

Chapman, M. G. and Tanaka, K. L. (1993). Geologic Map of the MTM-05152 and -10152 Quadrangles, Mangala Valles Region of Mars, USGS Misc. Invest. Map I-2294. *U.S. Geological Survey, Reston, Va.*

Christensen, P. R., Jakosky, B. M., Kieffer, H. H., Malin, M. C., Mcsween, H. Y., Nealson, K., Mehall, G. L., Silverman, S. H., Ferry, S., Caplinger, M. A., and Ravine, M. A. (2004). The Thermal Emission Imaging System (THEMIS) for the Mars 2001 Odyssey Mission. *Space Science Reviews*, *110*(1–2), 85–130. https://doi.org/10.1023/B:SPAC.0000

Craddock, R. A. and Greeley, R. (1994). Geologic Map of the MTM-20147 Quadrangle, Mangala Valles Region of Mars, USGS Misc. Invest. Map I-2310. *U.S. Geological Survey, Reston, Va.*

Cutts, J. A. and Blasius, K. R. (1981). Origin of Martian outflow channels: The Eolian hypothesis. *Journal of Geophysical Research*, *86*(B6), 5075–5102. https://doi.org/10.1029/JB086iB06p05075

Edwards, C. S., Nowicki, K. J., Christensen, P. R., Hill, J., Gorelick, N., and Murray, K. (2011). Mosaicking of global planetary image datasets: 1. Techniques and data

processing for Thermal Emission Imaging System (THEMIS) multi-spectral data. *Journal of Geophysical Research: Planets*, *116*(E10). https://doi.org/10.1029/2010JE003755

El-Baz, F. (1972). The cinder field of the Taurus Mountains, part I. *Apollo 15 Preliminary Science Report, NASA SP-289*.

ESRI. (2011). ArcGIS Desktop: Release 10, Redlands, CA: Environmental Systems Research Institute.

Gaddis, L. R., Hawke, B. R., Robinson, M. S., and Coombs, C. R. (2000). Compositional analyses of small lunar pyroclastic deposits using Clementine multispectral data. *Journal of Geophysical Research: Planets*, *105*(E2), 4245–4262. https://doi.org/10.1029/1999JE001070

Gaddis, L. R., Horgan, B. H. N., McBride, M., Bennett, K. A., Stopar, J. D., and Gustafson, J. O. (2016). Alphonsus Crater: Compositional clues to eruption styles of lunar small volcanoes. *Proceedings of the 47th Lunar and Planetary Science Conference*, 2065.

Gaddis, L. R., Pieters, C. M., and Hawke, B. R. (1985). Remote sensing of lunar pyroclastic mantling deposits. *Icarus*, *61*(3), 461–489. https://doi.org/10.1016/0019-1035(85)90136-8

Gaddis, L. R., Staid, M. I., Tyburczy, J. A., Hawke, B. R., and Petro, N. E. (2003). Compositional analyses of lunar pyroclastic deposits. *Icarus*, *161*(2), 262–280. https://doi.org/10.1016/S0019-1035(02)00036-2

Gault, E. D., Horz, F., Brownlee, E. D., and Hartung, B. J. (1974). Mixing of the lunar regolith. *Proceedings of the 5th Lunar and Planetary Science Conference*, 2365–2386.

Ghatan, G. J., Head, J. W., and Wilson, L. (2005). Mangala Valles, Mars: Assessment of Early Stages of Flooding and Downstream Flood Evolution. *Earth, Moon, and Planets*, *96*(1–2), 1–57. https://doi.org/10.1007/s11038-005-9009-y

Gold, T., Bilson, E., and Baron, R. L. (1976). Electrical properties of Apollo 17 rock and soil samples and a summary of the electrical properties of lunar material at 450 MHz frequency. *Proceedings of the 7th Lunar and Planetary Science Conference*, 2593–2603.

Greeley, R. and Spudis, P. D. (1981). Volcanism on Mars. *Reviews of Geophysics*, *19*(1), 13–41. https://doi.org/10.1029/RG019i001p00013

Greeley, R., Theilig, E., Guest, J. E., Carr, M. H., Masursky, H., and Cutts, J. A. (1977). Geology of Chryse Planitia. *Journal Geophysical Research*, *82*(28), 4093–4109. https://doi.org/10.1029/JS082i028p04093

Gustafson, J. O., Bell, J. F., Gaddis, L. R., Hawke, B. R., and Giguere, T. A. (2012). Characterization of previously unidentified lunar pyroclastic deposits using Lunar Reconnaissance Orbiter Camera data. *Journal of Geophysical Research: Planets*, *117*(E12). https://doi.org/10.1029/2011JE003893

Hartmann, W. K. (2005). Martian cratering 8: Isochron refinement and the chronology of Mars. *Icarus*, *174*(2), 294–320. https://doi.org/10.1016/j.icarus.2004.11.023

Haruyama, J., Ohtake, M., Matsunaga, T., Otake, H., Ishihara, Y., Masuda, K., Yokota, Y., and Yamamoto, S. (2014). Data products of SELENE (Kaguya) terrain camera for future lunar missions. *Proceedings of the 45th Lunar and Planetary Science Conference*, 1777.

Hauri, E. H., Weinreich, T., Saal, A. E., Rutherford, M. J., and Van Orman, J. A. (2011). High Pre-Eruptive Water Contents Preserved in Lunar Melt Inclusions. *Science*, *333*(6039), 213–215. https://doi.org/10.1126/science.1204626

Hawke, B. R., Coombs, C. R., and Clark, B. (1990). Ilmenite-rich Pyroclastic Deposits: An Ideal Lunar Resource. *Proceedings of the 20th Lunar and Planetary Science Conference*, 249–258.

Hawke, B. R., Coombs, C. R., Gaddis, L. R., Lucey, P. G., and Owensby, P. D. (1989). Remote sensing and geologic studies of localized dark mantle deposits on the moon. *Proceedings of the 19th Lunar and Planetary Science Conference*, 255–268.

Hawke, B. R., Spudis, P. D., and Clark, P. E. (1985). The origin of selected lunar geochemical anomalies: implications for early volcanism and the formation of light plains. *Earth, Moon, and Planets*, *32*(3), 257–273. https://doi.org/10.1007/BF00054216

Head, J. W. (1974). Lunar dark-mantle deposits: Possible clues to the distribution of early mare deposits. *Geochimica et Cosmochimica Acta*, *1*(1974), 207–222.

Head, J. W. (1976). Lunar volcanism in space and time. *Reviews of Geophysics and Space Physics*, *14*(2), 265–300. https://doi.org/10.1029/RG014i002p00265

Head, J. W. (2004). Glacial deposits on the rim of a Hesperian-Amazonian outflow channel source trough: Mangala Valles, Mars. *Geophysical Research Letters*, *31*(10), L10701. https://doi.org/10.1029/2004GL020294

Head, J. W. and Wilson, L. (1979). Alphonsus-type dark-halo craters: Morphology, morphometry and eruption conditions. *Proceedings of the 10th Lunar and Planetary Science Conference*, 2861–2897.

Head, J. W. and Wilson, L. (2017). Generation, ascent and eruption of magma on the Moon: New insights into source depths, magma supply, intrusions and effusive/explosive

eruptions (Part 2: Predicted emplacement processes and observations). *Icarus*, *283*(2017), 176–223. https://doi.org/10.1016/j.icarus.2016.05.031

Head, J. W., Wilson, L., and Mitchell, K. L. (2003). Generation of recent massive water floods at Cerberus Fossae, Mars by dike emplacement, cryospheric cracking, and confined aquifer groundwater release. *Geophysical Research Letters*, *30*(11), 2–5. https://doi.org/10.1029/2003GL017135

Henriksen, M. R., Manheim, M. R., Burns, K. N., Seymour, P., Speyerer, E. J., Deran, A., Boyd, A. K., Howington-Kraus, E., Rosiek, M. R., Archinal, B. A., and Robinson, M. S. (2017). Extracting accurate and precise topography from LROC narrow angle camera stereo observations. *Icarus*, *283*, 122–137. https://doi.org/10.1016/j.icarus.2016.05.012

Hill, J., Edwards, C. S., and Christensen, P. R. (2014). Mapping the martian surface with THEMIS infrared global mosaics. *Eight International Conference of Mars*, 1141.

Houghton, B. F. and Carey, R. J. (2015). Pyroclastic Fall Deposits. In H. Sigurdsson, B. F. Houghton, S. R. McNutt, H. Rymer, & J. Stix (Eds.), *The Encyclopedia of Volcanoes* (2nd ed., pp. 599–616). San Diego: Academic Press. https://doi.org/10.1016/B978-0-12-385938-9.00034-1

Houghton, B. F. and Gonnermann, H. M. (2008). Basaltic explosive volcanism: Constraints from deposits and models. *Chemie Der Erde - Geochemistry*, *68*(2), 117–140. https://doi.org/10.1016/j.chemer.2008.04.002

Houghton, B. F., Wilson, C. J. N., and Pyle, D. M. (2000). Pyroclastic Fall Deposits. In H. Sigurdsson, B. F. Houghton, S. R. McNutt, H. Rymer, & J. Stix (Eds.), *The Encyclopedia of Volcanoes* (pp. 555–569). San Diego: Academic Press.

Jaeger, W. L., Keszthelyi, L. P., McEwen, A. S., Dundas, C. M., and Russell, P. S. (2007). Athabasca Valles, Mars: a lava-draped channel system. *Science*, *317*(5845), 1709–11. https://doi.org/10.1126/science.1143315

Jaeger, W. L., Keszthelyi, L. P., Skinner, J. A., Milazzo, M. P., McEwen, A. S., Titus, T. N., Rosiek, M. R., Galuszka, D. M., Howington-Kraus, E., and Kirk, R. L. (2010). Emplacement of the youngest flood lava on Mars: A short, turbulent story. *Icarus*, *205*(1), 230–243. https://doi.org/10.1016/j.icarus.2009.09.011

Jaumann, R., Neukum, G., Behnke, T., Duxbury, T. C., Eichentopf, K., Flohrer, J., van Gasselt, S., Giese, B., Gwinner, K., Hauber, E., Hoffmann, H., Hoffmeister, A., Köhler, U., Matz, K. D., Mccord, T. B., Mertens, V., Oberst, J., Pischel, R., Reiss, D., Ress, E., Roatsch, T.,Saiger, P., Scholten, F., Schwarz, G., Stephan, K., Wählisch, M. (2007). The high-resolution stereo camera (HRSC) experiment on Mars Express: Instrument aspects and experiment conduct from interplanetary cruise through the

nominal mission. *Planetary and Space Science*, *55*(7–8), 928–952. https://doi.org/10.1016/j.pss.2006.12.003

Jawin, E. R., Besse, S., Gaddis, L. R., Sunshine, J. M., Head, J. W., and Mazrouei, S. (2015). Examining spectral variations in localized lunar dark mantle deposits. *Journal of Geophysical Research: Planets*, *120*(7), 1310–1331. https://doi.org/10.1002/2014JE004759

Jozwiak, L. M., Head, J. W., Neumann, G. A., and Wilson, L. (2017). Observational constraints on the identification of shallow lunar magmatism: Insights from floor-fractured craters. *Icarus*, *283*, 224–231. https://doi.org/10.1016/j.icarus.2016.04.020

Keske, A. L., Hamilton, C. W., McEwen, A. S., and Daubar, I. J. (2015). Episodes of fluvial and volcanic activity in Mangala Valles, Mars. *Icarus*, *245*, 333–347. https://doi.org/10.1016/j.icarus.2014.09.040

Keszthelyi, L. P., McEwen, A. S., and Thordarson, T. (2000). Terrestrial analogs and thermal models for Martian flood lavas. *Journal of Geophysical Research: Planets*, *105*(E6), 15027–15049. https://doi.org/10.1029/1999JE001191

Keszthelyi, L. P., Thordarson, T., McEwen, A. S., Haack, H., Guilbaud, M.-N., Self, S., and Rossi, M. J. (2004). Icelandic analogs to Martian flood lavas. *Geochemistry, Geophysics, Geosystems*, *5*(11), n/a-n/a. https://doi.org/10.1029/2004GC000758

Kiefer, W. S., MacKe, R. J., Britt, D. T., Irving, A. J., and Consolmagno, G. J. (2012). The density and porosity of lunar rocks. *Geophysical Research Letters*, *39*(7), 1–5. https://doi.org/10.1029/2012GL051319

Komar, P. D. (1979). Comparisons of the hydraulics of water flows in Martian outflow channels with flows of similar scale on earth. *Icarus*, *37*(1), 156–181. https://doi.org/10.1016/0019-1035(79)90123-4

Komar, P. D. (1980). Modes of sediment transport in channelized water flows with ramifications to the erosion of the Martian outflow channels. *Icarus*, *42*(3), 317–329. https://doi.org/10.1016/0019-1035(80)90097-4

Komatsu, G. and Baker, V. R. (2007). Formation of valleys and cataclysmic flood channels on Earth and Mars. In M. G. Chapman (Ed.), *The Geology of Mars: Evidence from Earth-Based Analogs* (pp. 297–321). Cambridge: Cambridge University Press.

Komatsu, G., Baker, V. R., Gulick, V. C., and Parker, T. J. (1993). Venusian Channels and Valleys: Distribution and Volcanological Implications. *Icarus*, *102*(1), 1–25. https://doi.org/10.1006/icar.1993.1029

Komatsu, G., Kargel, J. S., and Baker, V. R. (1992). Canali-type channels on Venus: Some genetic constraints. *Geophysical Research Letters*, *19*(13), 1415–1418. https://doi.org/10.1029/92GL01047

Lamb, M. P., Dietrich, W. E., Aciego, S. M., Depaolo, D. J., and Manga, M. (2008). Formation of Box Canyon, Idaho, by megaflood: implications for seepage erosion on Earth and Mars. *Science*, *320*(5879), 1067–70. https://doi.org/10.1126/science.1156630

Lemoine, F. G., Goossens, S. J., Sabaka, T. J., Nicholas, J. B., Mazarico, E. M., Rowlands, D. D., Loomis, B. D., Chinn, D. S., Neumann, G. A., Smith, D. E., and Zuber, M. T. (2014). GRGM900C: A degree 900 lunar gravity model from GRAIL primary and extended mission data. *Geophysical Research Letters*, *41*(10), 3382–3389. https://doi.org/10.1002/2014GL060027

Leverington, D. W. (2004). Volcanic rilles, streamlined islands, and the origin of outflow channels on Mars. *Journal of Geophysical Research: Planets*, *109*(E10). https://doi.org/10.1029/2004JE002311

Leverington, D. W. (2007). Was the Mangala Valles system incised by volcanic flows? *Journal of Geophysical Research: Planets*, *112*(E11). https://doi.org/10.1029/2007JE002896

Leverington, D. W. (2009). Reconciling channel formation processes with the nature of elevated outflow systems at Ophir and Aurorae Plana, Mars. *Journal of Geophysical Research: Planets*, *114*(10), 1–22. https://doi.org/10.1029/2009JE003398

Leverington, D. W. (2011). A volcanic origin for the outflow channels of Mars: Key evidence and major implications. *Geomorphology*, *132*(3–4), 51–75. https://doi.org/10.1016/j.geomorph.2011.05.022

Levy, J. S. and Head, J. W. (2005). Evidence for remnants of ancient ice-rich deposits: Mangala Valles outflow channel, Mars. *Terra Nova*, *17*(6), 503–509. https://doi.org/10.1111/j.1365-3121.2005.00642.x

Lucchitta, B. K. (1982). Ice sculpture in the Martian outflow channels. *Journal of Geophysical Research*, *87*(B12), 9951–9973. https://doi.org/10.1029/JB087iB12p09951

Lucey, P. G., Taylor, G. J., and Malaret, E. (1995). Abundance and distribution of iron on the Moon. *Science*, *268*(5214), 1150–1153. https://doi.org/10.1126/science.268.5214.1150

Maeno, F., Nagai, M., Nakada, S., Burden, R. E., Engwell, S., Suzuki, Y., and Kaneko, T. (2014). Constraining tephra dispersion and deposition from three subplinian

explosions in 2011 at Shinmoedake volcano, Kyushu, Japan. *Bulletin of Volcanology*, *76*, 1–16. https://doi.org/10.1007/s00445-014-0823-9

Malin, M. C., Bell, J. F., Cantor, B. A., Caplinger, M. A., Calvin, W. M., Clancy, R. T., Edgett, K. S., Edwards, L., Haberle, R. M., James, P. B., Lee, S. W., Ravine, M. A., Thomas, P. C., and Wolff, M. J. (2007). Context Camera Investigation on board the Mars Reconnaissance Orbiter. *Journal of Geophysical Research: Planets*, *112*(E5). https://doi.org/10.1029/2006JE002808

Malin, M. C. and Edgett, K. S. (2001). Mars global surveyor Mars orbiter camera: interplanetary cruise through primary mission. *Journal of Geophysical Research: Planets*, *106*(E10), 23429–23570. https://doi.org/10.1029/2000JE001455

Marra, W. A., Hauber, E., de Jong, S. M., and Kleinhans, M. G. (2015). Pressurized groundwater systems in Lunae and Ophir Plana (Mars): Insights from small-scale morphology and experiments. *GeoResJ*, *8*, 1–13. https://doi.org/10.1016/j.grj.2015.08.001

Mars Channel Working Group (1983). Channels and valleys on Mars. *Geological Society of America Bulletin*, *94*, 1035–1054. https://doi.org/10.1130/0016-7606(1983)94<1035:CAVOM>2.0.CO;2

Mazarico, E. M., Goossens, S. J., Lemoine, F. G., Neumann, G. A., Torrence, M. H., Rowlands, D. D., Smith, D. E., and Zuber, M. T. (2013). Improved Orbit Determination of Lunar Orbiters with Lunar Gravity Fields Obtained by the GRAIL Mission. *Proceedings of the 44th Lunar and Planetary Science Conference*, 2414.

Mazarico, E. M., Rowlands, D. D., Neumann, G. A., Smith, D. E., Torrence, M. H., Lemoine, F. G., and Zuber, M. T. (2012). Orbit determination of the Lunar Reconnaissance Orbiter. *Journal of Geodesy*, *86*(3), 193–207. https://doi.org/10.1007/s00190-011-0509-4

McCauley, J. F., Carr, M. H., Cutts, J. A., Hartmann, W. K., Masursky, H., Milton, D. J., Sharp, R. P., and Wilhelms, D. E. (1972). Preliminary mariner 9 report on the geology of Mars. *Icarus*, *17*, 289–327. https://doi.org/10.1016/0019-1035(72)90003-6

McEwen, A. S., Eliason, E. M., Bergstrom, J. W., Bridges, N. T., Hansen, C. J., Delamere, W. A., Grant, J. A., Gulick, V. C., Herkenhoff, K. E., Keszthelyi, L. P., Kirk, R. L., Mellon, M. T., Squyres, S. W., Thomas, N., and Weitz, C. M. (2007). Mars reconnaissance orbiter's high resolution imaging science experiment (HiRISE). *Journal of Geophysical Research: Planets*, *112*(E5). https://doi.org/10.1029/2005JE002605

McEwen, A. S., Keszthelyi, L. P., and Grant, J. A. (2012). Have there been large, recent water floods on Mars? *Proceedings of the 43rd Lunar and Planetary Science Conference*, 1612.

Melosh, H. J. (1989). *Impact cratering: A geologic process*. New York: Oxford University Press.

Michael, G. G. (2013). Planetary surface dating from crater size-frequency distribution measurements: Multiple resurfacing episodes and differential isochron fitting. *Icarus*, *226*(1), 885–890. https://doi.org/10.1016/j.icarus.2013.07.004

Michael, G. G. and Neukum, G. (2010). Planetary surface dating from crater size-frequency distribution measurements: Partial resurfacing events and statistical age uncertainty. *Earth and Planetary Science Letters*, *294*(3–4), 223–229. https://doi.org/10.1016/j.epsl.2009.12.041

Milton, D. J. (1974). Geologic Map of the Lunae Palus Quadrangle of Mars, USGS Misc. Invest. Map I-894. *U.S. Geological Survey, Reston, Va.*

Mustard, J. F., Cooper, C. D., and Rifkin, M. K. (2001). Evidence for recent climate change on Mars from the identification of youthful near-surface ground ice. *Nature*, *1128*(1971), 411–414. https://doi.org/10.1038/35086515

Neukum, G., Basilevsky, A. T., Kneissl, T., Chapman, M. G., van Gasselt, S., Michael, G. G., Jaumann, R., Hoffmann, H., and Lanz, J. K. (2010). The geologic evolution of Mars: Episodicity of resurfacing events and ages from cratering analysis of image data and correlation with radiometric ages of Martian meteorites. *Earth and Planetary Science Letters*, *294*(3–4), 204–222. https://doi.org/10.1016/j.epsl.2009.09.006

Nozette, S. (1995). The Clementine mission: Past, present, and future. *Acta Astronautica*, *35*(Suppl. 1), S161–S169. https://doi.org/10.1016/0094-5765(94)00181-K

Nummedal, D. A. G. and Priori, D. B. (1981). Generation of Martian Chaos and Channels by Debris Flows. *Icarus*, *45*(1), 77–86. https://doi.org/10.1016/0019-1035(81)90007-5

Paige, D. A., Foote, M. C., Greenhagen, B. T., Schofield, J. T., Calcutt, S., Vasavada, A. R., Preston, D. J., Taylor, F. W., Allen, C. C., Snook, K. J., Jakosky, B. M., Murray, B. C., Soderblom, L. A., Jau, B., Loring, S., Bulharowski, J., Bowles, N. E., Thomas, I. R., Sullivan, M. T., Avis, C., De Jong, E. M., Hartford, W., McCleese, D. J. (2010). The lunar reconnaissance orbiter diviner lunar radiometer experiment. *Space Science Reviews*, *150*(1–4), 125–160. https://doi.org/10.1007/s11214-009-9529-2

Papike, J. J. (1998). Planetary Materials. *Reviews in Mineralogy* (Vol. 36). Chantilly: Mineralogical Society of America.

Pieters, C. M., Boardman, J., Buratti, B., Chatterjee, A., Clark, R., Glavich, T., Green, R., Head, J. W., Isaacson, P., Malaret, E., Mccord, T. B., Mustard, J. F., Petro, N. E., Runyon, C., Staid, M. I., Sunshine, J. M., Taylor, L., Tompkins, S., Varanasi, P.,

White, M. (2009). The Moon Mineralogy Mapper (M3) on Chandrayaan-1. *Current Science*, *96*(4), 500–505. https://doi.org/10.2307/24105459

Pyle, D. M. (1989). The thickness, volume and grainsize of tephra fall deposits. *Bulletin of Volcanology*, *51*, 1–15. https://doi.org/10.1007/BF01086757

Robbins, S. J. and Hynek, B. M. (2012). A new global database of Mars impact craters ≥1 km: 2. Global crater properties and regional variations of the simple-to-complex transition diameter. *Journal of Geophysical Research: Planets*, *117*(E6). https://doi.org/10.1029/2011JE003967

Robinson, M. S., Brylow, S. M., Tschimmel, M., Humm, D., Lawrence, S. J., Thomas, P. C., Denevi, B. W., Bowman-Cisneros, E., Zerr, J., Ravine, M. A., Caplinger, M. A., Ghaemi, F. T., Schaffner, J. A., Malin, M. C., Mahanti, P., Bartels, A., Anderson, J. A., Tran, T. N., Eliason, E. M., McEwen, A. S., Turtle, E., Jolliff, B. L., Hiesinger, H. (2010). Lunar Reconnaissance Orbiter Camera (LROC) Instrument Overview. *Space Science Reviews*, *150*(1), 81–124. https://doi.org/10.1007/s11214-010-9634-2

Romero, J. E., Douillet, G. A., Vargas, S. V., Bustillos, J., Troncoso, L., Díaz Alvarado, J., and Ramón, P. (2017). Dynamics and style transition of a moderate, Vulcanian-driven eruption at Tungurahua (Ecuador) in February 2014: Pyroclastic deposits and hazard considerations. *Solid Earth*, *8*, 697–719. https://doi.org/10.5194/se-8-697-2017

Rotto, S. and Tanaka, K. L. (1995). Geologic/Geomorphic map of the Chryse Planitia region of Mars, USGS Misc. Invest. Map I–2441, scale 1:5000000. *U.S. Geological Survey, Reston, Va.*

Ruff, S. W. and Christensen, P. R. (2002). Bright and dark regions on Mars: Particle size and mineralogical characteristics based on Thermal Emission Spectrometer data. *Journal of Geophysical Research: Planets*, *107*(E12), 5127. https://doi.org/10.1029/2001JE001580

Sato, M. (1976). Oxygen fugacity and other thermochemical parameters of Apollo 17 high-Ti basalts and their implications on the reduction mechanism. *Proceedings of the 7th Lunar and Planetary Science Conference*, 1323–1344.

Schmitt, H. H., Trask, N. J., and Shoemaker, E. M. (1967). Geologic map of the Copernicus quadrangle of the Moon, USGS Misc. Invest. Map I-515. *U.S. Geological Survey, Reston, Va.*

Scott, D. H. and Tanaka, K. L. (1986). Geologic map of the western equatorial region of Mars, USGS Misc. Invest. Map I–1802–A, scale 1:15000000. *U.S. Geological Survey, Reston, Va.*

Sharp, R. P. and Malin, M. C. (1975). Channels on Mars. *Geological Society of America Bulletin*, *86*(50), 593–609. https://doi.org/10.1130/0016-7606(1975)86<593:COM>2.0.CO;2

Skinner, J. A., Hare, T. M., and Tanaka, K. L. (2006). Digital renovation of the Atlas of Mars 1:15,000,000-scale global geologic series maps. *Proceedings of the 37th Lunar and Planetary Science Conference*, 2331.

Smith, D. E., Zuber, M. T., Frey, H. V., Garvin, J. B., Head, J. W., Muhleman, D. O., Pettengill, G. H., Phillips, R. J., Solomon, S. C., Zwally, H. J., Banerdt, W. B., Duxbury, T. C., Golombek, M. P., Lemoine, F. G., Neumann, G. A., Rowlands, D. D., Aharonson, O., Ford, P. G., Ivanov, A. B., Johnson, C. L., McGovern, P. J., Abshire, J. B., Afzal, R. S., Sun, X. (2001). Mars Orbiter Laser Altimeter: Experiment summary after the first year of global mapping of Mars. *Journal of Geophysical Research: Planets*, *106*(E10), 23689–23722. https://doi.org/10.1029/2000JE001364

Smith, D. E., Zuber, M. T., Jackson, G. B., Cavanaugh, J. F., Neumann, G. A., Riris, H., Sun, X., Zellar, R. S., Coltharp, C., Connelly, J., Katz, R. B., Kleyner, I., Liiva, P., Matuszeski, A., Mazarico, E. M., McGarry, J. F., Novo-Gradac, A.-M., Ott, M. N., Peters, C., et al. (2010). The Lunar Orbiter Laser Altimeter Investigation on the Lunar Reconnaissance Orbiter Mission. *Space Science Reviews*, *150*(1), 209–241. https://doi.org/10.1007/s11214-009-9512-y

Smith, P. H., Bell, J. F., Bridges, N. T., Britt, D. T., Gaddis, L. R., Greeley, R., Keller, H. U., Herkenhoff, K. E., Jaumann, R., Johnson, J. R., Kirk, R. L., Lemmon, M., Maki, J. N., Malin, M. C., Murchie, S. L., Oberst, J., Parker, T. J., Reid, R. J., Sablotny, R., Ramos-Izquierdo, L. A., Ramsey, L., Rowlands, D. D., Schmidt, S., Scott, V. S., Shaw, G. B., Smith, J. C., Swinski, J., Torrence, M. H., Unger, G., Yu, A. W., Zagwodzki, T. W. (1997). Results from the Mars Pathfinder camera. *Science*, *278*(5344), 1758–1765. https://doi.org/10.1126/science.278.5344.1758

Spencer, D. A., Chait, S. B., Schulte, P. Z., Okseniuk, K. J., and Veto, M. S. (2016). Prox-1 University-Class Mission to Demonstrate Automated Proximity Operations. *Journal of Spacecraft and Rockets*, *53*(5), 847–863. https://doi.org/10.2514/1.A33526

Taddeucci, J., Edmonds, M., Houghton, B. F., James, M. R., and Vergniolle, S. (2015). Hawaiian and Strombolian Eruptions. In H. Sigurdsson, B. F. Houghton, S. R. McNutt, H. Rymer, & J. Stix (Eds.), *The Encyclopedia of Volcanoes* (2nd ed., pp. 485–503). San Diego: Academic Press. https://doi.org/10.1016/B978-0-12-385938-9.00027-4

Tanaka, K. L. and Chapman, M. G. (1990). The Relation of Catastrophic Flooding of Mangala Valles, Mars, to Faulting of Memnonia Fossae and Tharsis Volcanism. *Journal of Geophysical Research: Solid Earth*, *95*(B9), 14315–14323. https://doi.org/10.1029/JB095iB09p14315

Tanaka, K. L., Robbins, S. J., Fortezzo, C. M., Skinner, J. A., and Hare, T. M. (2014). The digital global geologic map of Mars: Chronostratigraphic ages, topographic and crater morphologic characteristics, and updated resurfacing history. *Planetary and Space Science*, *95*, 11–24. https://doi.org/10.1016/j.pss.2013.03.006

Tanaka, K. L., Skinner, J. A., Dohm, J. M., Irwin, R. P., Kolb, E. J., Fortezzo, C. M., Platz, T., Michael, G. G., and Hare, T. M. (2014). Geologic map of Mars: USGS Sci. Invest. Map 3292, scale 1:20,000,000. *U.S. Geological Survey, Reston, Va.* https://doi.org/10.3133/sim3292

Thankur, P. K., Bhardwaj, A., and Aggarwal, S. P. (2007). Hydrological Parameter Extraction and Analysis of Mangala Valles of Mars. *Seventh International Conference on Mars*, (1353), 3116.

Walker, G. P. L. (1973). Explosive volcanic eruptions - a new classification scheme. *Geologische Rundschau*, *62*(2), 431–446. https://doi.org/10.1007/BF01840108

Walker, G. P. L. (1991). Structure, and origin by injection of lava under surface crust, of tumuli, “lava rises”, “lava-rise pits”, and “lava-inflation clefts” in Hawaii. *Bulletin of Volcanology*, 546–558. https://doi.org/10.1007/BF00298155

Warner, N. H., Gupta, S., Muller, J.-P., Kim, J.-R., and Lin, S.-Y. (2009). A refined chronology of catastrophic outflow events in Ares Vallis, Mars. *Earth and Planetary Science Letters*, *288*(1–2), 58–69. https://doi.org/10.1016/j.epsl.2009.09.008

Wilhelms, D. E. (1972). Geologic Mapping of the Second Planet. *Interagency Report: Astrogeology 55*.

Wilhelms, D. E. and McCauley, J. F. (1971). Geologic map of the near side of the Moon, USGS Misc. Invest. Map I-703. *U.S. Geological Survey, Reston, Va.*

Wilson, L. and Head, J. W. (1994). Mars: Review and Analysis of Volcanic Eruption Theory and Relationships to Observed Landforms. *Reviews of Geophysics*, *32*(3), 221–263. https://doi.org/10.1029/94RG01113

Wilson, L. and Head, J. W. (2002). Tharsis-radial graben systems as the surface manifestation of plume-related dike intrusion complexes: Models and implications. *Journal of Geophysical Research: Planets*, *107*(E8). https://doi.org/10.1029/2001JE001593

Wilson, L. and Head, J. W. (2017). Generation, ascent and eruption of magma on the Moon: New insights into source depths, magma supply, intrusions and effusive/explosive eruptions (Part 1: Theory). *Icarus*, *283*(2017), 146–175. https://doi.org/10.1016/j.icarus.2016.05.031

Wilson, L., Mouginis-Mark, P. J., Tyson, S., Mackown, J., and Garbeil, H. (2009). Fissure eruptions in Tharsis, Mars: Implications for eruption conditions and magma sources. *Journal of Volcanology and Geothermal Research*, *185*, 28–46. https://doi.org/10.1016/j.jvolgeores.2009.03.006

Wilson, L., Scott, E. D., and Head, J. W. (2001). Evidence for episodicity in the magma supply to the large Tharsis volcanoes. *Journal of Geophysical Research: Planets*, *106*(E1), 1423–1433. https://doi.org/10.1029/2000JE001280

Witbeck, N. E., Tanaka, K. L., and Scott, D. H. (1991). The geologic map of the Valles Marineris region, Mars, USGS Misc. Invest. Map I–2010, scale 1:2000000. *U.S. Geological Survey, Reston, Va.*

Zimbelman, J. R., Craddock, R. A., and Greeley, R. (1994). Geologic Map of the MTM-15147 Quadrangle, Mangala Valles Region of Mars, USGS Misc. Invest. Map I-2402. *U.S. Geological Survey, Reston, Va.*

Zimbelman, J. R., Craddock, R. A., Greeley, R., and Kuzmin, R. (1992). Volatile History of Mangala Valles, Mars. *Journal of Geophysical Research: Planets*, *97*(E11), 18309–18317. https://doi.org/10.1029/92JE02054

APPENDIX A

CRATER SIZE FREQUENCY DISTRIBUTIONS FOR MANGALA VALLES

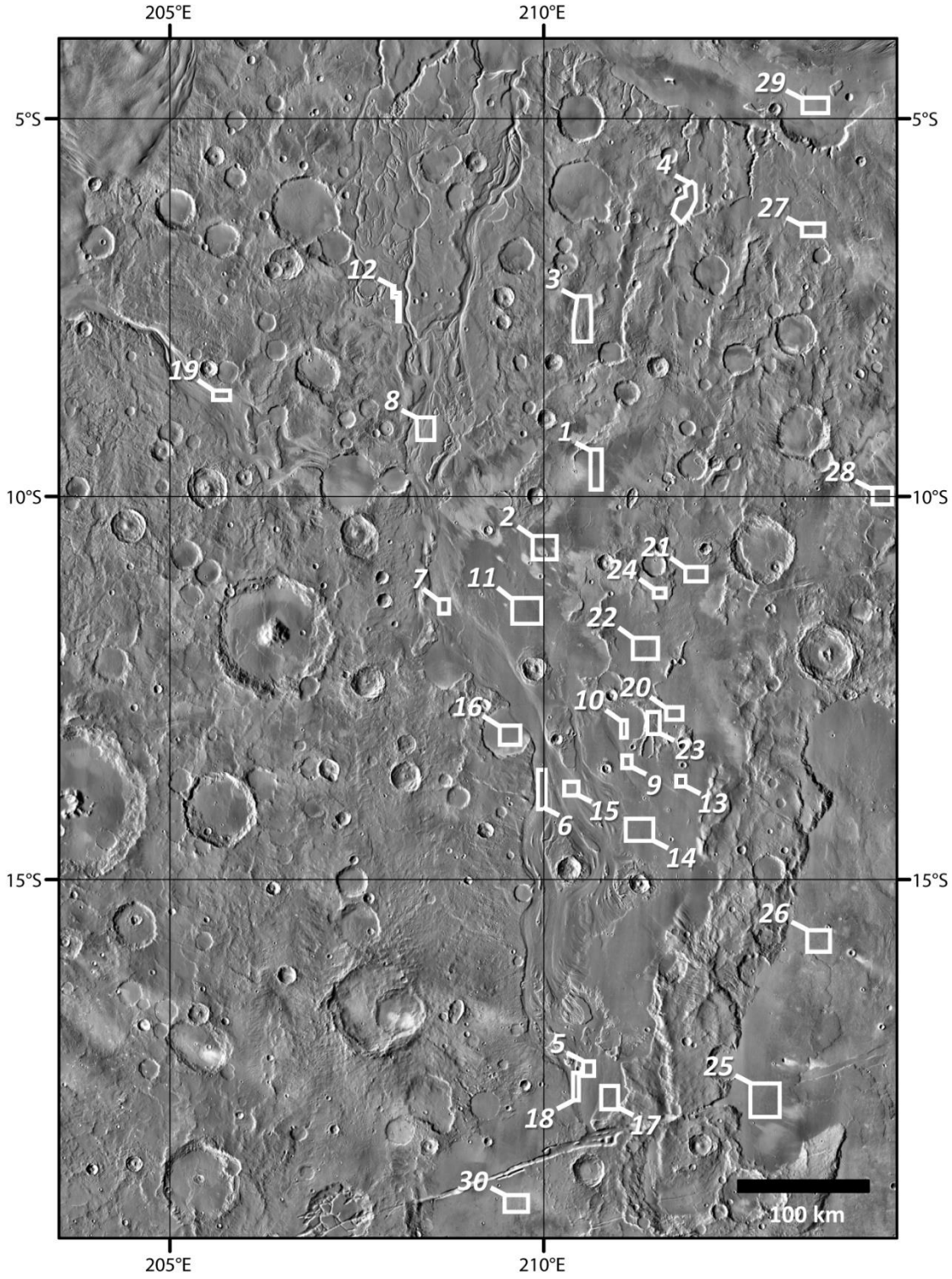

Figure A.1: Areas where crater counting was performed over a THEMIS Day IR v12 mosaic.

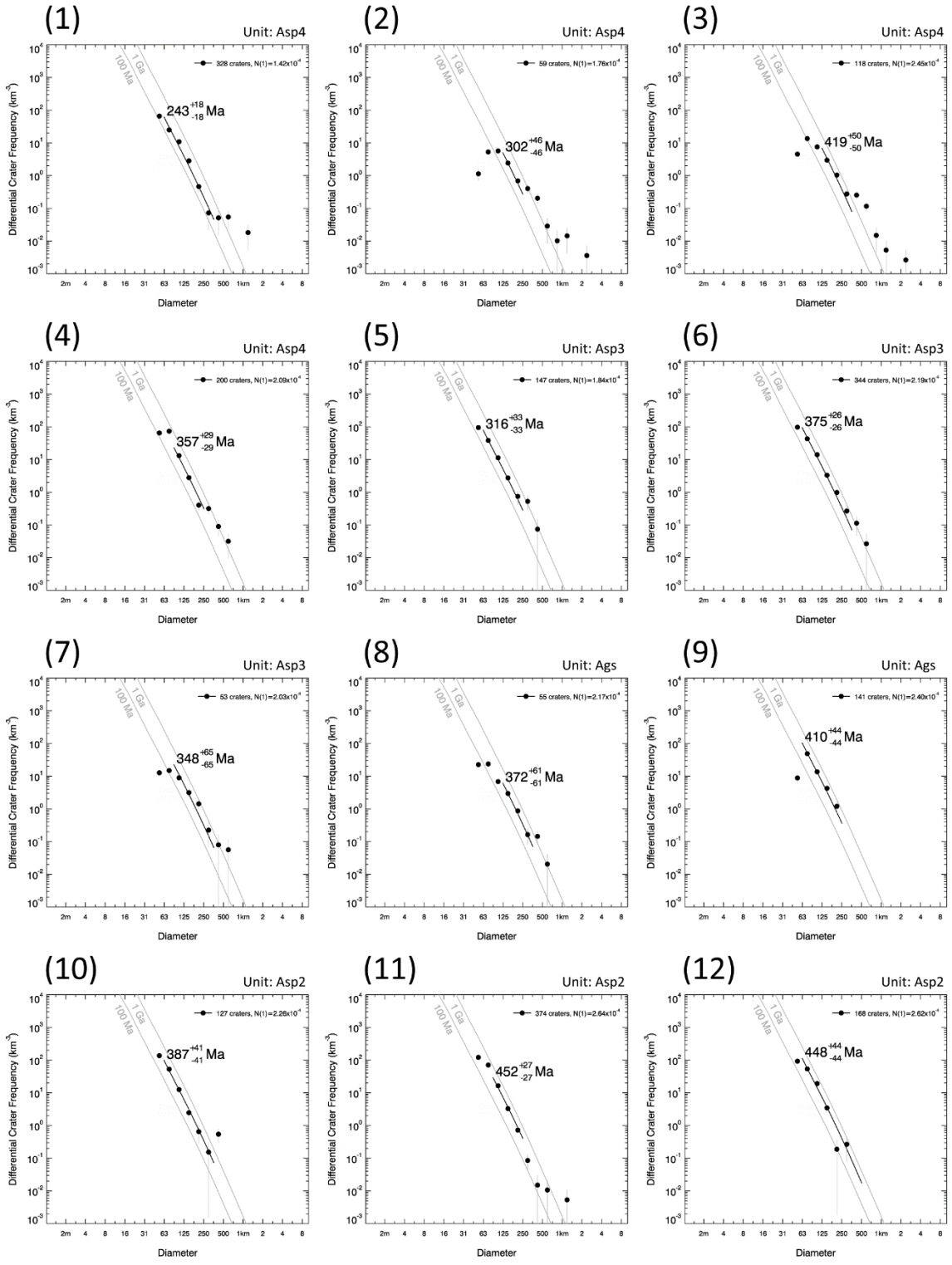
(1)
Unit: Asp4
328 craters, N(1)=1.42x10⁻⁴
243 +18 -18 Ma
(2)
Unit: Asp4
59 craters, N(1)=1.76x10⁻⁴
302 +46 -46 Ma
(3)
Unit: Asp4
118 craters, N(1)=2.45x10⁻⁴
419 +50 -50 Ma
(4)
Unit: Asp4
200 craters, N(1)=2.09x10⁻⁴
357 +29 -29 Ma
(5)
Unit: Asp3
147 craters, N(1)=1.84x10⁻⁴
316 +33 -33 Ma
(6)
Unit: Asp3
344 craters, N(1)=2.19x10⁻⁴
375 +26 -26 Ma
(7)
Unit: Asp3
53 craters, N(1)=2.03x10⁻⁴
348 +65 -65 Ma
(8)
Unit: Ags
55 craters, N(1)=2.17x10⁻⁴
372 +61 -61 Ma
(9)
Unit: Ags
141 craters, N(1)=2.40x10⁻⁴
410 +44 -44 Ma
(10)
Unit: Asp2
127 craters, N(1)=2.26x10⁻⁴
387 +41 -41 Ma
(11)
Unit: Asp2
374 craters, N(1)=2.64x10⁻⁴
452 +27 -27 Ma
(12)
Unit: Asp2
168 craters, N(1)=2.62x10⁻⁴
448 +44 -44 Ma
1 Ga
100 Ma
Differential Crater Frequency (km⁻²)
Diameter
2m 4 8 16 31 63 125 250 500 1km 2 4 8

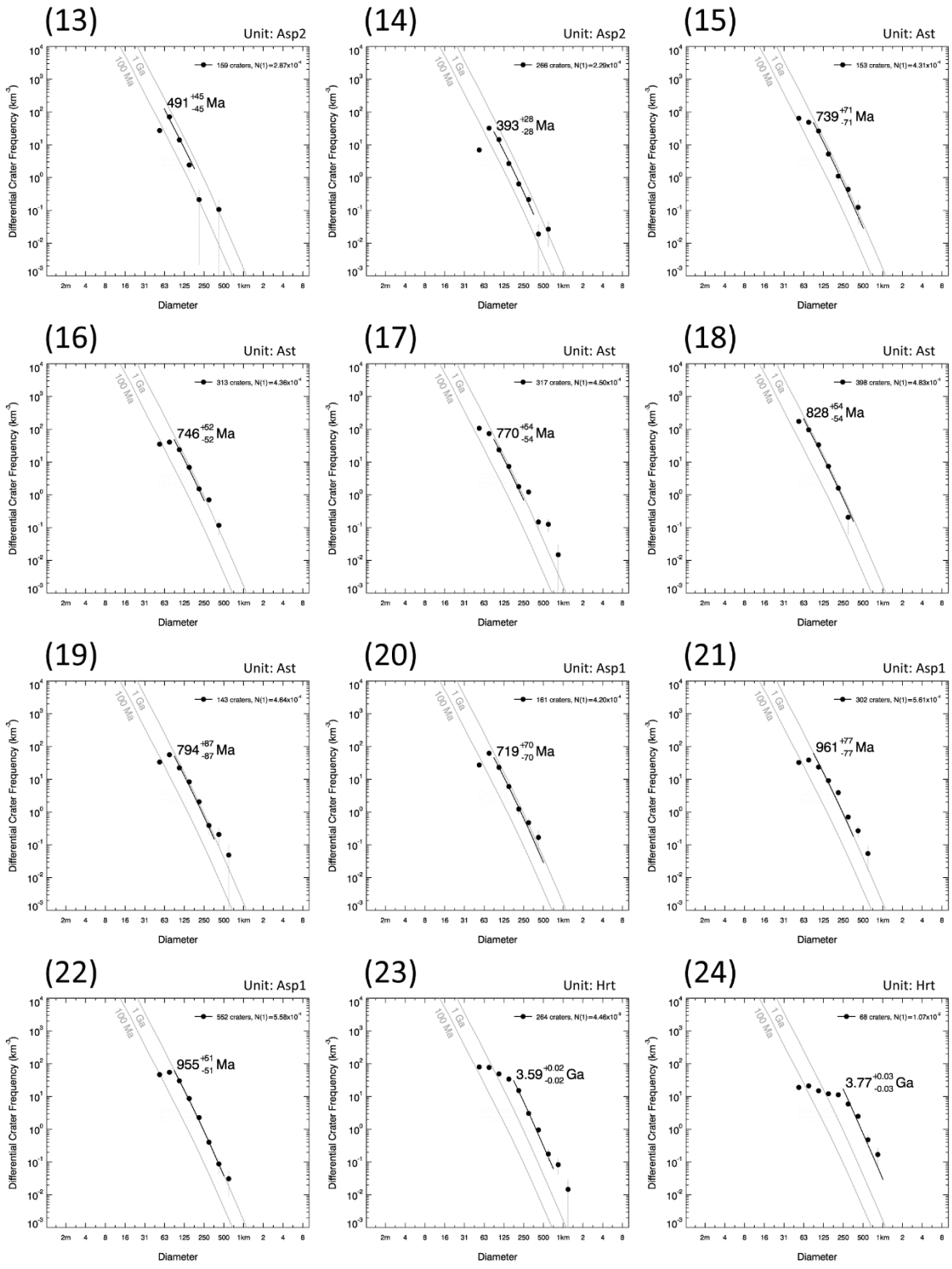
(13)
Unit: Asp2
159 craters, N(1)=2.87x10⁻⁴
491 +45 -45 Ma
(14)
Unit: Asp2
266 craters, N(1)=2.29x10⁻⁴
393 +28 -28 Ma
(15)
Unit: Ast
153 craters, N(1)=4.31x10⁻⁴
739 +71 -71 Ma
(16)
Unit: Ast
313 craters, N(1)=4.36x10⁻⁴
746 +52 -52 Ma
(17)
Unit: Ast
317 craters, N(1)=4.50x10⁻⁴
770 +54 -54 Ma
(18)
Unit: Ast
398 craters, N(1)=4.83x10⁻⁴
828 +54 -54 Ma
(19)
Unit: Ast
143 craters, N(1)=4.64x10⁻⁴
794 +87 -87 Ma
(20)
Unit: Asp1
161 craters, N(1)=4.20x10⁻⁴
719 +70 -70 Ma
(21)
Unit: Asp1
302 craters, N(1)=5.61x10⁻⁴
961 +77 -77 Ma
(22)
Unit: Asp1
552 craters, N(1)=5.58x10⁻⁴
955 +51 -51 Ma
(23)
Unit: Hrt
264 craters, N(1)=4.46x10⁻⁴
3.59 +0.02 -0.02 Ga
(24)
Unit: Hrt
68 craters, N(1)=1.07x10⁻⁴
3.77 +0.03 -0.03 Ga
1 Ga
100 Ma
Differential Crater Frequency (km⁻²)
Diameter
2m 4 8 16 31 63 125 250 500 1km 2 4 8

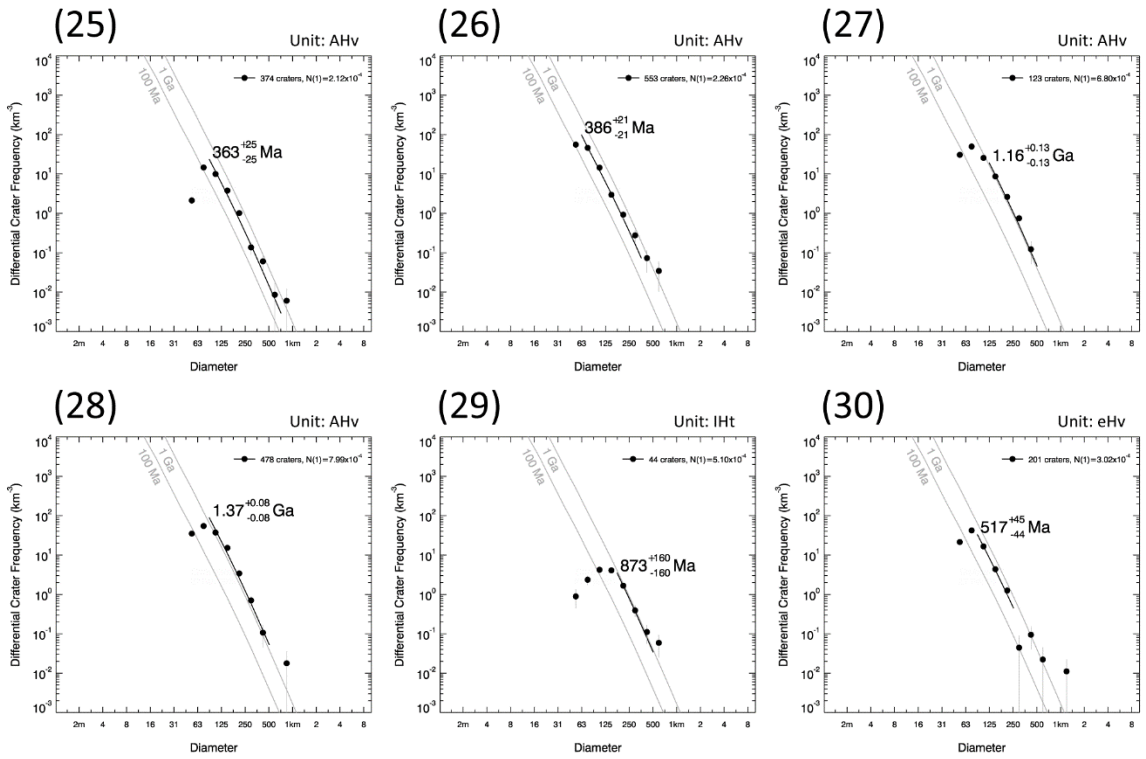

Figure A.2: Crater size-frequency distribution (CSFD) plots for each crater count performed, with boxes marking data points. Light gray lines represent isochrons based on the Hartmann (2005) model, black line represents the model age isochron plotted through the points used to calculate the model age. Age estimate and corresponding standard error is shown to the right of the function.

APPENDIX B

CRATER SIZE FREQUENCY DISTRIBUTIONS FOR MAJA VALLES

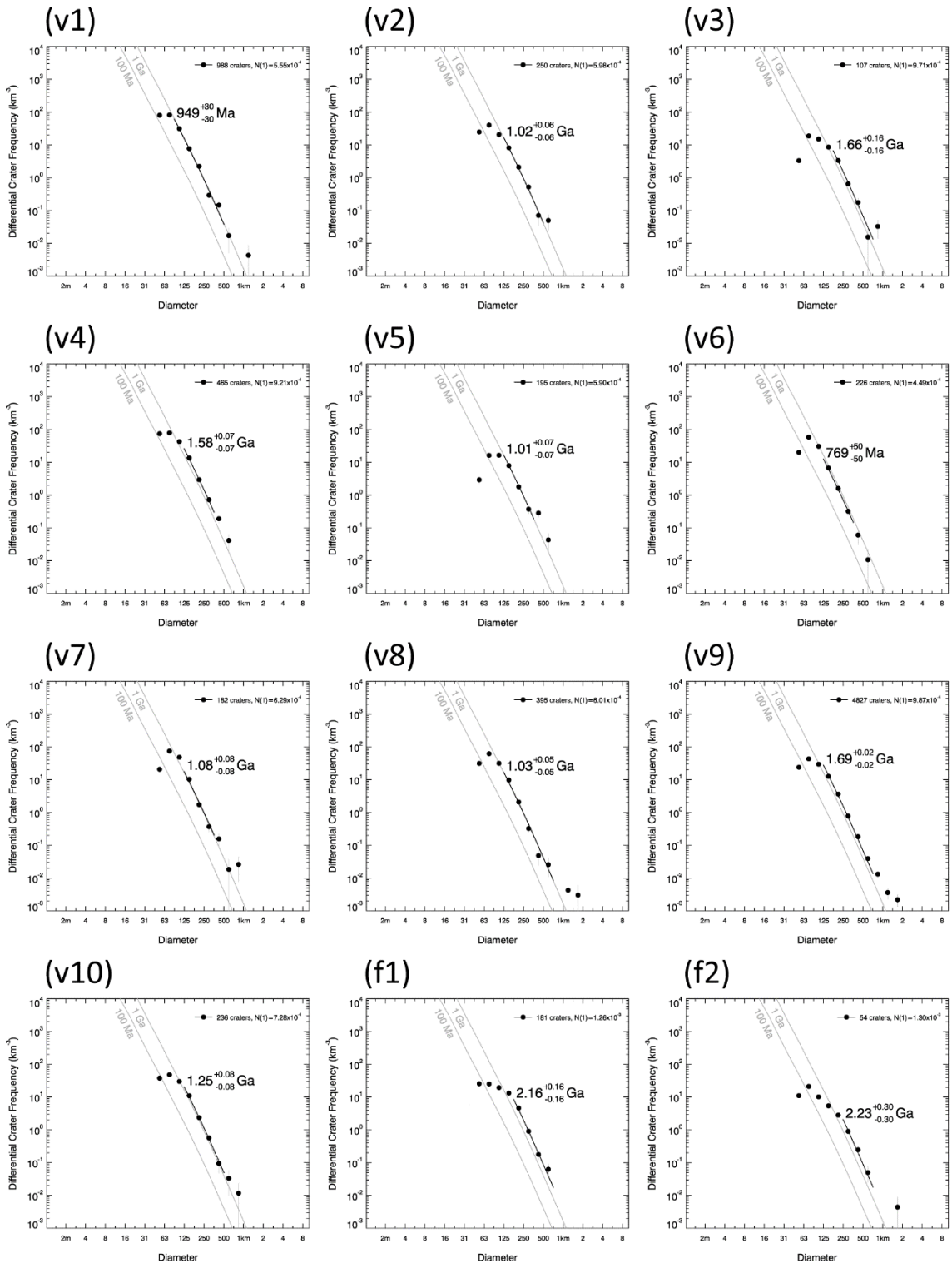
(v1)
988 craters, N(1)=5.55x10⁻⁴
949 +30 -30 Ma
(v2)
250 craters, N(1)=5.98x10⁻⁴
1.02 +0.06 -0.06 Ga
(v3)
107 craters, N(1)=9.71x10⁻⁴
1.66 +0.16 -0.16 Ga
(v4)
465 craters, N(1)=9.21x10⁻⁴
1.58 +0.07 -0.07 Ga
(v5)
195 craters, N(1)=5.90x10⁻⁴
1.01 +0.07 -0.07 Ga
(v6)
226 craters, N(1)=4.49x10⁻⁴
769 +50 -50 Ma
(v7)
182 craters, N(1)=6.29x10⁻⁴
1.08 +0.08 -0.08 Ga
(v8)
395 craters, N(1)=6.01x10⁻⁴
1.03 +0.05 -0.05 Ga
(v9)
4827 craters, N(1)=9.87x10⁻⁴
1.69 +0.02 -0.02 Ga
(v10)
236 craters, N(1)=7.28x10⁻⁴
1.25 +0.08 -0.08 Ga
(f1)
181 craters, N(1)=1.26x10⁻³
2.16 +0.16 -0.16 Ga
(f2)
54 craters, N(1)=1.30x10⁻³
2.23 +0.30 -0.30 Ga
1 Ga
100 Ma
Differential Crater Frequency (km⁻²)
Diameter
2m 4 8 16 31 63 125 250 500 1km 2 4 8

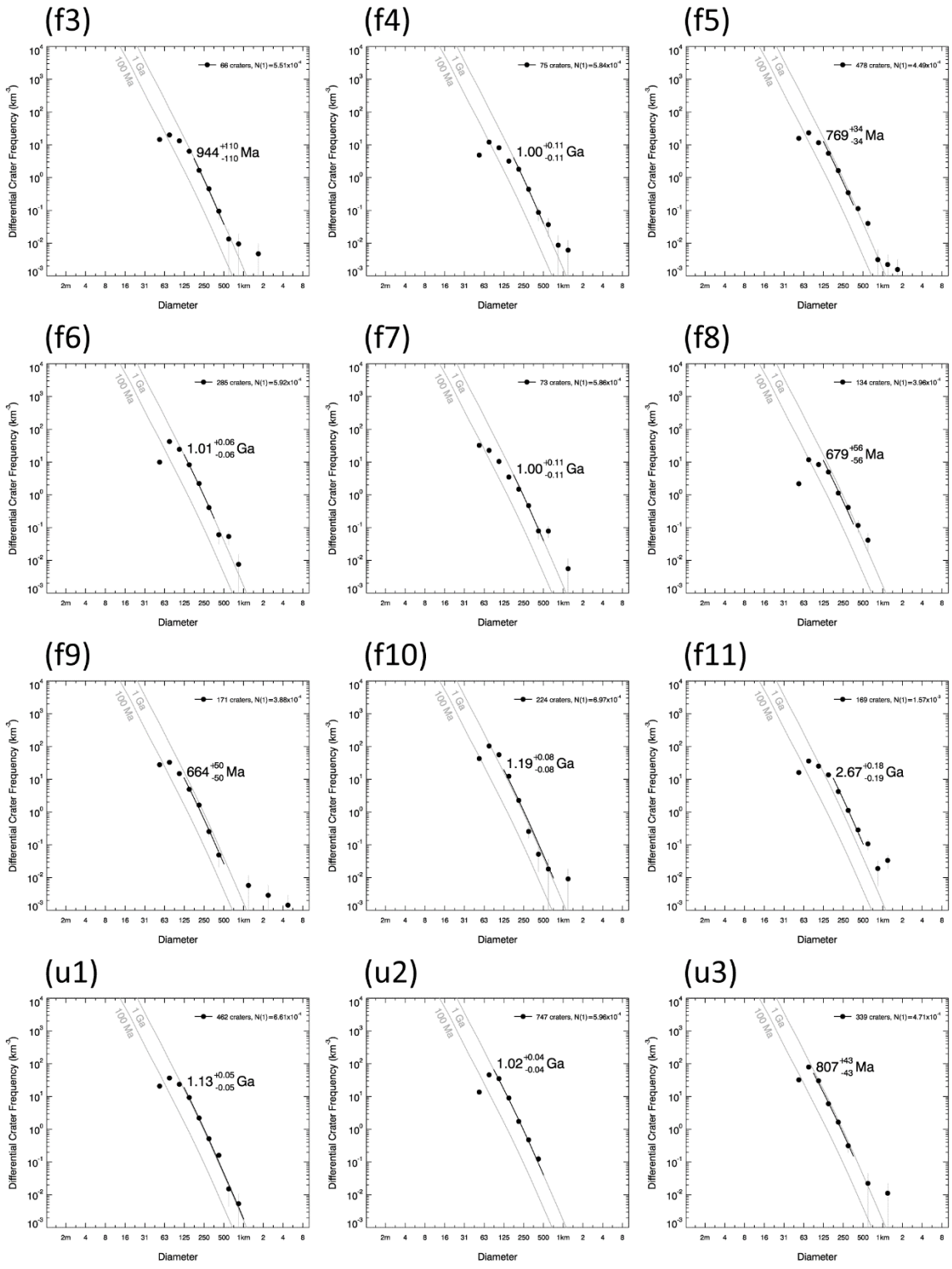
(f3)
66 craters, N(1)=5.51x10⁻⁴
944 +110 -110 Ma
(f4)
75 craters, N(1)=5.84x10⁻⁴
1.00 +0.11 -0.11 Ga
(f5)
478 craters, N(1)=4.49x10⁻⁴
769 +34 -34 Ma
(f6)
285 craters, N(1)=5.92x10⁻⁴
1.01 +0.06 -0.06 Ga
(f7)
73 craters, N(1)=5.86x10⁻⁴
1.00 +0.11 -0.11 Ga
(f8)
134 craters, N(1)=3.96x10⁻⁴
679 +56 -56 Ma
(f9)
171 craters, N(1)=3.88x10⁻⁴
664 +50 -50 Ma
(f10)
224 craters, N(1)=6.97x10⁻⁴
1.19 +0.08 -0.08 Ga
(f11)
169 craters, N(1)=1.57x10⁻⁴
2.67 +0.18 -0.19 Ga
(u1)
462 craters, N(1)=6.61x10⁻⁴
1.13 +0.05 -0.05 Ga
(u2)
747 craters, N(1)=5.96x10⁻⁴
1.02 +0.04 -0.04 Ga
(u3)
339 craters, N(1)=4.71x10⁻⁴
807 +43 -43 Ma
1 Ga
100 Ma
Differential Crater Frequency (km⁻²)
Diameter
2m 4 8 16 31 63 125 250 500 1km 2 4 8

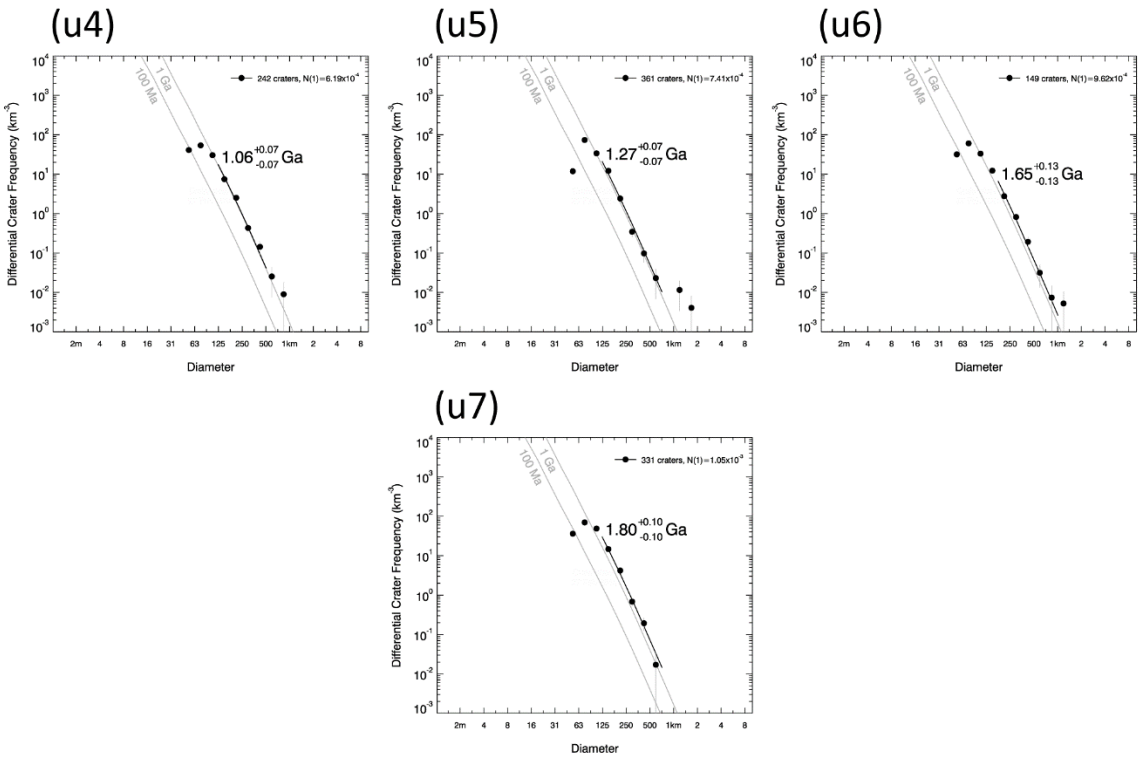

Figure B.1: Crater size-frequency distribution (CSFD) plots for each crater count performed, with boxes marking data points. Light gray lines represent isochrons based on the Hartmann (2005) model, black line represents the model age isochron plotted through the points used to calculate the model age. Age estimate and corresponding standard error is shown to the right of the function.